Fundamental understanding of re-dispersion of cobalt on supported model Fischer-Tropsch catalysts

By
Magdalena Maria Hauman
B.Pharm
University of Potchefstroom

Thesis submitted for the degree of
Masters in Chemical Engineering
at the University of Cape Town

Supervisor: Prof. Eric van Steen, UCT
Co-supervisors: Dr. Abdool Saib, Sasol Limited
and Dr. Denzil Moodley, Sasol Limited

January 2011

DECLARATION

I know the meaning of plagiarism and declare that all the work in the document, save for that which properly acknowledge, is my own.

Magdalena Maria Hauman
February 2011

ACKNOWLEDGEMENTS

I would like to thank everyone contributing to this thesis and to help me to grow and learn.

I would like to thank Sasol Technology, Research and Development for funding this project. I would like to thank Philip Gibson for allowing me and giving me the opportunity at a different age that most people will complete an M.Sc.

I would like to thank Prof. Eric van Steen, my supervisor, for the privilege to do a M.Sc. study under his guidance. I would like to thank Eric for his patience, time, teaching and his kindness.

I would like to thank Dr. Abdool Saib, my co-supervisor, for giving me the opportunity to grow. I would like to thank Abdool for the time made available to complete my thesis, for his support and his guidance.

I would like to thank Dr. Denzil Moodley for all his time, willingness to help, guidance and sharing his knowledge.

I would like to thank the following Sasol colleagues for their contributions:

- Jolandie Davel for helping me with catalyst preparation and for her friendship.
- Dr. Esna du Plessis for helping me with XRD characterization. Her time and patience to teach me and to help me by delivering data that contributes significantly to this thesis.
- Beatrice Breedt for doing the XRD experimental work and to teach me how to use the software.
- Ghislaine ter Stege for all her effort with the TEM images. I would like to thank Ghislaine for her time and willingness and for taking the amazing images.
- Willem Erasmus for TEM images. I would like to thank Willem for his time, willingness to help and taking me with him to the University of the Witwatersrand where the electron microscope is situated.
- Henno Gericke for being always so friendly and for doing the XPS analyses in Eindhoven.

- Dr. Hardi Koortzen for helping me and teaching me how to use the TPR. I would like to thank Hardi for his friendship, helping me with anything I asked and all the enjoyable teatimes.
- Dr. Michael Datt for sending on relevant articles and for his friendship.
- Dr. Frans Prinsloo for always being willing to help and to answer my questions.
- Susan Lethale (SCI) for doing the ICP analyses.
- Pheladi Mohlala for doing the H_2 chemisorption analyses.
- Deshen Kistamurthy for running the fixed bed reactors, his perseverance, his friendly smile and willingness to help.
- Ludwig Wedemeyer for helping with the running of the fixed bed reactors, the creative naming of the runs and his willingness to help.

I would like to thank my children, Martin, Rikus en Neil, for giving me the time to do this. I would like to thank them for their love.

I would like to thank my husband, Don, who believes in me, who encourages me and who loves me.

I would like to thank God.

SYNOPSIS

Supported-cobalt catalysts are usually preferred for Fischer-Tropsch synthesis (FTS) in the gas-to-liquid (GTL) process for reasons of stability, higher per pass conversion, high selectivity towards linear paraffins and low CO_2 selectivity. However, supported-cobalt FTS catalysts, as with many other catalyst systems lose their activity with time on stream. Cobalt is an expensive metal and it is therefore it is important to maximize the cobalt catalyst lifetime. One option is to regenerate the catalyst after time on stream to reverse the deactivation mechanisms at play thereby increasing the activity of the spent catalyst similar to that of a fresh catalyst. A typical regeneration procedure consists of a de-waxing step followed by an oxidation step to remove the carbon. This is followed by a reduction step to re-activate the catalyst.

A number of different mechanisms are postulated for the deactivation of a supported-cobalt catalyst. Literature showed that the main deactivations mechanisms for a typical FTS supported-cobalt catalyst are carbon formation and sintering if the Fischer-Tropsch synthesis is conducted in a poison free environment. Catalyst deactivation can then result due to a decrease of the number of active sites if sintering is the deactivation mechanism at play. It is then of importance to improve re-dispersion of a sintered deactivated supported cobalt catalyst.

The aim of this study was to investigate how the catalytically active material may re-disperse during consecutive oxidation-reduction steps (OROR) for a model supported-cobalt catalyst to give insight into the regeneration process of a spent supported-cobalt FTS catalyst. For this study, a simplified supported-cobalt catalyst was prepared on a $\alpha\text{-}Al_2O_3$ model support. A simplified system was chosen due to the complexity of commercial supported catalysts that makes it difficult to gain information with certain characterization methods. The influences of other parameters (e.g. promoters) are therefore also limited.

An aluminium oxide (Ceralox APA-0.5) with a surface area of 8.1 m^2/g was used as a support to prepare a catalyst with a cobalt loading of 8 mass %. A main catalyst batch (Experiment 1) was prepared by impregnation of the support with a cobalt nitrate solution. This batch was used to produce other catalysts in either a reduced or oxidised state, viz. the reduced catalyst (Experiment 2), the re-oxidised, reduced catalyst (Experiment 3), the reduced, re-oxidised, reduced catalyst (Experiment 4),

and the re-oxidised reduced catalyst, which was re-oxidised at elevated pressure (10 bar) (Experiment 5).

TEM images showed discreet crystallites on the surface of the support after preparation of the main batch of the supported-cobalt catalyst. Hollow sphere crystallites were observed when studied using TEM after the oxidation (ORO cycle with O = oxidation and R = reduction) of the reduced calcined sample. A decrease in average Co_3O_4 crystallite size was observed with XRD from 33 nm to 9 nm. The decrease can be ascribed to the measurement of the diameter of a solid crystallite compared to the measurements of only crystalline domains in the shell of the hollow sphere. A shell width of 9 nm (± 2.8 nm) was measured after the ORO cycle. Hollow spheres were also formed during the high-pressure oxidation of the reduced calcined sample. Smaller crystalline domains of 6.4 nm (± 1.5 nm) were formed in the outer shell. However, a third oxidation step (ORORO catalyst) did not result in a smaller average Co_3O_4 crystallite size. The smallest average Co_3O_4 crystallite size was obtained during high-pressure oxidation.

Smaller metallic cobalt crystallites were observed with TEM after the reduction of a hollow sphere as apposed to that of a solid oxide particle. This indicated that after hollow sphere formation, a well-dispersed cobalt metal was obtained on a model supported-cobalt catalyst. The reduction in the average crystallite size of metallic cobalt was also confirmed by an increase in the metal surface area.

In-situ XRD was used to study phase changes of the cobalt crystallites during consecutive oxidation and reduction steps. Both hexagonal closed packed (hcp) cobalt and face centred cubic (fcc) cobalt were detected by *in-situ* XRD in the reduced catalyst samples. The amount of hcp-Co relative to the amount of fcc-Co was higher after the second reduction step of the in-situ XRD experiment. This unexpected result can be explained, as been postulated in literature, that hcp-Co could form during heating up to the transition temperature during reduction and then remain as hcp-Co because it is stabilised by its environment.

The oxidation of a previously reduced catalyst sample (ORO catalyst) resulted in a lower amount of hydrogen consumed upon reducing during the TPR-analysis. A shift in the temperature of reduction (TPR analysis) for the cobalt species of Experiment 5 (re-oxidised reduced catalyst, which was re-oxidised at elevated pressure) in the 400-500°C range was towards higher temperatures due to small crystallites. The temperature of reduction during TPR analysis was lower after hollow sphere formation (as observed with TEM) for the supported-cobalt catalyst. *In-situ* XRD showed that not only did the on-set of reduction for the re-oxidised sample start at a lower temperature, but also that the whole reduction process occurred at a lower temperature. This is probably due to the larger surface available in the case of a hollow sphere where more Co_3O_4 sites are accessible to the hydrogen. The upper part of the hollow sphere also experiences less metal support interaction which makes reduction more facile.

The rate of CO consumption during FTS, normalized per unit surface area showed that the catalysts were less active after the formation of hollow spheres. If the metal surface area is an indication of the number of active sites available in the catalyst, it would be expected that the catalyst, which was re-oxidised under high-pressure would be the most active catalyst. The presence of small cobalt crystallites (< 6 nm) may have resulted in the reduction / lowering of the averaged turn-over-frequencies as has also been reported in literature. These small crystallites were observed with TEM after the reduction of the re-oxidized samples, which contain hollow spheres.

In conclusion, hollow sphere formation leads to a well-dispersed catalyst with a high available surface area. This phenomenon makes an oxidative regeneration process attractive to improve the dispersion of cobalt metal on a deactivated catalyst. However, a highly dispersed cobalt-based catalyst is not necessarily the most active.

TABLE OF CONTENTS

CHAPTER 3

CHAPTER 4

CHAPTER 5

CHAPTER 6

CHAPTER 7

APPENDIX A

APPENDIX B

LIST OF TABLES

LIST OF FIGURES

NOMENCLATURE

ABBREVIATIONS

CNF	Carbon nanofiber
EELS	Electron energy loss spectroscopy
EFTEM	Energy filtered transmission electron microscopy
EXAFS	Extended X-ray absorption fine structure
fcc	Face centred cubic
FG	Feed gas
FT	Fischer-Tropsch
FTS	Fischer-Tropsch synthesis
GC	Gas chromatograph
GTL	Gas-to-liquid
hcp	Hexagonal closed packed
HDP	Homogeneous deposition-precipitation
HP	High pressure
HRTEM	High resolution transmission electron microscopy
HSLEIS	High sensitive low energy ion scattering
ICP-OES	Inductively coupled plasma optical emission spectroscopy
LEIS	Low energy ion scattering
MFC	Mass flow controllers
OROR	Oxidation-reduction- oxidation-reduction
PZC	Point of zero charge
RF	Radio frequency
Riaf	Relative intrinsic activity factor
ROR	Reduction-oxidation-reduction
SIMS	Secondary ion mass spectrometry
SSITKA	Steady-State Isotopic Transient Kinetic Analysis
SSMI	Strong metal-support interaction
STM	Scanning tunnelling microscopy
STP	Standard temperature pressure
TCD	Thermal conductivity detector
TEM	Transmission electron microscopy
TG	Tail gas
TOF	Turn-Over-Frequency
TP	Temperature programmed

TPD	Temperature programmed desorption
TPH	Temperature programmed hydrogenation
TPR	Temperature programmed reduction
WGS	Water gas shift
XANES	X-ray absorption near edge spectroscopy
XPS	X-ray photoelectron spectroscopy
XRD	X-ray diffraction

CHAPTER 1

INTRODUCTION

Supported-cobalt catalysts are usually preferred for Fischer-Tropsch synthesis (FTS) in the gas-to-liquid (GTL) process for reasons of stability, higher per pass conversion, high selectivity to linear paraffins and low CO_2 selectivity [1,2,6]. However, supported-cobalt Fischer-Tropsch catalysts, as many other catalyst systems, loose their activity with time on stream [3]. A number of different mechanisms are postulated for the deactivation of supported-cobalt catalysts. Literature showed that the main deactivation mechanisms for a commercial FTS supported-cobalt catalyst are carbon formation and sintering if the FTS is conducted in a poison free environment [4,5]. Poisons in the synthesis gas such as sulphur and nitrogen compounds can also lead to catalyst deactivation. [7,52]. Cobalt is an expensive metal and it is therefore important to maximize the cobalt catalyst lifetime [6]. One option is to regenerate the catalyst after time on stream to reverse the deactivation mechanisms at play thereby increasing the activity of the spent catalyst to that of a fresh catalyst.

A typical regeneration procedure consists of a de-waxing step followed by an oxidation step to remove the formed carbon. The oxidation step is followed by a reduction step to activate the catalyst. During this regeneration procedure, the deactivated catalyst will experience an additional oxidation and reductions step since the initial catalyst preparation because the freshly prepared catalyst is calcined to remove residual nitrate and then reduced during catalyst preparation [7-9].

Sintering plays an important role as a deactivation mechanism in cobalt-based Fischer-Tropsch catalysts [6,10-12]. In a simplified case, it can be postulated that the catalytic activity is proportional to the number of active sites [49]. Catalyst deactivation can then result due to a decrease of the number of active sites if sintering is the deactivation mechanism at play. It is then of importance to improve re-dispersion of a sintered deactivated supported cobalt catalyst. An oxidative treatment of a reduced catalyst may result in re-dispersion of the catalytically active material, as observed for platinum [13], rhenium [14] and cobalt [7].

In this study, re-dispersion of cobalt crystallites in a supported cobalt FTS catalyst will be investigated. In particular, re-dispersion of cobalt crystallites occurring during consecutive oxidation and reduction steps, will be studied, since these conditions will be experienced by the deactivated catalyst during a regeneration process. The study will focus on the morphology changes of the cobalt metal during a second oxidation and reduction step. A simplified supported-cobalt catalyst was prepared on a α-Al_2O_3 model support because the complexity of commercial supported catalysts makes it difficult to gain information with certain characterization methods. The influences of other parameters (e.g. promoters) are limited in this way [48].

CHAPTER 2

LITERATURE REVIEW

Supported-cobalt catalysts are the preferred catalyst for the Fischer-Tropsch synthesis (FTS) in a gas-to-to liquid (GTL) process [1,2]. Supported-cobalt Fischer-Tropsch catalysts as many other systems lose some of their activity with time on stream [3-5,7]. It is shown in literature that it is possible to regenerate a spent supported-cobalt Fischer-Tropsch catalyst and to regain the activity of a fresh catalyst [7].

The literature study will give a brief introduction to the FTS and the gas-to-liquid process and outline why supported-cobalt catalyst is the catalyst of choice is for Fischer-Tropsch synthesis (FTS).

The synthesis of a supported-cobalt catalyst is also very important to obtain a highly active catalyst. The most frequent used preparation methods to obtain an active FTS catalyst will be discussed. A model catalyst was used for this study and the importance of model catalysts for research will be highlighted.

Deactivation of a FTS supported-cobalt catalyst will be discussed and also the deactivation mechanisms at play. Regeneration procedures that are applied to regain the activity of a deactivated catalyst will be discussed.

2.1 Fischer-Tropsch synthesis and the gas-to-liquid process

Natural gas is a “clean” building block for Fischer-Tropsch synthesis (FTS). The conversion of natural gas to hydrocarbons is typically carried out in two steps. In the first step methane is reformed with water or partially oxidised with oxygen to produce carbon monoxide and hydrogen that is known as synthesis gas. In the second step, the synthesis gas is converted to hydrocarbons [15].

The second step is known as the Fischer-Tropsch process, which is the catalytic conversion of synthesis gas, carbon monoxide and hydrogen, yielding hydrocarbon products. The reaction taking place during Fischer-Tropsch synthesis can be stoichiometrically described as follows when only methane is produced [16]:

$$CO + 3H_2 \rightarrow CH_4 + H_2O$$

Heavier hydrocarbons are also formed during Fischer-Tropsch synthesis (FTS) and the simplified, stoichiometric equation can be expressed as [17]:

$$n\,CO + 2n\,H_2 \rightarrow (-CH_2-)_n + n\,H_2O$$

The gas-to-liquid process (GTL) process has in addition to the Fischer-Tropsch process, a hydro-cracking step for the production of liquid fuel. Hence, the gas-to-liquid process can be divided into three steps, i.e. synthesis gas generation (methane reforming), synthesis gas conversion (FTS) and hydro-processing. In the third step of the gas-to-liquid process (GTL) process wax produced in the Fischer-Tropsch synthesis is hydro-isomerised/hydro-cracked to produce high quality diesel (C_{11}-C_{18}) and naphta (C_5-C_{10}) [17].

2.2 Supported cobalt catalyst versus iron-based catalyst

Ruthenium followed by iron, nickel and cobalt are the most active metals for the hydrogenation of carbon monoxide (CO). Nickel catalysts under practical conditions produce too much methane and ruthenium is too expensive. Hence, only cobalt-based (Co) and iron-based (Fe) catalysts are used commercially for the Fischer-Tropsch synthesis [18]. Cobalt-based catalysts are more expensive than iron-based catalysts [6,18], and the preference of one type of catalyst above the other catalyst needs to be evaluated carefully.

The activity of iron-based catalysts and the activity of cobalt-based catalysts for the Fischer-Tropsch synthesis are comparable at low conversions [2]. However, cobalt catalysts have a higher productivity at higher conversion, since water generated during the Fischer-Tropsch synthesis (FTS) slows down the reaction over iron-based catalysts more than over cobalt-based catalysts [2,19-21], despite the mitigating extent of the water gas shift (WGS) reaction, which is more significant over iron-based catalysts than over cobalt-based catalysts [16].

The water gas shift (WGS) reaction is given by the following stoichiometric equation [16]:

$$CO + H_2O \rightarrow CO_2 + H_2$$

The high activity of iron-based catalysts for the water gas shift (WGS) reaction results in a much higher CO_2 formation with these catalysts. This is a major concern for Gas-to-Liquid (GTL) processes, since this will lower the carbon efficiency of the process (less carbon in the feed is converted into the desired product) and a higher emission of the greenhouse gas, CO_2. However, the higher water-gas shift (WGS) activity of iron-based catalysts allows the use of synthesis gas with a sub-stoichiometric H_2/CO ratio as present in coal and biomass derived synthesis gas [6].

The Fischer-Tropsch synthesis over iron-based catalysts yields predominantly linear alpha olefins and a mixture of oxygenates such as alcohols, aldehydes and ketones [1], whereas the product of the Fischer-Tropsch synthesis over cobalt-based catalysts contains relatively more paraffins. The latter is more desired if diesel-type of fuel is the product of choice.

The operating window of cobalt-based Fischer-Tropsch catalysts and iron-based Fischer-Tropsch catalysts differ. Cobalt-based catalysts operate at a very narrow temperature range and an increase in temperature leads to a strong increase in methane selectivity [18]. The minimum operating temperature of Iron-based catalysts is typically slightly higher (15-30^{o}C) than the typical operating temperature of cobalt-based temperature. A temperature increase in iron-based Fischer-Tropsch synthesis leads to a modest increase in the methane selectivity. This allows iron-based catalysts to be operated in two different modes [16], i.e. low temperature mode (245-270^{o}C) with as the main product long chain hydrocarbons (wax) and high temperature mode (300-350^{o}C) yielding short chain olefins and gasoline range hydrocarbons.

Catalyst stability is of utmost importance [6]. The use of a catalyst, which is per unit mass more expensive, can be justified if its life time mitigates the cost difference. Both cobalt-based and iron-based catalysts are sensitive to sulphur poisoning. For iron-based catalysts the sulphur content in the synthesis gas should be less than 2 ppm and for cobalt less than 0.1 ppm [18]. Cobalt catalysts supported on oxide supports are more resistant to attrition and are therefore more suitable for slurry-type reactors [22].

Cobalt seems to be the catalyst of choice for Fischer-Tropsch synthesis (FTS) in the gas-to-liquid (GTL) process due to its stability, higher per pass conversion, high selectivity to linear paraffins and low CO_2 production.

2.3 Synthesis of a supported cobalt catalyst

The performance of Fischer-Tropsch (FT) catalysts is influenced by the methods of catalyst preparation [23]. The preparation of cobalt supported catalyst consists of several steps, i.e. the choice of support, method of deposition of the cobalt, catalyst promotion and oxidative and reductive treatments. The ultimate goal of the deposition of the catalytically active phase on a support is to obtain catalysts with a high surface area of the catalytically active material. The properties of the catalyst, number of cobalt active sites and localization on the support can be controlled by promotion with noble metals and oxides. The performance of the FT catalysts is also strongly influenced by the different oxidising and reducing pre-treatments [23].

Highly active catalysts for the Fischer-Tropsch synthesis are required, since Fischer-Tropsch synthesis catalysts with high volumetric productivity result in smaller reactor volume requirements and improve significantly process economics. The preparation method of a supported cobalt catalyst plays an important role to control the volumetric productivity of a cobalt catalyst. Supported cobalt (Co) catalysts with a high intrinsic activity require supported catalysts with small metal crystallites and a high surface density on the support surface [23]. With particles larger than 10 nm, the turnover rates are not influenced by dispersion or support effects at conditions favouring chain growth (C_{5+} selectivity > 80%) [24]. It was however determined that the turn-over frequency for CO over cobalt crystallites supported on carbon nanofibers with a diameter less than 6 nm is significantly lowered [25]. The effect of cobalt crystallite size in Fischer-Tropsch catalysis was studied with Steady-State Isotopic Transient Kinetic Analysis (SSITKA) [26]. It was found at a pressure of 1.85 bar and $H_2/CO = 10$ that the residence time of CH_x and OH_x intermediates was higher with cobalt particles smaller than 6 nm, but it was lower for adsorbed CO. The residence time of CH_x, OH_x and CO appeared independent when catalysts with larger crystallites (> 6 nm) were studied. The surface coverage of CH_x, OH_x and CO intermediates decreased for small particles and is constant for larger crystallites (> 6 nm). It was concluded from CO introduction experiments that a significant amount of irreversible bonded CO molecules is present on the small particles. This causes blocking of the cobalt surface resulting in a lower TOF for CO hydrogenation over Co particles smaller than 6 nm. The increase in methane selectivity with smaller cobalt crystallite sizes was ascribed to a higher coverage of the surface with hydrogen. Hence, the catalytic performance of cobalt catalysts in the Fischer-Tropsch synthesis is independent of cobalt particle sizes, if the crystallite size is larger than 6 nm. The catalyst productivity under typical FTS conditions can then be predicted directly from Co dispersion values as measured by e.g. hydrogen chemisorption [23,24].

The synthesis of highly dispersed cobalt catalysts requires the initial formation of small cobalt oxide (CoO and Co_3O_4) crystallites. Cobalt dispersions above 0.15 to 0.2 from hydrogen (H_2) chemisorption (5-6 nm crystallite diameters) are difficult to achieve during synthesis [23]. Small crystallites (< 4 nm) appear to oxidise and deactivate rapidly in the presence of water reaction products at typical FTS conditions [7].

2.3.1 Role of support in catalyst preparation

The support plays an important role in the structure and performance of cobalt supported catalysts. The support is important for dispersion of the cobalt and to produce stable cobalt metal particles after reduction. The cobalt particle size is controlled by the porous structure of the support [27,28]. A series of cobalt supported catalyst were prepared with different pore size γ-Al_2O_3 supports [28]. It was found that the average Co_3O_4 crystallite size was dependent on the type of γ-Al_2O_3 support. The average crystallite size of Co_3O_4 increased with increasing pore size. Furthermore, it was observed that the C_{5+}-selectivity increased by choosing a support that contained wide pores.

Aluminium oxide (Al_2O_3) is one of the most used supports for cobalt FTS catalysts, due to its high attrition resistance [22]. Cobalt oxide strongly interacts with Al_2O_3 support, forming relative small cobalt crystallites [23]. Reducibility is higher in silica supported cobalt Fischer-Tropsch catalysts because the interaction between the support and cobalt is not very strong [29,30]. However, cobalt dispersion is much lower on silica supported catalysts than on alumina supported catalysts. In order to mitigate the low reducibility of cobalt on alumina, noble metals are added to improve reducibility [29,31,32].

2.3.2 Methods of deposition of the cobalt on the support

Supported-cobalt Fischer-Tropsch catalysts are often prepared by impregnation. Other preparation techniques include co-precipitation, deposition-precipitation, sol-gel methods have been used as well [23] to achieve a homogeneous distribution of cobalt throughout the catalyst particle.

Incipient wetness impregnation is the most common method to prepare cobalt supported catalysts [23]. In this method a solution of cobalt salt (e.g. cobalt nitrate) is contacted with a dry porous support. The solution fills the pores due to capillary forces inside the pores of the support. This process is complete when all the pores are filled and there is no excess moisture available. Reproducibility is controlled by impregnation parameters, i.e. temperature and time of drying and rate of addition of impregnation solution. The distribution Co^{2+} ions on the support after impregnation are affected by electrostatic interactions. At a pH higher than the point of zero charge (PZC), Co^{2+} ions are distributed more homogeneously.

Cobalt repartition in silica supported catalyst during impregnation at different pH was characterized with X-ray photoelectron spectroscopy (XPS) [34]. The XPS spectra revealed the presence of Co^{2+} ions on the surface of the impregnated dried catalyst. The I_{Co}/I_{Si} ratios of the XPS intensities were used to provide information about repartition of cobalt ions on silica surface after calcination. Higher I_{Co}/I_{Si} ratios are characteristic of higher cobalt dispersion in dried cobalt catalyst. An increase in cobalt dispersion (higher I_{Co}/I_{Si} ratio) was observed with an increase in pH. XPS results showed that repartition of Co ions on the surface are getting more uniform with increase in pH value.

Slurry impregnation studies [34] showed that it is important to ensure proper anchoring of cobalt on to the support during the impregnation step of the pre-shaped support material. Insufficient anchoring could result in the washing out of cobalt-rich ultra-fine particles from the porous support material during commercial slurry phase FTS. During catalyst preparation, the dissolved aluminium ions can precipitate either as boehmite or in combination of cobalt ions as a cobalt aluminium hydrotalcite, producing a physically amorphous layer uniformly covering the surface of the bulk support material. The presence of this amorphous layer, prior the actual impregnation, weakens the anchoring of the active cobalt metal. To prevent the dissolution of the alumina during the slurry phase impregnation step of the catalyst preparation step, alumina can be modified with silicon.

The co-precipitation method is mostly used to prepare iron-based Fischer-Tropsch catalysts [18,23].

Deposition-precipitation is precipitation combined with deposition from a liquid medium [23,35]. In this method a metal precursor in solution is deposited onto the surface of a suspended support by slow introduction of a precipitating agent (usually hydroxyl ions). This process consists out of two steps. In the first step precipitation occurs from the bulk solution on the support and in the second step interaction occurs between the precipitate and the support surface. The deposition-precipitation method combines all the advantages of the precipitation method related to control of size and size distribution of precipitated particles, but diminishes the risk of formation of bulk mixed compounds of support and active phase. It is possible to obtain uniform distributed small cobalt particles (3-5 nm). High activity in the FTS over this type of catalyst has been reported with high dispersion and Co loadings.

Homogeneous deposition-precipitation (HDP) of cobalt on either silica or carbon nanofiber (CNF) was studied [35]. The classical HDP starting from an acidic solution was compared with catalysts prepared with HDP starting from a high pH solution (pH = 11) with ammonia addition. A very strong interaction formed between the silica and cobalt of the cobalt silica supported catalyst prepared at a low pH. The catalyst contained mainly cobalt hydrosilicates requiring a high reduction temperature of 600ºC to yield metallic cobalt. The use of a high reduction temperature leads to sintering of the cobalt crystallites. Well dispersed Co_3O_4 crystallites with an average crystallite size of 4 nm were formed on silica using homogeneous deposition-precipitation (HDP) at a high pH. The reduction temperature was also lower at 500ºC. A low loading of cobalt on carbon nanofibers (CNF) was obtained with the catalyst prepared at a low pH due to a very weak interaction between the cobalt and the carbon nanofibers. As stronger interaction was observed with the catalyst prepared at a high pH, which also reduced at a lower temperature. A higher catalytic activity in the Fischer-Tropsch synthesis was obtained with these catalysts prepared at high pH.

In the sol-gel method cobalt nitrate is dissolved [23,36] (e.g. in ethylene glycol [36]). Tetraethyl ortho-silicate and pore size modifiers are added to the solution. Water and ethanol are added and a clear sol is formed. This is hydrolyzed by increasing the temperature to from a transparent gel that is subsequently dried and calcined. This process allows mastering and adjusting surface area, porosity and particle size of prepared catalysts. FTS activity testing was conducted on different prepared amorphous silica catalysts according the sol-gel technique. The metal salts were incorporated into the structure of the support. After the reduction it was shown that the catalysts were active for the Fischer-Tropsch synthesis.

In the above outlined methods, the catalytically active material is distributed over the whole support. In eggshell-type of catalysts the catalytically active material is concentrated close to the external surface [23,24,37]. This type of catalysts is used to overcome diffusion limitations in catalysts pellets (particularly of interest for fixed bed applications, where the necessary usage of large pellets may induce mass and heat transfer limitations). These catalysts are prepared by controlled impregnation and/or drying.

Cobalt catalysts can also be incorporated in a monolith [23,38], Monolithic catalysts consist of long parallel channels separated by thin walls. The walls are made of cordierite on which a high surface area support can be wash coated. Cobalt active phase is deposited by co-impregnation or homogeneous deposition on to the wash coat. The largest advantage of monolithic catalysts is a low pressure drop in a large scale reactor. Two methods were applied to prepare square channel cordierite catalysts for FTS [38]. The first method was to wash coat a Co-Ru/γ-Al_2O_3 catalyst on to the monolith and the second method was to wash coat γ-Al_2O_3 on to the monolith followed by impregnation of the active phase and promoter on the wash coat. The catalyst prepared according the second method showed better results for CO-conversion, C_{5+} selectivity and chain growth probability in the FTS.

Cobalt nitrate and cobalt acetate are the most common precursors in the preparation of cobalt catalyst [23]. Cobalt precursor decomposition is an important step in catalyst preparation [33,39]. The heat released during decomposition has an effect on dispersion and reducibility [39]. Decomposition of cobalt nitrate in air is slightly endothermic and decomposition of cobalt acetate is highly exothermic in air [33]. Smaller cobalt particles with higher cobalt dispersion were observed when cobalt nitrate was decomposed at lower temperatures. The lower temperatures resulted in slower decomposition of the cobalt precursor. This was observed when Co_3O_4 crystallite sizes of cobalt silica supported catalysts were plotted as a function of the calcination temperatures. Low calcination temperatures can prevent sintering of the cobalt oxide particles. Exothermic decomposition of a cobalt precursor, e.g. cobalt acetate, can lead to an uncontrolled high rate of decomposition of the cobalt precursor and could lead to the formation of cobalt support mixed compounds that do not produce an active phase for the FTS. A series of silica supported cobalt catalysts was prepared via impregnation with cobalt acetate. The decomposition of the catalysts was studied using differential calorimetry with thermogravimetric analysis.

Higher concentration of α-orthorhombic cobalt silica was detected in the catalysts prepared via rapid and highly exothermic decomposition of cobalt acetate.

2.3.3 Activation of a supported cobalt Fischer-Tropsch catalyst

Cobalt-based Fischer-Tropsch synthesis is catalysed by the surface of metallic cobalt [24,40]. Hence, the activity of the cobalt-based Fischer-Tropsch catalysts is strongly dependent on the molar fraction of cobalt phases and the number of cobalt metal surface sites. The number of cobalt metal sites in the catalyst is a function of the size of the cobalt metal particles and extent of reduction. The number and density of available cobalt metal sites are important for enhancing the catalytic performance of cobalt supported catalyst [40].

The type of support, cobalt loading and the addition of a noble promoter are important in the kinetics of the reduction [31]. The reduction of supported Co_3O_4 to metallic cobalt proceeds via two-steps with the intermediate formation of CoO [31,41]:

$$\text{First step:} \quad Co_3O_4 + H_2 \rightarrow 3CoO + H_2O$$

$$\text{Second step:} \quad 3CoO + 3H_2 \rightarrow 3Co^0 + 3H_2O$$

On Co/SiO_2 catalysts, the first reduction step occurs in the temperature range of 200º - 300ºC [41]. The reduction of the second step is strongly influenced by the crystallite size with the smaller crystallite size below 6 nm being more difficult to reduce than larger crystallites of 20 – 70 nm [31]. High reduction temperatures are required if there is a strong interaction between the support and cobalt. This could lead to agglomeration and the formation of large Co metal particles.

Two peaks were observed during temperature programmed reduction (TPR) of Co/γ-Al_2O_3 catalysts (with a loading of 15 - 25 %) that were calcined at a low temperature (350ºC) [31]. The first peak was a sharp peak around 350ºC and a very broad second peak were observed that extends to temperatures as high as 800ºC. Higher cobalt loadings resulted in easier to reduce Co_3O_4 crystallites and can result in one broad asymmetric peak in the range of 300º – 800ºC. Higher loadings lead to larger cobalt oxide crystallite sizes that weaken the interaction with the support.

A more complex interpretation was given for the TPR profile for a 9.1 % CoO/γ-Al_2O_3 catalyst that was calcined at 400ºC [31]. Four reduction regions were described during the reduction:

- i) 277-377ºC is the reduction of Co_3O_4
- ii) 450-500ºC is the reduction of well-dispersed Co^{3+} surface ions
- iii) 600-650ºC is the reduction of well-dispersed Co^{2+} surface ions
- iv) above 825ºC the reduction of cobalt aluminate crystallites.

The reduction of cobalt supported on α-Al_2O_3 is more facile than the reduction of cobalt supported on γ-Al_2O_3 [42]. The TPR-profile for both Co/α-Al_2O_3 and Co/γ-Al_2O_3 showed four maxima, which were ascribed to the reduction of residual cobalt nitrate (200°C for Co/α-Al_2O_3 and 250°C for Co/γ-Al_2O_3), the reduction of Co_3O_4 to CoO (295°C for Co/α-Al_2O_3 and 335°C for Co/γ-Al_2O_3), reduction of CoO, (425°C for Co/α-Al_2O_3 and 585°C for Co/γ-Al_2O_3),and the reduction of a more diffuse oxide phase interacting with the support (555°C for Co/α-Al_2O_3 and 940°C for Co/γ-Al_2O_3). The shift in the reduction temperature was attributed to a weaker interaction between the support and the cobalt oxide phase, due to the larger crystallite size of α-Al_2O_3 and possibly a more relaxed surface.

Noble metals, i.e. ruthenium (Ru), rhodium (Rh), platinum (Pt) and palladium (Pd), contribute to easier reduction of cobalt oxides to active metallic cobalt [23]. The addition of 0.5 % Pt to a 15 % and 25 % Co/Al_2O_3 catalysts shifted both reduction peaks to lower temperatures [31]. The first peak was more affected than the second peak. The temperature was lowered from a temperature range of 300 – 400ºC to 150 – 200ºC. Addition of platinum leads to an increase in the extent of reduction, when the reduction is carried out at a given temperature for a given time.

High water concentrations that developed during fast reduction of oxides and nitrates could lead to sintering and therefore lowering the metal dispersion [24] in addition to the formation of cobalt-support compounds [43]. Cobalt dispersion during reduction can be improved with high H_2 flow rates and slow temperature ramping to prevent high water concentration.

The smallest cobalt crystallite was obtained with strongly interacting support like aluminium oxide (Al_2O_3) in comparison with a support with a weak interaction, e.g. silica (SiO_2) [31]. H_2 chemisorption results showed higher active site densities are obtained with small crystallites. The size of the crystallite has a larger influence on the density of the active sites than extent of reduction and promotion.

The commercial Fischer-Tropsch catalyst, cobalt on alumina, contains a high loading of cobalt, up to 30g per 100g [44]. The high loadings are to weaken the interaction with the support. Increasing the cobalt crystallite size weakens the interaction with the support, but it would be economically beneficial to obtain commercial cobalt Fischer-Tropsch catalysts with lower cobalt loadings. The lower loading would require small well dispersed cobalt crystallites.

The reduction of the crystallite can be enhanced with a noble metal because it is the second step of reduction that depends strongly on the interaction with the support [31]. However, these small promoted crystallite catalysts have an initial high activity, but deactivate quite rapidly. The smaller clusters on the lower loaded cobalt supported catalyst appear to be more prone to sintering.

Repeated oxidation-reduction cycles on a 2 % Ru – 15 % Co/Al_2O_3 catalyst [45] showed that cobalt becomes systematically more reduced and that the reduction of the second step becomes easier. The reduction temperature of the first reduction step shifts to higher temperatures, but the temperature of the second step shifts to lower temperatures. Extended X-ray absorption fine structure (EXAFS) and X-ray absorption near edge spectroscopy (XANES) results showed that the average cobalt metal cluster size increases with increasing of number of oxidation-reduction cycles. The increase in cluster size showed an increase in reduction due to the weakening of the cobalt support interaction. This ripening technique via oxidation-reduction cycles improved the mixing of the cobalt and ruthenium that leads to an easier reduced catalyst.

Other gases than hydrogen can be used for activation, e.g. carbon monoxide (CO) or synthesis gas (H_2 and CO mixture) [46,47]. Introduction of CO into the reducing gas limits the cobalt compound formation [46]. *In-situ* XRD was also done on a calcined 10 wt % Co/SiO_2 catalyst with three different activation gases, namely H_2, CO and synthesis gas [47]. The activation treatment was conducted over a temperature range of 275°C to 500°C. Different temperatures were noted during each stage of the reduction of Co_3O_4 with different gases. The different temperatures observed during the two stages of reductions with different activation gases are summarised in Table 2.1. In particular, the temperature of transformation of CoO to Co^0 is much higher with CO and synthesis gas activation, which might be ascribed to a kinetic inhibition by CO.

Table 2.1 *Different reduction temperatures of a 10 wt % Co/SiO_2catalyst with different activation gases i.e. H_2, CO and synthesis gas [47]*

	H_2	CO	synthesis gas
Stage 1	275°C	325°C	300°C
Stage 2	350°C	500°C	500°C

2.3.4 The value of a model supported catalyst in research studies

Industrial supported catalysts are complex because they usually have high surface area, one or more catalytically active materials and chemical and structural promoters. Small particles can also be hidden in the pores of industrial supported catalysts making it difficult to gain information with certain characterization methods, e.g. X-ray photoelectron spectroscopy (XPS). In order to develop new generations of supported catalyst, it is important to gain knowledge on more simplified systems to understand complex systems better [48].

The term “model system” implies that a simplified system is used to imitate a complex catalyst. A single crystal of metals has often been used in model studies in catalysis for important catalytic reactions. One drawback of these systems is that the catalyst support is excluded from the catalyst system. Several possibilities for modelling catalysts exist between the industrial catalyst with a high surface area and porous support and the surface of a single crystal (see Figure 2.1) [48].

The first step to simplify a complex system would be to leave out all the promoters and to study a monometallic catalyst. This type of catalyst is well suited for reaction kinetic studies and spectroscopic characterization. It is however not suited for surface science. The first step to a model system is to replace the porous support with a non-porous spherical support. These systems are useful in studying particle morphology and metal support interaction by transmission electron microscope. Flat support systems are good for surface sensitive techniques that are based on the detection of electrons and ions [48].

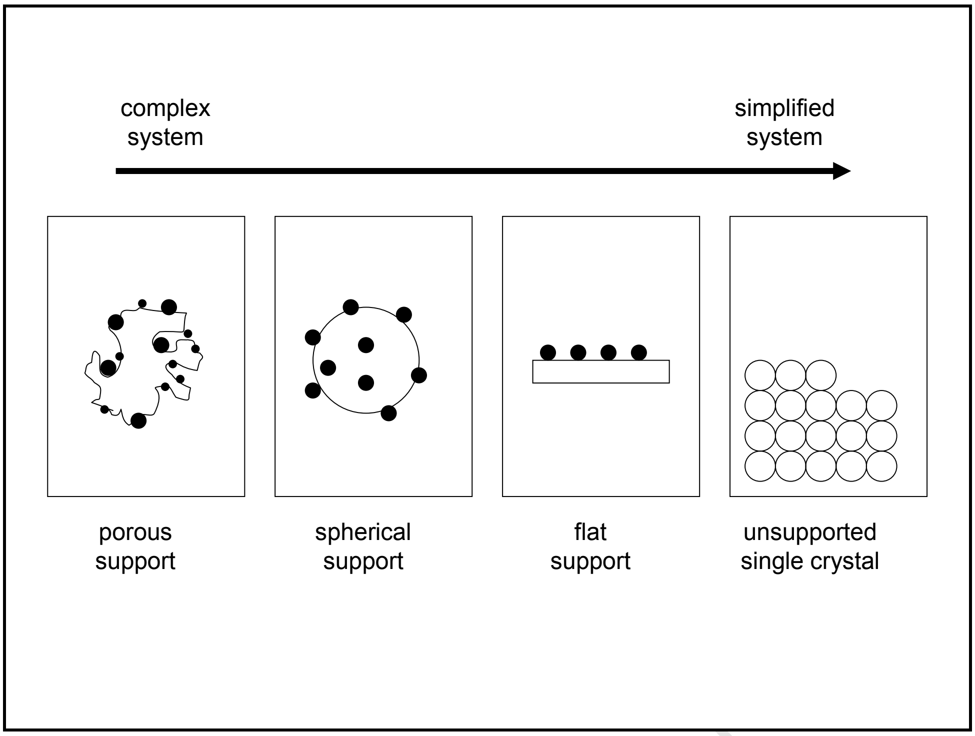

Figure 2.1: *Possible model catalyst systems [48]*

Several characterization techniques are useful in studying model catalysts. X-ray photoelectron spectroscopy (XPS) is a technique to determine the composition of model catalysts. Transmission electron microscopy (TEM) can be used to determine the morphology of small particles. TEM can also be use to study particle sintering and migration. The main advantage with TEM is direct visualization of sintering and re-dispersion of model catalysts. Mechanistic processes such as migration and spreading can be directly observed [48].

In-situ TEM studies were conducted on a spherical model cobalt catalyst [4]. The sample was reduced and imaged under a reduction atmosphere and Fischer-Tropsch synthesis (FTS) conditions with different H_2/CO ratios. It was shown that with the combination of Wulff construction and *in-situ* TEM, it was possible to gain information on exposed faces under different reaction conditions. Cobalt particles on spherical silica support did not change under model Fischer-Tropsch conditions.

Other useful techniques are low energy ion scattering (LEIS), secondary ion mass spectrometry (SIMS), electron energy loss spectroscopy (EELS), scanning tunnelling microscopy (STM) and temperature programmed desorption (TPD). STM is also useful like TEM in studying directly the morphology of small particles. *Real*-space imaging is possible with STM [48].

Thermal desorption (TPD) is used to study adsorption. Another use of thermal desorption is to measure the total metal surface area. Small clusters, that are too small for TEM, can be identified by TPD. The metal area, in conjunction with the total amount of metal deposited, can also be used to calculate the percentage of metal exposed and the particle average diameter [48].

Silica, alumina, titania, zinc oxide, zirconia, carbon, mica, ceria and lanthana are all supports that have been used in studies of model systems. Almost all flat silica model systems are made by oxidation of silicon wafers or reactive evaporation of silica in oxygen [49], although silica spheres have been applied as well [4].

Several crystallographic modifications of alumina exist that make the structural chemistry of alumina complex. Various flat aluminium oxides have been used to model porous alumina supports, e.g. single crystalline α-aluminium oxide (α-Al_2O_3), thermally oxidised aluminium single crystals, aluminium foils, evaporated films, anodized films and films made by reactive evaporation [48]. Single crystalline supports, α-Al_2O_3, are thermally stable and can be easily cleaned. Thin, flat γ-Al_2O_3 can be made directly by thermal oxidation and is a good replica for the high surface area α-alumina.

There are two important requirements for model systems to be able to be subjected to reaction conditions [48]. Firstly the model system should be thermally stable against sintering, volatilization and reaction with the support, at the temperature of the catalytic reaction. Secondly that the number density of particles per unit surface area is high enough for both reactivity and spectroscopic studies.

There are several techniques to deposit metal particles on a substrate. Metal deposition by evaporation is the most applied method [48]. This method leads to a Gaussian-like distribution in particle size. Other methods are chemical vapour deposition and wet chemical impregnation. Almost all supported catalysts are prepared by wet chemical impregnation. In the industry the catalyst is prepared by pore volume impregnation or “incipient” wetness impregnation. For flat supports the spin-coating technique is developed to fill the pores. Wet chemical methods make it possible to study on a model scale the surface chemistry of catalyst preparation, which has industrial relevance.

Model catalysts have played a significant role in understanding strong metal-support interaction (SSMI) effect. TEM images on a study of a Rh/TiO_2 catalyst after reduction showed the presence of a amorphous surface layers on the metal particles [48]. It was concluded that SSMI effect is the incorrect name for another phenomenon. This was explained by the blocking of adsorption sites due to the covering of metal particles by mobile oxide species from the support.

2.4 Deactivation of supported cobalt Fischer-Tropsch catalysts

An ideal catalyst will be a catalyst that does not change and has eternal life. This is however not the case, since catalyst lose some of their activity with time (deactivation). The catalyst is deactivated when it has lost so much of its initial activity that it must be replaced or regenerated [49,50]. During Fischer-Tropsch synthesis the cobalt catalyst deactivates with time on stream [3-5, 7-11, 51-57]. Regeneration or replacement of the deactivated catalyst is necessary to maintain the reactor productivity with minimum fresh catalyst make-up [51].

Deactivation of a supported-cobalt catalyst was shown in a slurry bubble reactor [3]. The FTS $Co/Pt/Al_2O_3$ catalyst was tested in a 100 bbl/day slurry bubble column reactor. The reactor was operated under realistic FT conditions, i.e. 230°C, 20 bar and H_2 + CO conversion between 50 % and 70 %. The feed gas composition was 50 vol % H_2 and 25 vol % CO. The catalyst contained 20 mass % Co and 0.5 mass % Pt. The relative intrinsic activity factor (Riaf) was shown to decline with time on line (the Riaf of the catalyst is the activity of the catalyst that is determined with the FT rate, relative to the activity after one day on line - see Figure 2.2). Deactivation can be observed as the decline in activity, which starts to level off after 30 days on line.

In the simplest case, the catalytic activity is proportional to the number of active sites [49]. Catalyst deactivation can then be due to (i) a decrease of the number of active sites (e.g. decrease due to poisoning or sintering) , (ii) a decrease of the quality of the active sites and (iii) a degradation in accessibility of the pore space.

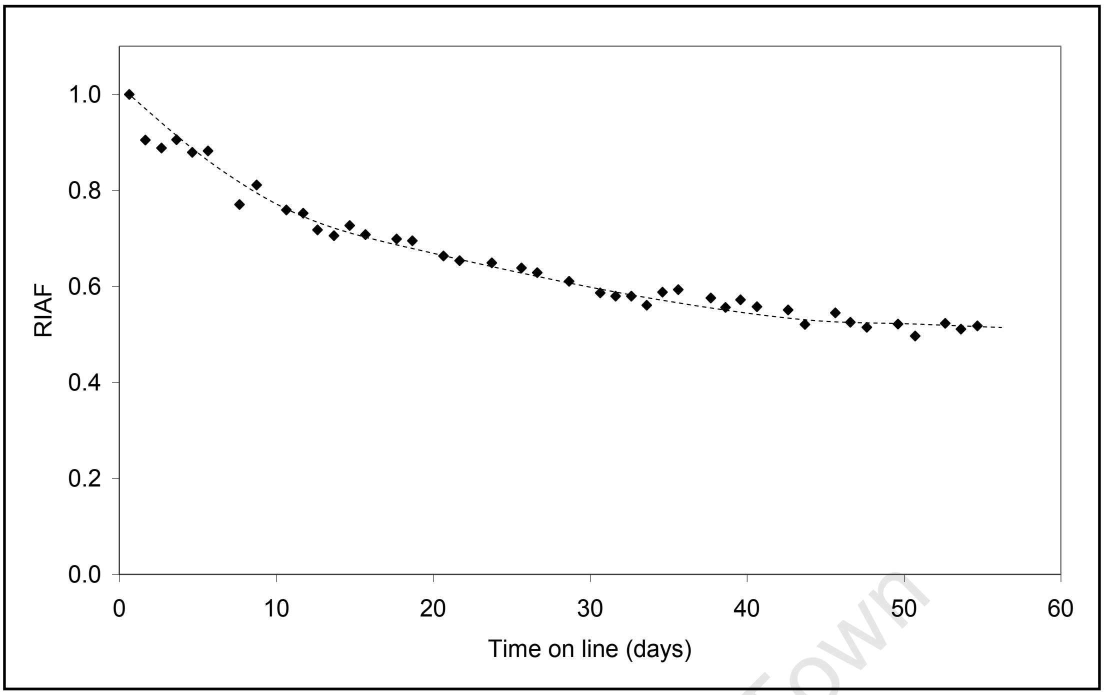

Figure 2.2: *Relative intrinsic activity factor (Riaf) during Fischer-Tropsch synthesis over a Co/Pt/Al_2O_3 catalyst under industrially relevant conditions [3]*

A number of different mechanisms are currently postulated for the deactivation of cobalt supported catalyst, i.e.

I. Poisoning by sulphur and/or nitrogen containing compounds in the synthesis gas feed [7,52]
II. Oxidation of active cobalt metal to inactive cobalt oxide [3,53,54]
III. Cobalt-support compound formation like cobalt aluminates [4,54]
IV. Sintering of small cobalt crystallites into larger ones [5,7,11,55]
V. Surface reconstruction [56]
VI. Carbon formation [4,7,57]

2.4.1 Poisoning of active metal surface

Poisoning is the strong chemisorption of reactants, products or impurities on active sites that are available for catalysis. There are different mechanisms in which way poisons can affect catalysts activity. A strong adsorbed sulphur atom can physically block at least one 3- or 4-fold adsorption/reaction sites and 3 or 4 top sites on a metal surface. The adsorbed poison can also blocks access of adsorbed reactants to each other and can slow the surface diffusion of adsorbed reactants [50]. Furthermore, the strong chemical bond poison can electronically modify neighbouring metal atoms and thereby modifying the surface metal's ability to adsorb and/or dissociate reactant molecules. In addition to these effects, strongly adsorbed poisons may induce surface reconstruction.

Experiments, in which sulphur compounds were co-fed with synthesis gas during the FTS over an alumina-supported platinum promoted cobalt catalyst in a micro-slurry reactor [52], showed that sulphur has a negative effect on the activity (see Figure 2.3). Hydrogen sulphide (H_2S), carbon oxysulfide (COS) and mercaptans were added as poisons during these experiments at a concentration of 100-400 vppb in the feed gas. A drastic decline in activity is observed after 190 vppb of H_2S was added. Sulphur poisoning is irreversible. The sulphur was adsorbed completely on the catalyst and a sulphur mass balance of about 85 % was detected by analysing the sulphur in the feed gas, tail gas and spent catalyst.

The impact of nitrogen containing compounds on the activity of a supported cobalt catalyst for FTS is less severe than sulphur [7]. Poisoning by nitrogen containing compounds, e.g. hydrogen cyanide (HCN) and ammonia (NH_3) can be reversed with a mild hydrogen treatment.

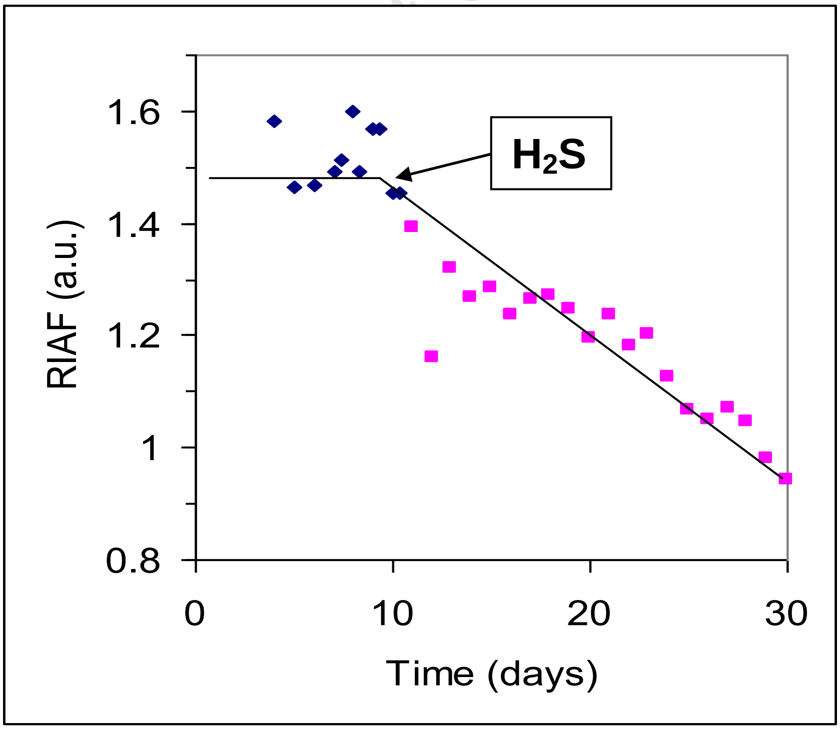

Figure 2.3: *Relative intrinsic activity factor (Riaf) during co-feeding of H_2S over a $Co/Pt/Al_2O_3$ catalyst during Fischer-Tropsch synthesis [52]*

2.4.2.1 Oxidation of the catalytically active metal

During the Fischer-Tropsch synthesis CO and H_2 react over metallic cobalt to produce hydrocarbons. In this process the carbon and oxygen bond is broken and the surface oxygen reacts to form water as a by-product. During realistic FT conditions, i.e. 230°C, 20 bar, (H_2 + CO) conversions between 50 and 70 % and a feed gas ratio of 50 vol % H_2 and 25 vol % CO, a water partial pressure of 4 – 6 bar is created [3]. Under these conditions, the oxidation of bulk metallic cobalt to Co(II)O is not feasible [54]. The water partial pressure relative to the hydrogen partial pressure must be in excess of 128 bar at 220°C in order for the oxidation of cobalt to Co(II)O to become thermodynamically feasible.

Supported cobalt-based Fischer-Tropsch catalysts typically contain cobalt crystallites with a diameter well less than 100 nm. The thermodynamics of the oxidation of nano-sized cobalt requires the inclusion of the change in the surface energy contribution [58]. The inclusion of the change in the surface energy upon oxidation of metallic cobalt to Co(II)O results in a reduction in the stability of metallic cobalt. Co crystallites with a diameter less than 2 nm are thermodynamically not stable under realistic FT conditions and can transform into Co(II)O [59]. This indicates that very small crystallites of commercial catalyst will not be regenerated and remain in the inactive oxide state under realistic FT conditions. They may react further to form cobalt-surface species, e.g. Co aluminates due to the intimate contact with the support [54].

In a study to determine if oxidation does occur under realistic Fischer-Tropsch conditions, representative samples were taken over a time period during the Fischer-Tropsch synthesis over a $Co/Pt/Al_2O_3$ catalyst [3]. The crystallite size of metallic cobalt in the catalyst was predominantly 6 nm. XANES analyses were conducted on reference compounds (CoO, Co_3O_4, $CoAl_2O_4$ and Co^0) as well as a calcined sample, a freshly reduced catalyst and the spent catalyst samples taken over a certain time period. The calcined catalyst sample was very similar to reference compound of Co_3O_4. In Figure 2.4 it is shown that with time on line, the $Co/Pt/Al_2O_3$ catalyst becomes more reduced from freshly reduced sample to a sample that was taken 125 days on line. The sample that was left on line for 125 days compared well with the reference sample of Co^0. It was speculated that reduction under realistic FT conditions occured due to the (i) the relative high H_2 partial pressure, (ii) the presence of CO or (iii) sintering that caused larger Co crystallites that were easier to reduce.

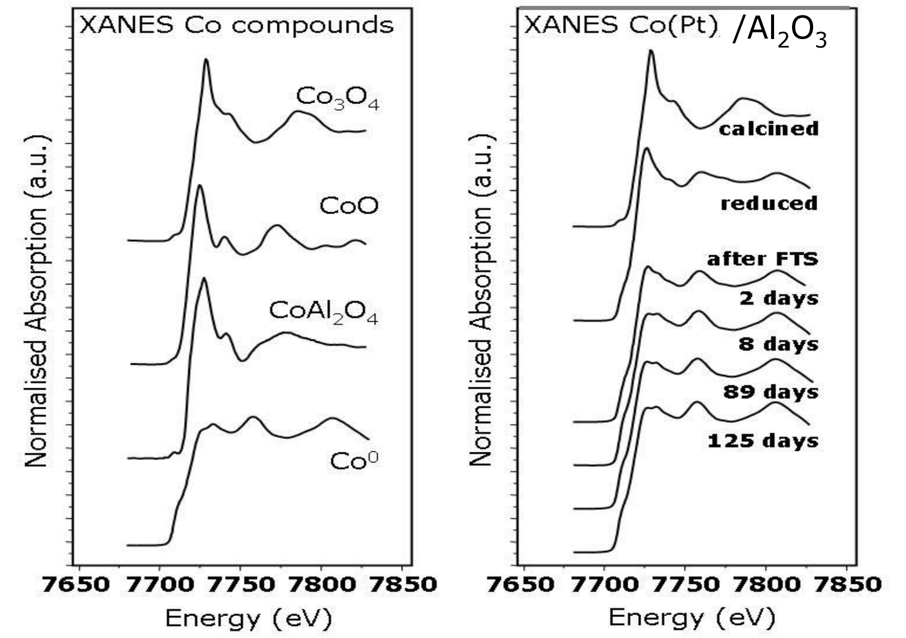

Figure 2.4: *XANES analyses of reference compounds and a series of spent $Co/Pt/Al_2O_3$ catalyst samples [3]*

2.4.3 Formation of cobalt-support compounds (cobalt aluminates)

It has been postulated that the conversion of Co/Al_2O_3 to cobalt aluminate ($CoAl_2O_4$) needs to proceed via CoO as an intermediate product [54]:

$$Co + H_2O \rightarrow CoO + H_2$$
$$CoO + Al_2O_3 \rightarrow CoAl_2O_4$$

The conversion of Co and Al_2O_3 to $CoAl_2O_4$ is thermodynamically favoured, but it is unlikely that it will occur. The oxidation of bulk phase metallic cobalt to CoO or Co_3O_4 is thermodynamically unlikely and the oxidation to $CoAl_2O_4$ is therefore kinetically restricted during typical FT conditions.

The formation of $CoAl_2O_4$ might be kinetically hindered at temperatures applicable to the Fischer-Tropsch synthesis, but it might be accelerated due to the presence of water [7]. A 20 wt % Co/Al_2O_3 catalyst promoted with 0.05 wt % Pt was tested under realistic FT conditions varying the water partial pressure between 1- 10 bar [4]. XANES studies showed that the catalyst underwent reduction compared to the fresh catalyst. The formation of cobalt aluminates was observed at higher water partial pressures. The cobalt aluminates formed at the expense of CoO and not metallic cobalt. CoO existed as 2-3 nm crystallites strongly interacting with the support and therefore difficult to reduce.

2.4.4 Sintering

Sintering is the loss of catalytic surface because of crystallite growth of the catalytically active phase. It may also occur due to loss of support area because of collapse of the support or because of pores collapsing of the active phase [50]. Sintering decreases the number of available active sites for a given amount of supported metal catalyst by decreasing the total surface area of metal on the support via an increase in the size of the metal crystallites [60].

Three mechanisms can occur during sintering [50], i.e. (i) crystallite migration, (ii) atomic migration and (iii) vapour transport at very high temperatures. Crystallite migration involves the migration of entire crystallites over the support surface followed by collision and coalescence. Atomic migration involves the detachment of metal atoms from crystallites over the support surface and capture by larger particles (see Figure 2.5). Sintering processes usually take place at very high reaction temperatures (e.g. > 500°C) and are accelerated by water vapour. Temperature, gas atmosphere, metal type, metal dispersion, promoters / impurities and support surface area are all factors affecting metal particle growth on supported catalysts [50].

Sintering is strongly temperature dependent [49.50]. The melting point of the metal plays an important role because the solid-state diffusion becomes faster when the temperature is closer to the melting point. The Tamman and Hüttig temperatures indicate at which temperature sintering may occur. The mobility of the metal atoms increases with an increase in temperature. Metal atoms at defects become mobile when the Hüttig temperature is reached. The Hüttig temperature for cobalt is 253°C, which is in the temperature range of Fischer-Tropsch synthesis.

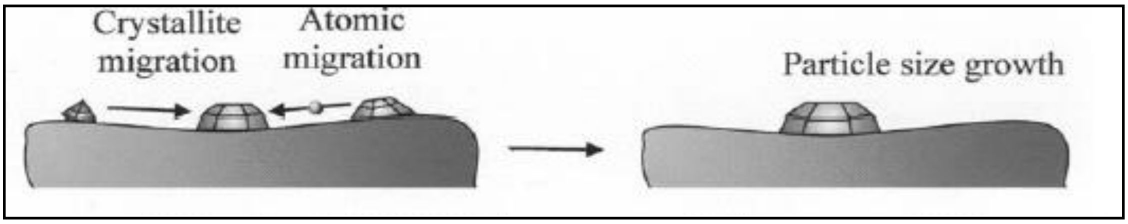

Figure 2.5: *Atomic migration and crystallite migration during sintering [61]*

The crystallite size of cobalt in representative samples of a Co/Pt/Al_2O_3 Fischer-Tropsch catalyst that were tested in a 100 bbl/day slurry bubble column reactor operating under realistic Fischer-Tropsch conditions was determined using TEM and H_2 chemisorption (see Figure 2.6) [5]. Individual cobalt crystallite sizes of the freshly reduced catalyst were between 4 and 12 nm with an weighted area average of 8.6 nm. The cobalt crystallite sizes increased rapidly over the first 10 days of the Fischer-Tropsch synthesis from 10 nm to 14-16 nm. The cobalt crystallites size seems to stabilise after 10 days on line. The loss of surface area was confirmed with H_2 chemisorption results. Bezemer et al. [55] correlated the sintering of a carbon nanofiber supported cobalt catalyst to the presence of a high water partial pressure.

2.4.5 Surface reconstruction

One of the elementary steps in the FTS process is the dissociation of carbon monoxide (CO) into carbon (C) and oxygen (O). The carbon will react with hydrogen to form hydrocarbons. A side reaction is for the carbon to stay on the cobalt metal surface and/or to convert into different carbon species. DFT-studies showed that adsorbed C on Co(111) can be responsible for surface reconstruction going from a compact surface to a more open one, i.e. a transformation from Co(111) to Co(100) [56]. This was not possible with adsorbing O, CO, CH_2 and CH. Carbon was also the only species that could induce the clock reconstruction of the fcc-Co(111) surface. This unique behaviour of C is related to its stability in 4-fold hollow site with 5 neighbouring metal atoms.

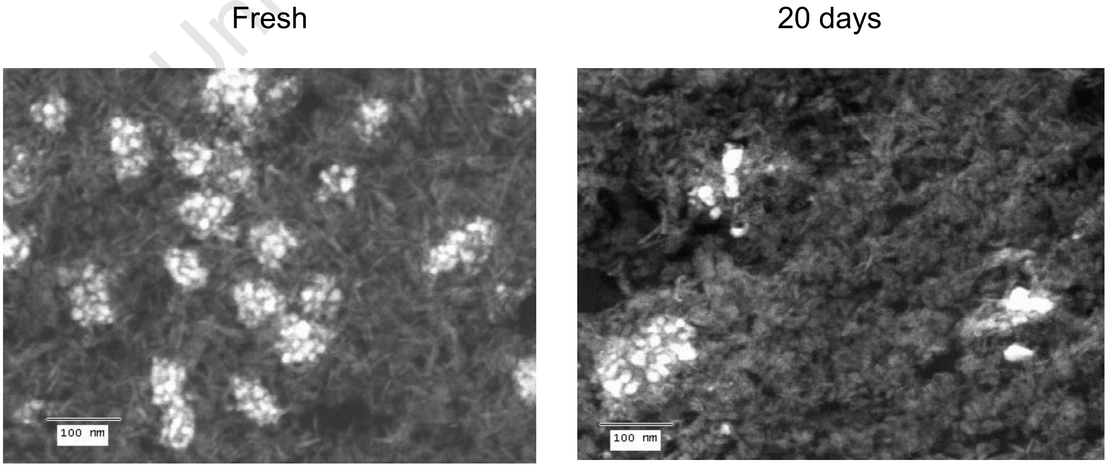

Figure 2.6: *TEM image of a freshly reduced Co/Pt/Al_2O_3 catalyst (left) and after 20 days exposure to industrial Fischer-Tropsch conditions (right) [7]*

2.4.6 Carbon deposition

Various types of carbonaceous species can be formed on catalyst surfaces during catalytic reactions [4].

Carbon is a product of carbon monoxide (CO) disproportionation [1], which may recombine [62] to form graphene like overlayers [59,63]. This may occur when the carbon on the surface is not rapidly converted to form hydrocarbon (CH_x) intermediates. The possible routes of carbon formation during FTS on cobalt supported catalyst are illustrated in Figure 2.7. A bulk carbide phase (Co_2C) will be formed if the carbon diffuses into the bulk metal.

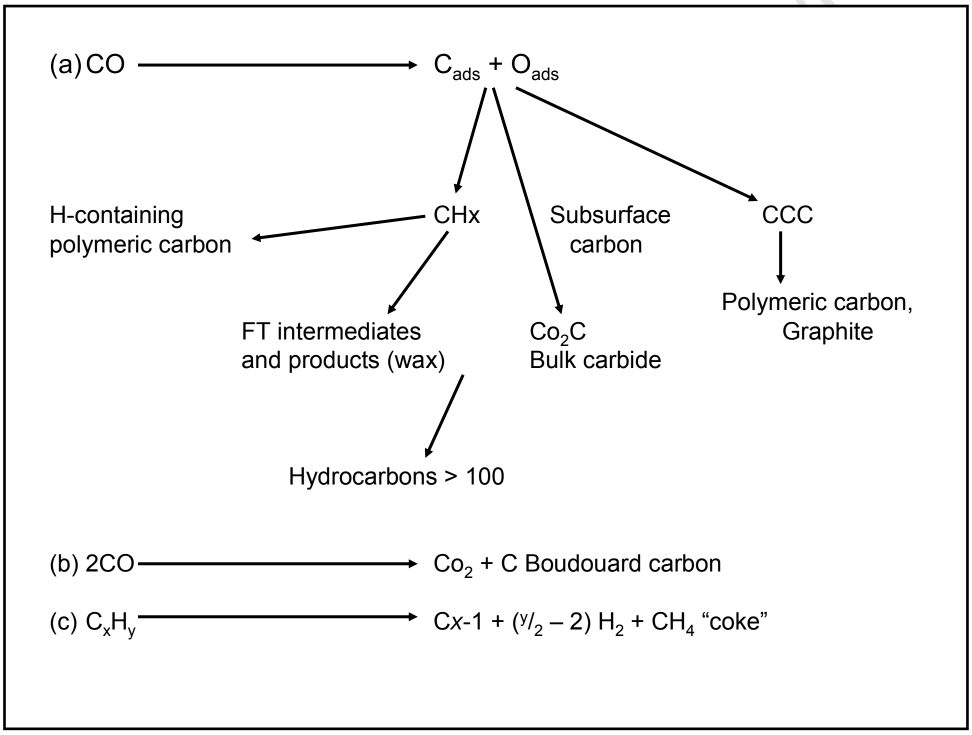

Figure 2.7: *Possible routes for carbon formation of coke deposition on supported cobalt catalyst during the Fischer-Tropsch synthesis [4,64]*

Other potential routes to unwanted carbon formation include deposition of Boudouard carbon and also further reactions of the Fischer-Tropsch products (hydrocarbons) yielding coke [4,49,64]. Coke consists of polymerised hydrocarbons and is produced by decomposition or condensation of hydrocarbons on catalyst surfaces.

Catalytic reactions accompanied by carbon or coke formation can be divided in a structure-sensitive or a structure-insensitive catalytic reaction [50]. During coke-sensitive reactions, unreactive coke is deposited on active sites leading to a decline in activity. Relative coke precursors are in formed on active sites during coke-insensitive reactions. This formed coke is readily removed by hydrogen. Fischer-Tropsch synthesis (FTS) is said to be an example of a coke-insensitive reaction.

Carbon formation and deposition on supported metal catalysts is illustrated in Figure 2.8 [50]. Carbon may (i) chemisorb strongly as a monolayer or physical adsorb in multi-layers that can block access of reactants to metal surface sites, (ii) totally encapsulate a metal particle and cause total deactivation of that particle and/or (iii) plug pores that reactants cannot access crystallites inside the pores. In extreme cases, strong carbon filaments may build up inside the pores that can cause catalyst break-up (catalyst dusting).

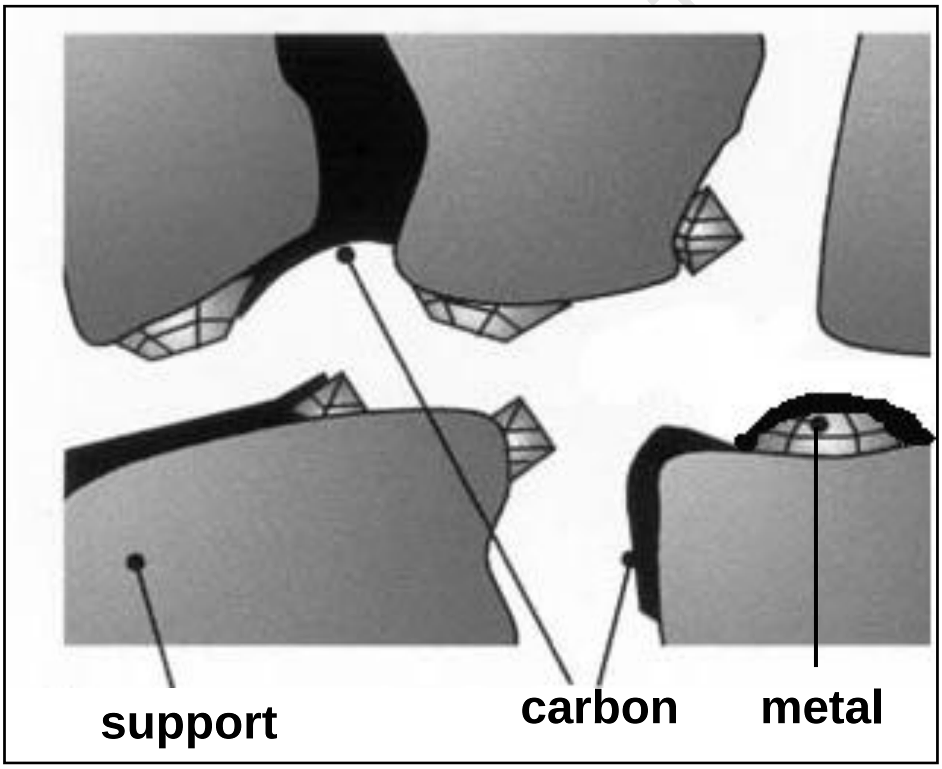

Figure 2.8: *Carbon formation on supported metal catalysts [61]*

To determine whether carbon was deposited during extended Fischer-Tropsch synthesis runs, representative samples were taken over a time period during the FT synthesis of a FTS Co/Pt/Al_2O_3 catalyst that was tested in a 100 bbl/day slurry bubble column reactor and analysed using temperature programmed (TP) techniques, energy filtered transmission electron microscopy (EFTEM) and high sensitive low energy ion scattering (HSLEIS) [4,57,64] was used to determine the amount, reactivity and location of carbonaceous phases formed under these conditions.

Three broad peaks for the rate of methane formation were observed during temperature programmed hydrogenation (TPH) of the wax extracted catalyst (see Figure 2.9) [4,64], which was assigned to different types of carbon according to literature. The first peak around 250°C indicates the possible presence of surface carbides species, residual wax/hydrocarbons and bulk cobalt carbide. The second peak around 330°C is likely due to residual wax in narrow pores. Polymeric carbon on cobalt or on the support is indicated by the third peak around 445°C.

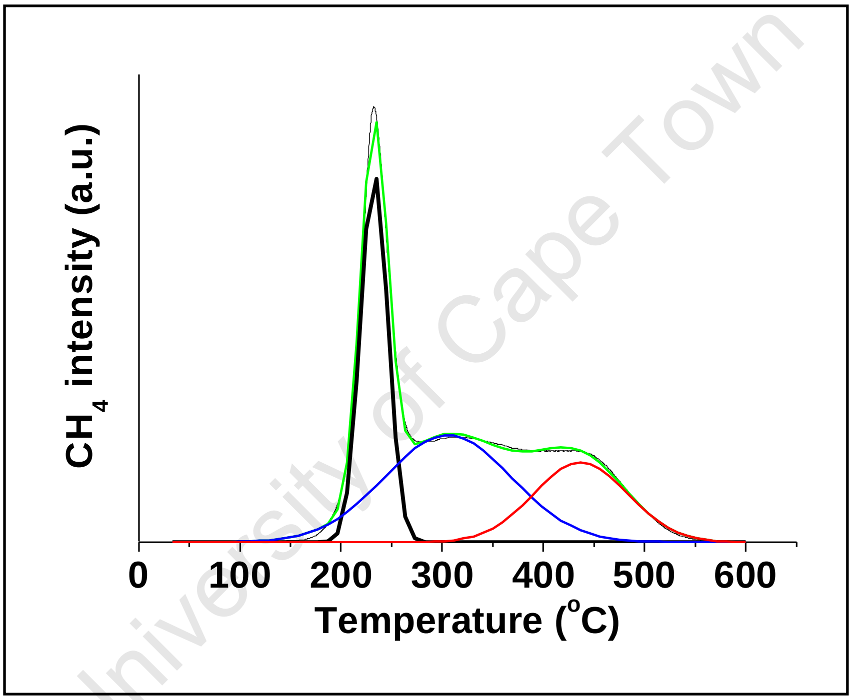

Figure 2.9: *Methane formation in temperature programmed hydrogenation (TPH) of a wax extracted supported cobalt catalyst [57]*

The wax extracted samples with time on line were hydrogenated at 350°C and then exposed to oxygen with a temperature ramp to 900°C to obtain information on the nature of polymeric carbon species. An increase in polymeric carbon species was observed with time on line over a period of 6 months. EFTEM carbon and cobalt maps of the hydrogenated catalyst were used to determine the location of the polymeric carbon, which showed that the carbon was located over the support and over the cobalt phase. HSLEIS experiments showed that polymeric carbon is removed during an oxidative regeneration step (see Figure 2.10). An increase in both aluminium (Al) and cobalt (Co) signal were detected, which implies that the polymeric carbon is located on both the support and the cobalt [57,64].

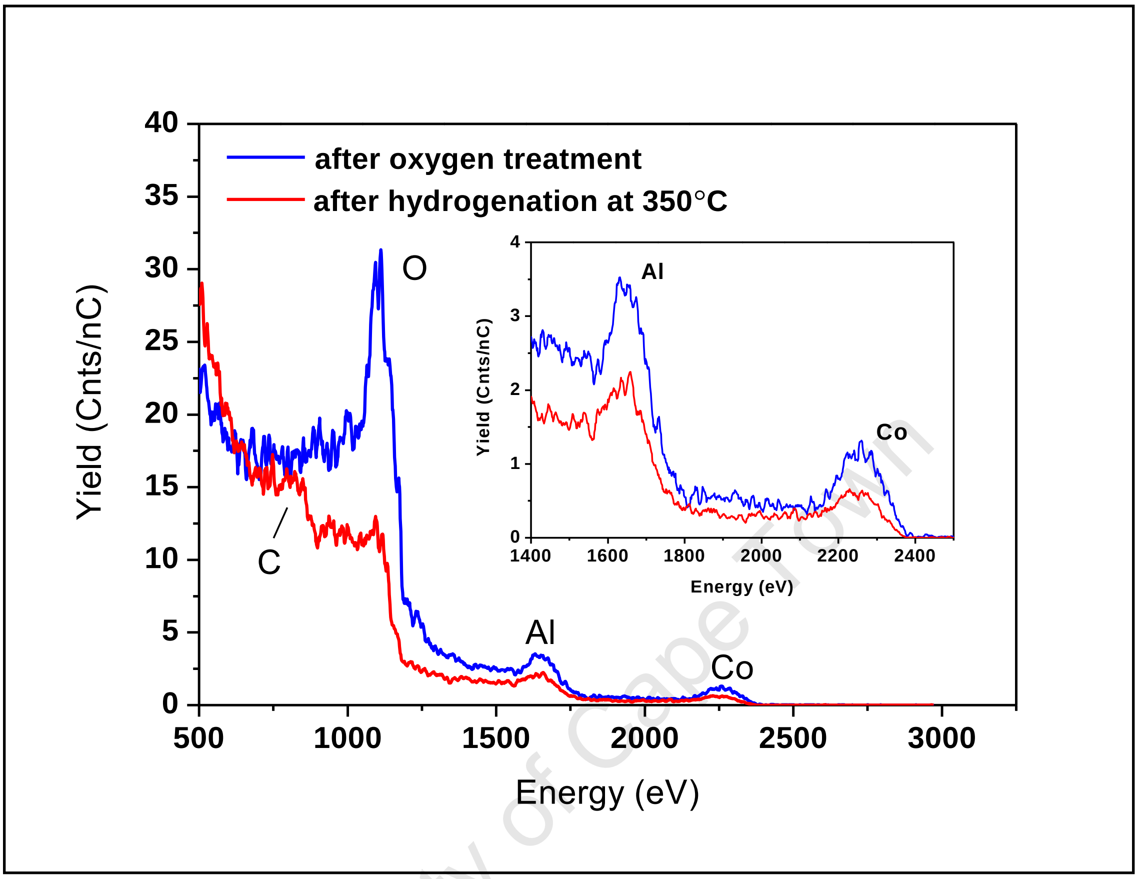

Figure 2.10: *HSLEIS spectrum of a wax extracted supported cobalt catalyst after hydrogenation and oxidation [57]*

2.5 Regeneration of deactivated supported cobalt Fischer-Tropsch catalysts

Catalyst deactivation is the loss over time of catalytic activity and/or selectivity [49,50]. Deactivation time refers to the time after which a catalyst has lost so much of its initial activity that it must be regenerated or replaced. Several regeneration procedures are in use, including rejuvenation techniques which apply milder conditions [49].

In 1942 it was reported in a patent [65] that it was possible to reactivate (regenerate) exhausted cobalt catalyst that had been used for the synthesis of low boiling hydrocarbons such as gasoline from mixtures of carbon dioxide and hydrogen at temperatures above 300°C. It was shown that the original activity of the catalyst could be regained by a hydrogen treatment to remove the paraffin on the exhausted catalyst at 350°C for two hours. The treatment with the hydrogen is continued at 400°C or higher.

In 1953 and 1954 a method was patented [66,67] to regenerate a cobalt catalyst to restore the activity for the catalytic conversion of olefins, carbon monoxide and hydrogen into carbonylic products. The process was a treatment with an oxygen-nitrogen mixture. There are limited studies regarding regeneration of cobalt-based Fischer-Tropsch (FT) catalysts in the open literature [8,68].

Regeneration of the cobalt based Fischer-Tropsch slurry catalyst is a process in which the catalyst is treated in such a way that, after a certain time on stream, it will behave again like a fresh catalyst. There are several methods that are applied to regenerate a spent cobalt-based Fischer-Tropsch slurry catalyst, most of which have been patented. Examples of regeneration processes are *in-situ* and *ex-situ* hydrogen treatment in the presence of liquid hydrocarbons, steam stripping of deactivated catalyst or sequential oxidation-reduction [68].

There are a number of limitations to *in-situ* regeneration because the catalyst is in a slurry phase [68]. Regeneration of a slurry phase catalyst outside the reactor therefore requires a separation step. Syntroleum has been working on Fischer-Tropsch catalyst regeneration both in fixed bed and slurry bubble column reactors [8,9,68]. The fixed bed catalyst regeneration is less complicated than the slurry bubble column catalyst regeneration due to the slurry transport and the transformation from slurry phase to solid phase in the slurry bubble column process.

The Syntroleum approach to catalyst regeneration involves sequential oxidation-reduction reactions. The process involves dewaxing and drying of the slurry catalyst to produce a free flowing powder that can be fluidized. The catalyst is treated with an oxygen containing gas to remove hydrocarbons from the catalyst powder. Finally the catalyst is reduced with a hydrogen containing gas and re-slurried.

Huang et al. also patented a regeneration process of a Fischer-Tropsch slurry phase cobalt catalyst [9] that involves a dewaxing/drying step that delivers a free-flowing powder that undergoes an oxygen treatment followed by reduction step. The oxidation and reduction steps can be repeated. Huang et al. [9] claimed three procedures for the oxidation step where (1) fixed oxygen levels with ramping temperatures or (2) fixed temperature with incremental oxygen levels or (3) a combination of 1 and 2. Analyses of the catalyst showed an improved dispersion and reproducibility, when an oxidation step was conducted with incremental oxygen treatment, resulting in improved catalyst performance. During the oxygen treatment the combustion of hydrocarbons and carbon rich materials competes with the oxidation of reduced metal present in the catalyst. Both reactions may be slow at low temperatures (<232°C). The oxidation of the metal may be further retarded by the organic layer covering the metal. When the layer is removed, the oxidation of the metal can proceed more rapidly. The exothermic nature of the metal oxidation with oxygen can lead to localised high temperatures. High temperatures with limited O_2 availability can lead to pyrolysis of some of the carbon material. Furthermore, a localised high temperature can lead to sintering and affect the metal dispersion. The catalyst also recovered almost 100% of its original activity when high temperature inert gas treatment was used for dewaxing and drying.

Syntroleum has developed a catalyst regeneration process for a cobalt based catalyst that is used in the Fischer-Tropsch synthesis (see Figure 2.11) [8]. This process consists of withdrawing the spent catalyst from the FT reactor(s) and recovering of the catalyst activity through multiple treating steps. The treatment process includes slurry transfer, gravitational slurry setting, catalyst drying, wax stripping, oxidation, and hydrogen reduction. This process has been successfully demonstrated at the Syntroleum GTL demonstration facility in Tulsa, Okalahoma.

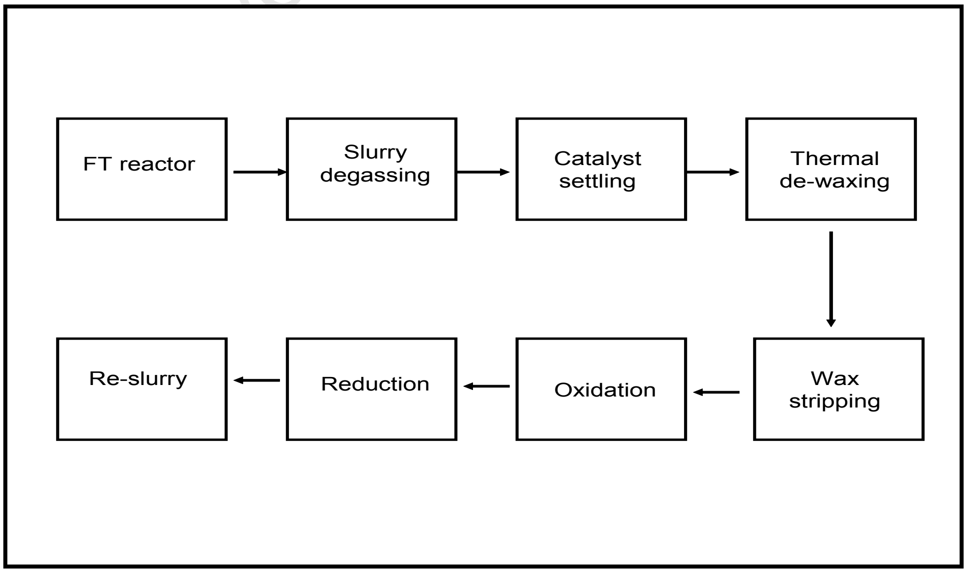

Figure 2.11: *SynmGEN^{TM} process for regeneration of a cobalt-based Fischer-Tropsch catalyst) [8]*

Regeneration process for Fischer-Tropsch catalysts under pressure and utilizing different oxidising agent like steam have also been patented [51]

An activation process referred as a ROR (reduction-oxidation-reduction) treatment has also been patented for regeneration of a partially deactivated Fischer-Tropsch catalyst [69]. The first step of the ROR treatment involves stripping the catalyst with hydrogen to remove heavy wax and/or carbonaceous material that has precipitated on the catalyst during operation as well as a slow reduction process. The second step is an oxidation step to oxidise remaining carbonaceous material into carbon dioxide and water, in which the catalytically active metal is oxidised as well. In the last step the oxidised cobalt is reduced.

Sasol also showed that it is possible to re-verse deactivation mechanisms such as sintering and carbon deposition by regenerated a cobalt catalyst [7,70]. The regeneration procedure consists of a solvent wash step with heptane at 100ºC to remove the excess wax. This was followed by an oxidation step in a fluidised unit using an oxygen/nitrogen mixture that was gradually increased from 3% to 21% to control the exothermic oxidation reaction. The heating rate during oxidation was 2ºC/min to 300ºC with a hold time of 6 to 8 hours. The sample was subsequently reduced in pure hydrogen. The regenerated cobalt catalyst recovered its initial Fischer-Tropsch activity completely. Temperature programmed oxidation (TPO) analyses showed that it was possible to remove a large part of the polymeric carbon with the regeneration process [7]. Furthermore, TEM analyses showed that the large cobalt crystallites of the spent cobalt catalyst underwent re-dispersion following regeneration. Reversing deactivation mechanisms like sintering contributed to the recovery of the activity of a deactivated cobalt catalyst. It is important to understand the mechanism of re-dispersion and the influence of re-dispersion on activity.

2.5.1 Cobalt re-dispersion

A supported-cobalt (Co) catalyst with high turnover rates requires a supported catalyst with small metal crystallites with a high surface density on the support surface [24]. It is thus important to regain a well dispersed supported-cobalt catalyst with small crystallites after regeneration of a sintered catalyst. This can only be achieved by re-dispersion of cobalt during the regeneration process.

Re-dispersion may occur during oxidation if a volatile or highly mobile metal oxide is formed that migrates and interact strongly with the support [71]. Re-dispersion may occur during reduction, due to particles break-up into small clusters [71], if crystallite contraction is observed. Re-dispersion is influenced by temperature, time, atmosphere and support. It is also influenced by the metal and promoter used as well as metal loading and catalyst preparation.

The crystallite splitting model has been used to describe the re-dispersion of platinum particles during oxidation [13,60]. Platinum oxide is formed on the support during oxidation. The bulk platinum oxide is thermodynamically unstable and single molecules of platinum oxide are formed on the support. The decrease in particle size is due to cracks that are formed on the surface of the crystallite resulting eventually in fracturing. The entire particle must be converted to the oxide before splitting can occur. Therefore this is only applicable on small particles. A re-dispersed platinum metal on the support is formed after reduction.

The oxidation step plays an important role during regeneration of the catalyst (oxidative thermal treatment is used to remove carbon from the spent catalyst during regeneration [70]) and therefore the oxidation of the cobalt catalyst is of interest with particular emphasis on the morphological changes of cobalt [72].

It was shown with cobalt particles supported on amorphous SiO_2 films that formation of the Co_3O_4 phase prior to reduction at 500°C is important in the formation of small cobalt particles [73]. It was observed that the cobalt-containing phase spreads over the surface during calcination in contrast to the sample that was only annealed at 300°C under vacuum. The annealed sample formed a quasi-continuous structure where particles with an irregular shape were formed during reduction. CoO was formed at 425°C when the oxidised sample was reduced and further reduction at 500°C caused the film to break into small isolated particles.

A model catalyst where cobalt particles were supported on amorphous thin carbon films was used to investigate microstructure changes during oxidation-reduction treatment [72]. It was found that oxidation-reduction treatment influences metal dispersion. A reduced sample was heated in air at 400°C and kept for 2 hours. It was found that the hollow quasi-continuous structures consisted crystalline domains occurring at the edges. Subsequent heating of the sample in H_2 at 300°C for 2 hours, resulted in rupture of the crystalline particles and their contraction. Further heating of the sample in H_2 at 400°C for 2 hours resulted in sintering of the metal particles.

Recent research work shows that a hollow sphere structure is formed during oxidation of cobalt metal [74,75] as a consequence of the Kirkendall effect. This effect occurs when the mutual diffusion rates of two components differ and the outward diffusion of cobalt is faster than the inward diffusion of oxygen. The formation of hollow spheres was shown by oxidation of cobalt nano-crystals [74] and cobalt supported on Montmorillonite [75]. In the latter case, it was observed that cobalt oxide crystallites were irregular with cracks. Further reduction of the cobalt oxide leads re-dispersion of the cobalt by breaking into smaller pieces [75].

The formation of hollow spheres or void spaces is not unique to the oxidation of cobalt, but has been observed with copper [76], iron [77], aluminium [76,78] and zinc [79], However, the oxidation of lead does not lead to the formation of hollow spheres [76].

The Kirkendall effect is the dominant process for formation of hollow spheres from Cu nano-particles during oxidation due to the faster diffusion of copper in comparison to oxygen [76]. The faster diffusion of metal ions from the core metal to the outer oxide shell produces excess vacancies at the metal side near the metal/oxide interface. Vacancy clusters begin to form at the interface and become larger as the metal atoms in the core migrate into the oxide layer and then contribute to the formation of a new oxide layer. After all the metal ions are consumed by the reaction with the oxygen ions absorbed on the oxide surface, a nano-pore is formed as a result of vacancy clustering in the core of the oxide particle.

Void formation was observed with iron nano particles oxidised at room temperature [77]. Particles smaller than 8 nm were fully oxidised with a void enclosed in the centre of the particle. Iron particles larger than 8 nm had a surface oxide layer of ~3 nm. Voids were observed on the interface between the oxide layer and metal core.

The formation of hollow aluminium particles was also observed upon oxidation of aluminium particles at temperatures higher than 1000^{o}C using high resolution transmission electron microscopy (HRTEM) [78] and supported by density measurements. This was confirmed by Nakamura et al. [76], who reported the formation of hollow spheres upon oxidation of small Al nanoparticles (6-8 nm).

However, oxidation of larger Al particles (10-20 nm) only yielded an oxide layer on the outer surface that stayed constant even after a long period of oxidation. The formation of hollow Al-oxide through the oxidation of small Al nano-particles can be explained in terms of the Cabrera-Mott theory where there is an initial rapid outward diffusion of metal cations during the initial oxidation stage. Subsequently, oxygen atoms are absorbed on the oxide surface establishing an equilibrium between the metal and absorbed oxygen. It is further assumed that electrons can pass through this oxide layer rapidly. This process creates an electronic field over the thin oxide layer capable of pulling metal ions through the oxide film. However, after the formation of an initial oxide layer of a certain thickness, the migration of metal ions requires thermal activation for further growth of the oxide layer.

The oxidation of zinc follows a similar pattern as aluminium. TEM studies showed hollow sphere formation during low temperature oxidation of zinc (Zn) nano particles, but not with particles larger than 20 nm [79]. The authors found that oxidation rate was initially very rapid and the dropped gradually to very low levels. Therefore the larger Zn nano particles did not show the formation of hollow spheres since the rate of oxidation slows down after the formation of ZnO (zinc oxide) layer of 10 nm.

CHAPTER 3

EXPERIMENTAL

3.1 Preparation of model catalyst samples

Supported cobalt catalysts were prepared with Ceralox APA-0.5 alumina as a support. The support, an aluminium oxide (α-Al_2O_3), lot number C816982 with a surface area of 8.1 m^2/g, pore volume of 0.0023 cm^3/g, was obtained from Sasol North America, Inc. The particle size according to the sieve analysis was 33 mass % above 200 µm and 7 mass % smaller than 75 µm. The main batch of catalyst was prepared by impregnation of the support with cobalt nitrate solution (*Experiment 1*). This batch was used to produce other catalysts in either a reduced or oxidised state. The aim was to see the influence of OROR (O = oxidation and R = reduction) treatment on the re-dispersion of the cobalt on the support. One sample was oxidised at 10 bar to compare high pressure oxidation with oxidation at atmospheric pressure (0.86 bar). All these procedures are discussed below. The prepared catalysts are listed below in Table 3.1.

The Ceralox APA-0.5 alumina support was treated in a similar manner as the catalyst used for characterisation of the support to obtain information on the influence of catalyst preparation and treatment on the support (see Table 3.2).

Table 3.1: *List of catalyst samples prepared*

Sample name	Sample info	Sequence of treatment[1]
Exp 1	Main batch	O
Exp 2	Prepared from Exp 1	OR
Exp 3	Prepared from Exp 2	ORO
Exp 4	Prepared from Exp 3	OROR
Exp 5	Prepared from Exp 2	OR HP_O

[1] O: treatment in oxygen; R: reduction in hydrogen; HP_O: high pressure oxidation

Table 3.2: *List of support samples prepared*

Sample name	Sample info	Sequence of treatment[1]
S1	Main batch	O
S2	Prepared from S1	OR
S4	Prepared from S2	ORR

[1] O: treatment in oxygen; R: treatment in hydrogen/water

3.1.1 Impregnation of support with cobalt nitrate

10 g of cobalt was loaded on 90 g of Ceralox APA-0.5 alumina support. Two crucibles, each containing 55 g of support were dried overnight at 120°C in air. 49.39 g of cobalt nitrate (corresponding to 0.17 mol) was weighed off and dissolved in 60 ml of deionised water. The pH of the solution was 5.95. The support (90 g) was weighed off and added to the solution. The slurry was dried on a rotavap immersed in an oil bath heated to 75°C. The rotational speed was 90 rpm. The absolute pressure was set at 260 mbar. After 1½ hours at 75 °C, the temperature of the oil bath was increased to 80°C. After 2½ hours at 80°C, the temperature was increased to 85°C. After 1 hour at 85°C and 260 mbar, the pressure was reduced to 50 mbar, and these conditions were maintained for another hour. Subsequently, the paste was removed from the round bottle flask by scraping it out of the flask. The paste dried very easily and became very hard when it was exposed to air.

3.1.2 Support "impregnation" with water

90 g of Ceralox APA-0.5 alumina support was added to 60 ml of deionised water in order to mimic the impregnation procedure. The pH of the solution was 5.38 (the lowering of the pH can be ascribed to the release of protons from the support surface or dissolution of some of the support). The slurry was dried on a rotavap immersed in an oil bath heated to 75°C. The rotational speed was 90 rpm. The absolute pressure was set at 260 mbar. After 1½ hours at 75 °C, the temperature of the oil bath was increased to 80°C. After 2½ hours at 80°C, the temperature was increased to 85°C. After 1 hour at 85°C and 260 mbar, the pressure was reduced to 50 mbar, at which conditions it was kept for another hour.

3.1.3 Calcination and oxidation step (*Experiment 1*, *Experiment 3* and *S1 support*)

Calcination was performed in air by fluidising the sample in a glass tube. The glass tube consisted of an outer tube (65 mm X 260 mm) with an inner tube (38 mm X 215 mm) with a frit at the bottom. The sample was crushed with a mortar and pestle and subsequently loaded into the inner tube. The (initial) particle size distribution used was 7.8 mass % above 200 μm and 8.6 mass % smaller than 75 μm. The sample was heated to 250°C at 1°C/min where it was kept for 6 hours. The temperature of the oven was set at 255°C to be able to reach a temperature of 250°C inside the sample. The flow rate of air was controlled with a Brooks mass flow controller. The space velocity was 1430 ml (STP)/hr/$g_{catalyst}$ (in *Experiment 1* the catalyst mass was

100 g and a flow rate of 2380 ml (STP)/min was used; in *Experiment 3* the catalyst mass was 12 g and a flow rate of 286 ml (STP)/min was used). The measured flow rate and the temperature within the catalyst bed temperature in the calcination set-up were continuously monitored (see Figures 3.1 and 3.2).

A bed temperature of 250°C was not reached during the calcination of *Experiment 1*. Two different calcination units were used, i.e. unit 4 for *Experiment 1* and unit 5 for *Experiment 3*. The differences in bed temperature are due to the differences in catalyst loading of 100g and 12 g. This is illustrated in Figure 3.3 where the same calcination unit was used with different loadings of support. The support was calcined using the same procedure used to calcine the catalyst. The sample was heated to 250°C at 1°C/min where it was kept for 6 hours. The temperature of the oven was set at 255°C to be able to reach a temperature of 250°C inside the sample. The space velocity was 1430 ml (STP)/hr/$g_{catalyst}$.

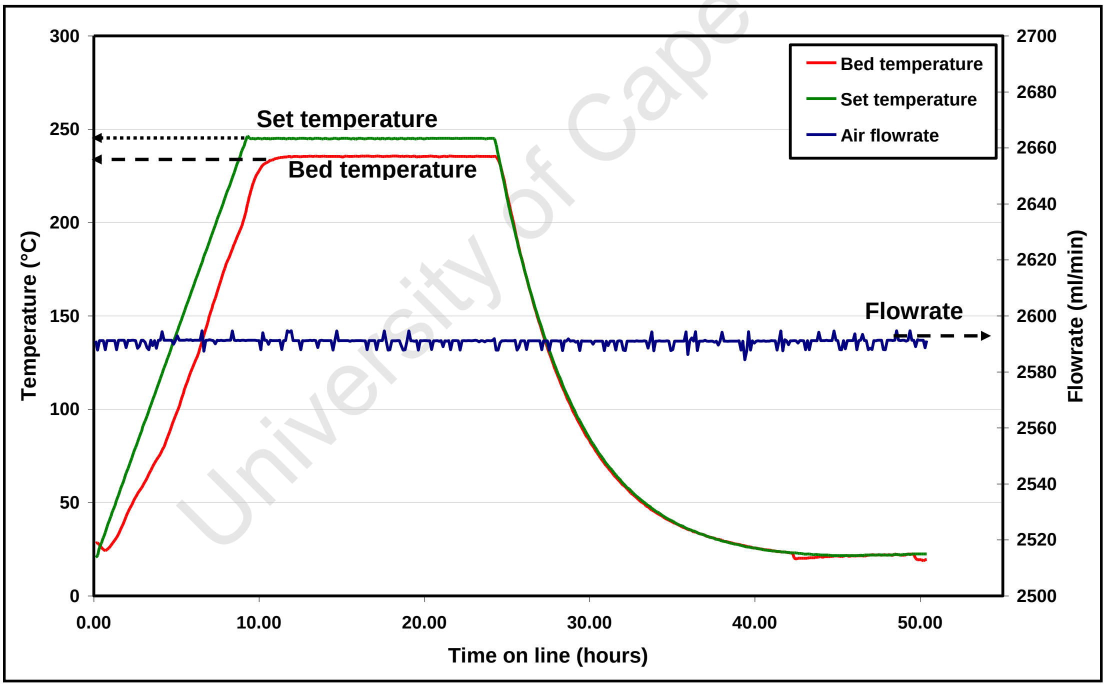

Figure 3.1: *Flow rate and temperature measured during calcination in air of 100 g of catalyst with a space velocity of 1430 ml (STP)/hr/$g_{catalyst}$ (Exp 1)*

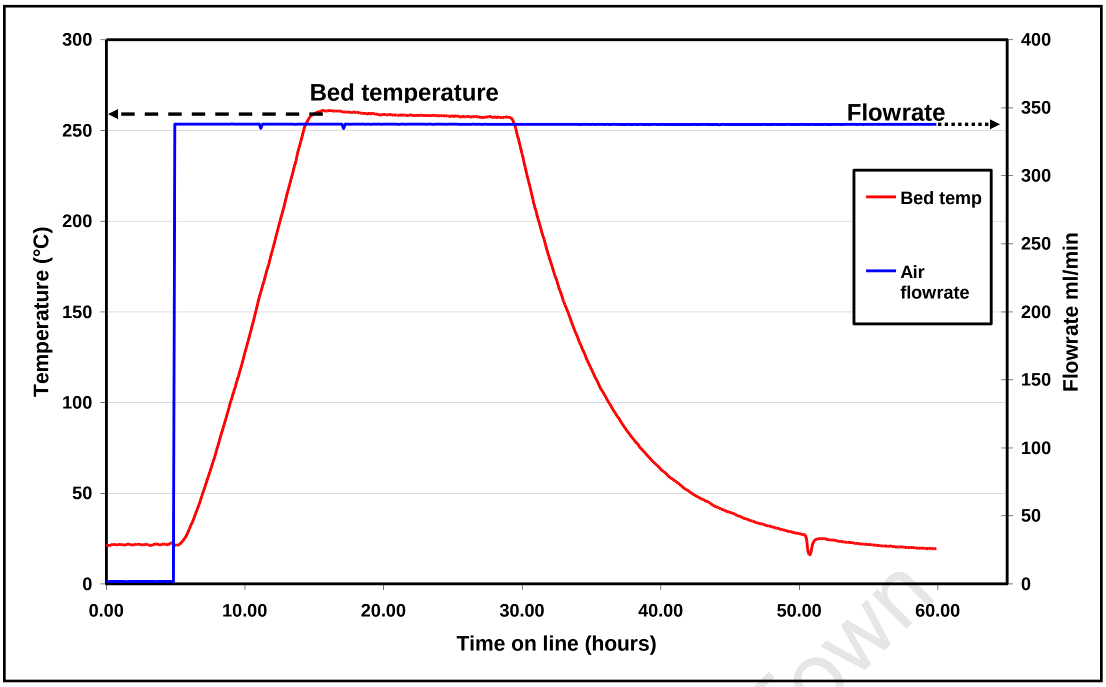

Figure 3.2: *Flow rate and temperature measured during calcination in air of 12 g of catalyst with a space velocity of 1430 ml (STP)/hr/g$_{catalyst}$ (Exp 3)*

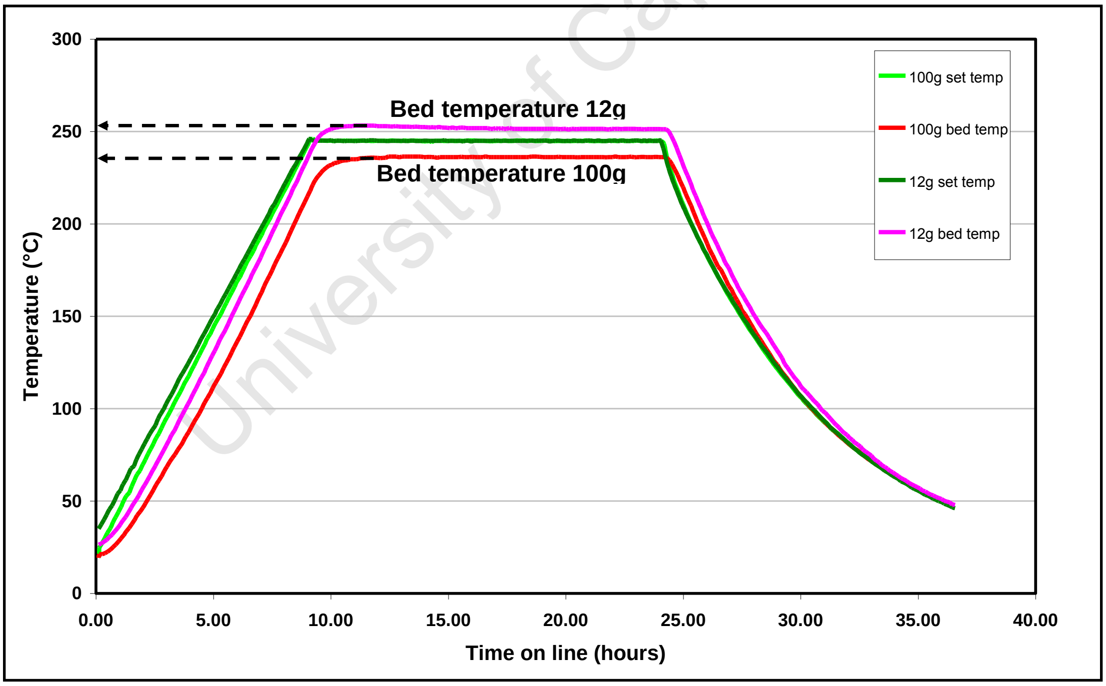

Figure 3.3: *Flow rate and temperature measured during calcination in air of 12 g and 100 g of support with a space velocity of 1430 ml (STP)/hr/g$_{catalyst}$*

3.1.4 Reduction (*Experiment 2*, *Experiment 4*, *S2 support* and *S4 support*)

The sample was reduced in pure hydrogen by fluidising the sample in a glass tube. The glass tube consisted of an outer tube (28 mm X 245 mm) with an inner tube (18 mm X 235 mm). Glass wool was put at the bottom of the tube to maitain the sample in the tube. The sample was loaded and another piece of glass wool was inserted. This was put a small distance above the catalyst bed to enable fluidisation of the catalyst bed. The glass wool was added at the top to prevent small particles being carried out of the reactor tube with the gas flow. The sample was heated to 425°C at 1°C/min where it was kept for 10 hours. The space velocity was 2000 ml (STP)/hr/$g_{catalyst}$. The hydrogen flow was controlled with a Brooks mass flow controller. Figures 3.4 and 3.5 show the measured flow rates and inside temperatures for *Experiment 2* and *Experiment 4* respectively. In *Experiment 2* a catalyst mass of 15 g was used and in *Experiment 4* the catalyst mass was 6 g, used. Different flow rates were used since the space velocity was kept constant at 2000 ml (STP)/hr/$g_{catalyst}$. The sample was after cooling unloaded in dry ice. A 250 ml plastic bottle was half way filled with dry ice. Argon at a low flow rate was used to replace the air inside the bottle filled with the dry ice. The sample was gently added to the dry ice. The sample was left under argon until all the dry ice had evaporated.

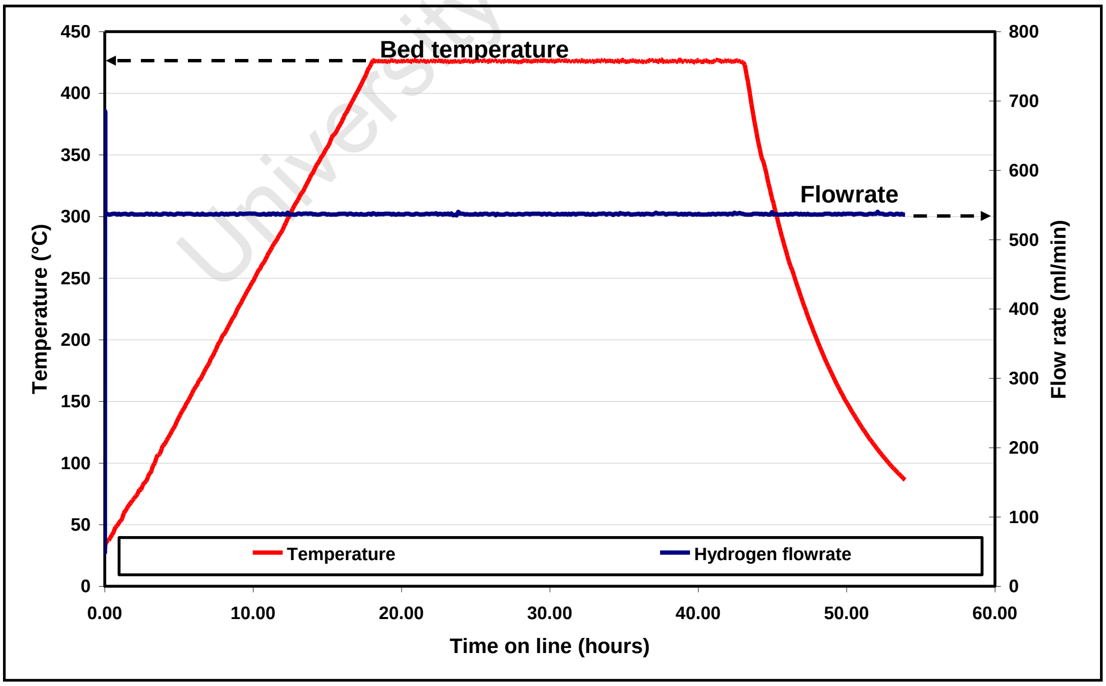

Figure 3.4: *Flow rate and temperature measured during reduction in hydrogen of 15 g of catalyst with a space velocity of 2000 ml (STP)/hr/$g_{catalyst}$ (Exp 2)*

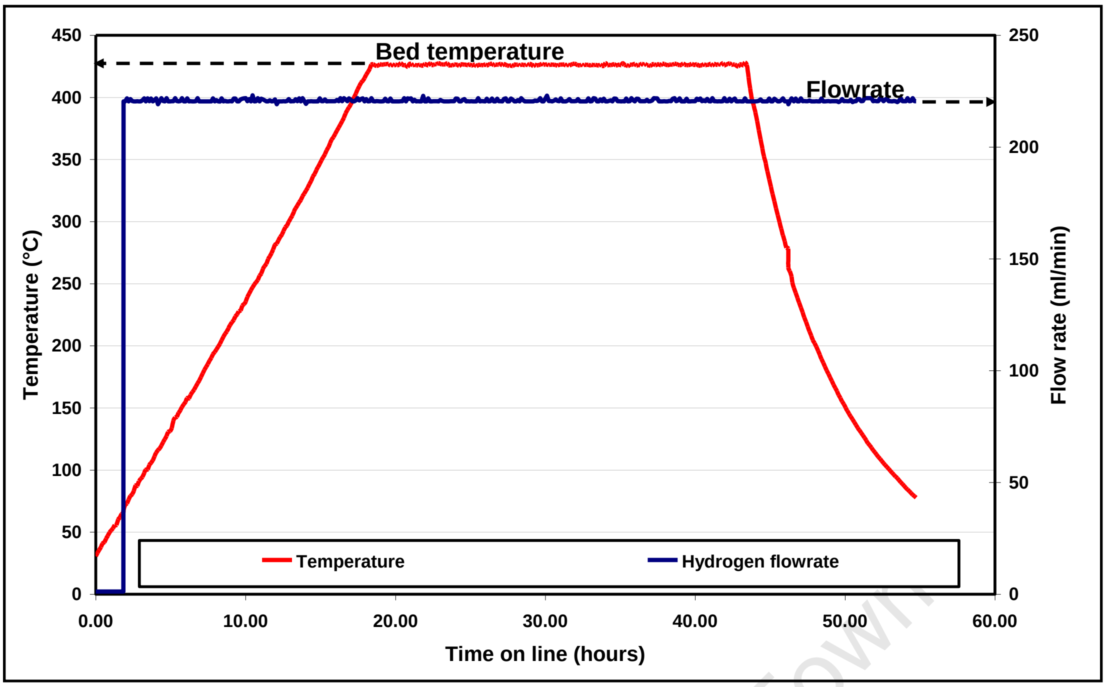

Figure 3.5: *Flow rate and temperature measured during calcination in air of 6 g of catalyst with a space velocity of 2000 ml (STP)/hr/$g_{catalyst}$ (Exp 4)*

The support also underwent a hydrogen treatment after calcination to prepare the support for TEM analyses. 5 g of support was loaded in a glass tube. The support was heated at 10°C/min to 425°C. When the temperature reached 400°C, hydrogen gas was switched to bubble through a Schott bottle containing 300 ml of deionised water. Water vapour was added to the hydrogen stream to mimic the gas composition during the reduction process of the supported catalyst (p_{H_2O} = 2.7 kPa). The temperature was kept at 425°C for 6 hours. The reactor was subsequently cooled down under dry hydrogen to prevent condensation of water on the sample. Hydrogen (100 ml/min at ambient conditions) was fed from the bottom of the glass tube. A low flow rate was used to prevent excessive bubbling of the water and condensation of water in the lines.

3.1.5 High pressure oxidation

Sample from *Experiment 2* (5 g) was loaded into a fluidized bed unit. Synthetic air was fed from the bottom of the reactor. A frit was installed at the bottom of the reactor to prevent the catalyst from falling through. In the top part of the reactor glass wool was placed to prevent small particles from passing through. The diameter of the reactor 21.7 mm was and the length was 280 mm. The sample was heated to 250°C at 1°C/min where it was kept for 6 hours. The temperature of the heating mantle was set at 255°C in order to achieve a temperature of 250°C inside the sample. The space velocity was 1560 ml/hr/$g_{catalyst}$. The flow rate of air was controlled with a Brooks mass flow controller. A backpressure regulator was used to control the pressure inside the reactor. The pressure was controlled at 10 bar (gauge pressure). The oxygen content in the effluent was determined by diverting a flow of 100 ml/min (at ambient conditions) to an oxygen analyzer (Servomex 5200 Multi Purpose). The rest of the gas was vented. The oxygen analyzer was calibrated with air and argon.

A schematic drawing of the fluidized bed unit is given in Figure 3.6. Three thermocouples were used to measure the temperature inside the reactor. They were placed at the following distance from the bottom of the reactor:

Thermocouple 1	bottom of the reactor
Thermocouple 2	4 cm from bottom of reactor
Thermocouple 3	7 cm from bottom of reactor

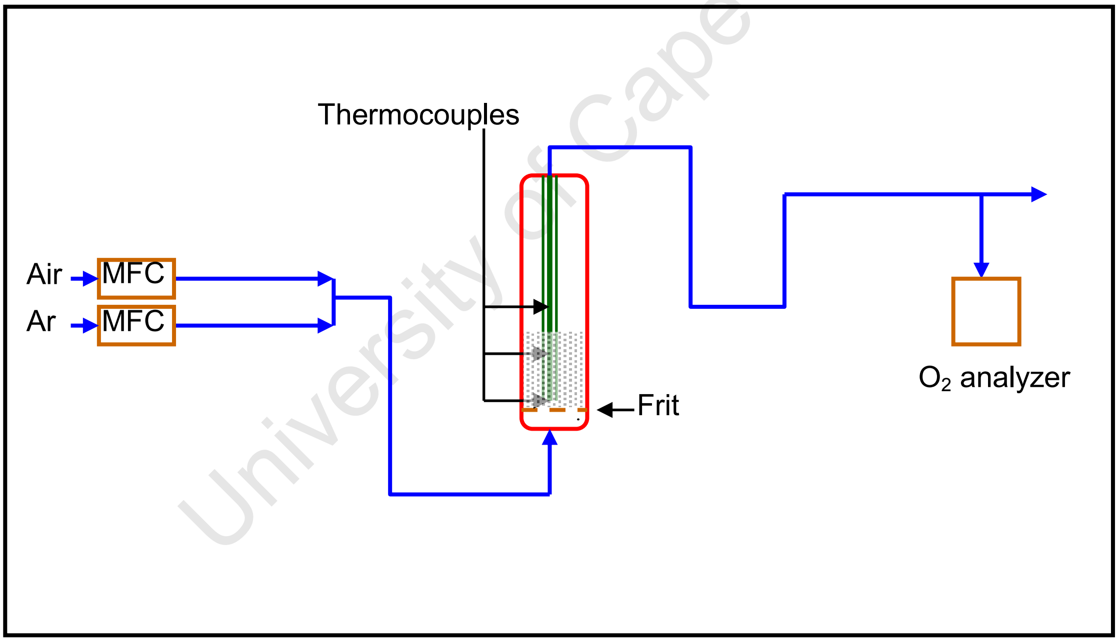

Figure 3.6: *Schematic drawing of the fluidized bed unit used for high pressure oxidation*

The Figure 3.7 below shows the temperatures as measured inside the reactor. Thermocouple 1 and thermocouple 2 measured the temperature in the catalyst bed. The incoming gas was not heated and therefore the temperature indicated by thermocouple 1 at the bottom of the reactor is slightly lower than the temperature indicated by thermocouple 2. Thermocouple 3 was positioned above the catalyst bed and a much lower temperature was indicated in the top part of the reactor. This indicates heat loss in the upper part of the fluidized bed reactor.

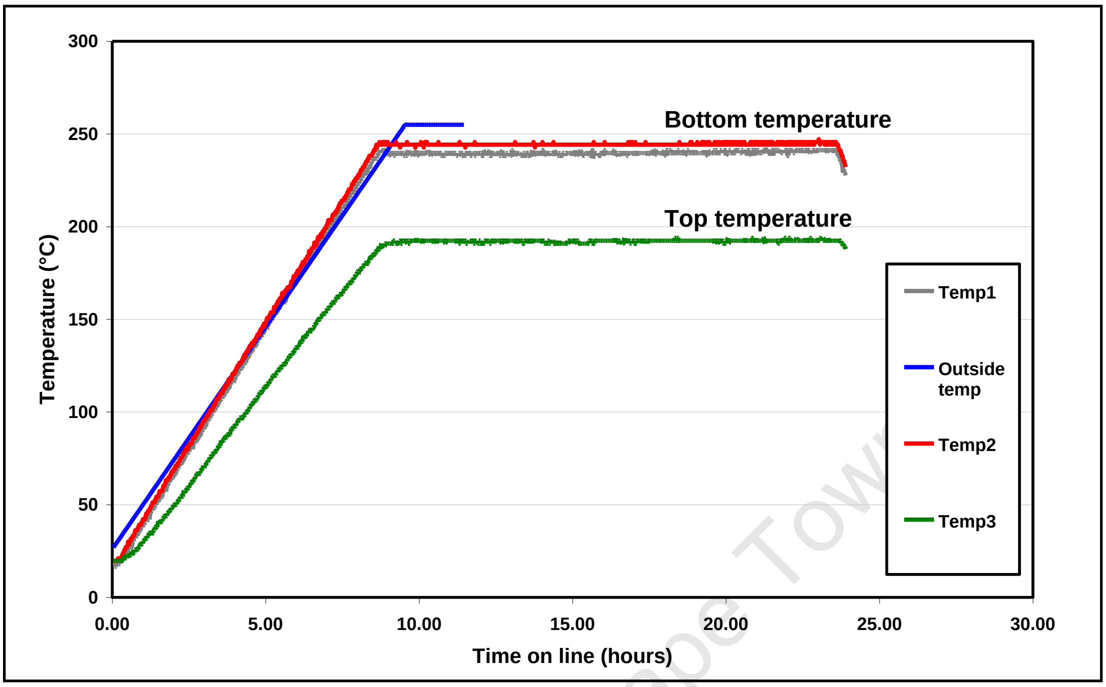

Figure 3.7: *Temperatures measured during the high-pressure calcination in Exp 5 (the royal blue line is set temperature of the heating element and not a measured value).*

3.2 Catalyst characterization

Characterization techniques used were inductively coupled plasma optical emission spectroscopy (ICP-OES), X-ray diffraction (XRD), *in-situ* XRD, H_2 chemisorption, temperature programmed reduction (TPR) and transmission electron microscopy (TEM). ICP-OES was used to determine the metal loading on the prepared catalyst. Crystallite size determination was done with XRD. *In-situ* XRD was used to determine crystallite sizes and phase changes during consecutive reduction and oxidation steps. TEM analyses were performed to support XRD analyses and to obtain physical images of the changes in crystallite sizes. Metallic surface area and % dispersion were estimated from static H_2 chemisorption. The reducibility of the various calcined samples was evaluated using TPR.

3.2.1 Inductively coupled plasma optical emission spectroscopy

Inductively coupled plasma optical emission spectroscopy (ICP-OES) is an analytical technique used for the detection of trace metals. It is a type of emission spectroscopy that uses the inductively coupled plasma to produce excited atoms and ions that emit electromagnetic radiation at wavelengths characteristic of a particular element. The intensity of this emission is indicative of the concentration of the element within the sample.

The ICP-OES consists of two parts: the ICP and the optical spectrometer. The ICP torch consists of 3 concentric quartz glass tubes. The output or "work" coil of the radio frequency (RF) generator surrounds part of this quartz torch. Argon gas is typically used to create the plasma.

The sample is digested in a Milestone Etos Plus closed vessel microwave using hydrochloric (HCl), nitric (HNO_3) and hydrofluoric acid (HF) (Merck GR grade). A sample (0.1 g) was weighed off into a Teflon microwave digestion vessel. In the process 6 ml of concentrated HCl, 2 ml concentrated HNO_3 and 1 ml concentrated HF was added to the sample. After digestion the sample was diluted to 100 ml with deionised water. The cobalt in the diluted solution was quantified by comparing the intensity at the characteristic wavelength of a standard using a Perkin-Elmer Optima 4300 DV. The cobalt loading of the sample was calculated from:

$$\text{Co (ppm m/m)} = \frac{\text{Concentration from calibration (µg/ml) X volume (100 ml)}}{\text{sample mass (g)}}$$

The accuracy of this method depends heavily on the initial mass of the catalyst sample, in addition to accurate calibration and dilution of the digested sample. The mass of the catalyst sample may change with time due to changes in the catalyst, e.g. due to uptake of moisture from air.

3.2.2 X-ray diffraction (XRD)

X-rays have wavelengths in the Ångstrøm range. X-rays are sufficiently energetic to penetrate solids and to probe their internal structure. X-ray diffraction (XRD) is the elastic scattering of X-ray photons by atoms in a periodic lattice. The scattered monochromatic X-rays that in are in phase produce constructive interference. Lattice spacing can be calculated with Bragg’s law from the X-ray diffraction of crystal planes. The angles of the maximum intensity enable one to calculate the spacing between the lattice planes, which aids in the phase determination. The lattice spacing, which is characteristic for a particular structure, can be obtained from the measured diffraction angle, 2θ, using the Bragg relationship. Only a small fraction of powdered samples will be orientated that a certain crystal plane is at the correct angle θ with the incident beam for constructive interference (see Figure 3.8) [80].

In catalyst characterisation, the diffraction patterns are mainly used for phase identification. XRD can also be used to monitor the kinetics of bulk transformation and to estimate particle size. Diffraction patterns of perfect crystals are very narrow, but line broadening occurs with crystallite sizes below 100 nm. Line broadening occurs due to incomplete destructive interference in scattering directions where the X-ray is out-of-phase [81].

The Debye-Scherrer equation relates crystallite size to line width [81]:

$$\langle L \rangle = \frac{K \cdot \lambda}{\beta \cdot \cos \theta}$$

where

<L> a measure for the volume average dimension of the particle in the direction of perpendicular to the reflecting plane

λ X-ray wavelength

β peak width

θ the angle between the beam and the normal on the reflecting plane

K a constant

The Debye-Scherrer equation indicates that sharper peaks are obtained when using X-rays with smaller wavelengths (λ) and at lower diffraction angles.

Better procedures to determine particle sizes form XRD are based on line profile analyses with Fourier transform methods. The average size is obtained from the first derivative of the cosine coefficients and the distribution of crystallite sizes from the second derivative.

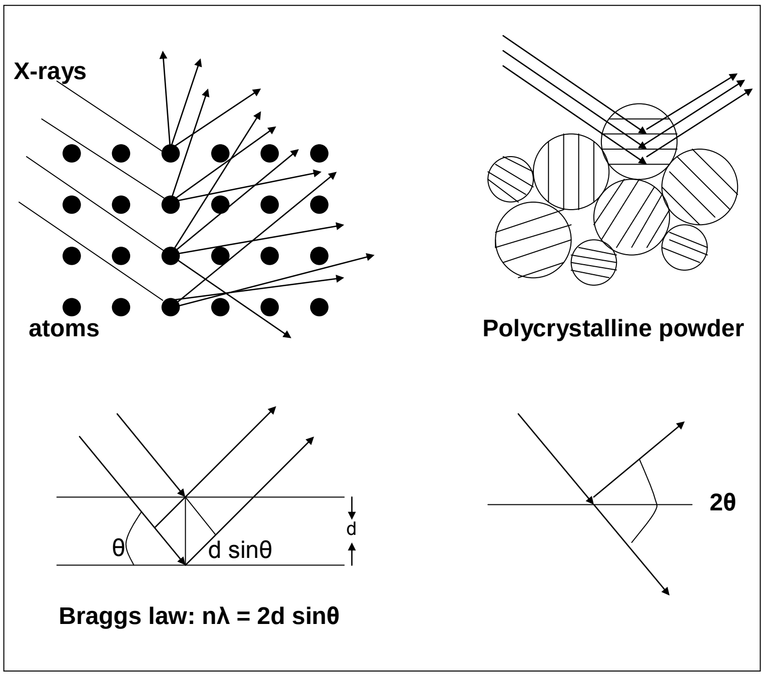

Figure 3.8: *Illustrations of X-ray diffraction [81]*

In the mid neneteen sixties, it was realised that more information could be obtained from a powder pattern, if computers are applied to full-pattern analysis. Rietveld worked out the first computer-based analytical procedure by making use of the full information content of the powder pattern [82]. The Rietveld method uses a least squares approach to refine a theoretical line profile until it matches the measured profile. The "pattern decomposition" procedure is a systematic procedure for decomposing a powder pattern in its component Bragg's reflections without a reference to crystal structure model [81].

The phases and average crystallite sizes of the crystalline phases were determined using powder X-ray diffraction data. The samples were packed into stainless steel holders. The Philips X'Pert Pro multi-purpose diffractometer (XRD-2 system) was used to do the analyses. The instrument settings are given in Table 3.3.

X'Pert HighScore Plus software was used to identify the crystalline phases present in the samples. Topas4 was used for phase analysis using the fundamental parameter approach [83]. The full pattern refinement technique was used to determine the average crystallite sizes.

Table 3.3: *Instrument settings for XRD-analysis on Philips X'Pert Pro multi-purpose diffractometer*

Tube voltage : 40 kV
Tube current : 40 mA
Source : Cobalt (λ: 1.78897 Å)
Soller slit : 0.04 rad.
Beam mask : 10 mm
Fixed divergence slit : 1 °
Anti-scatter slit : 2 °
Filter : Iron
Detector : X'Celerator
Detector active length : 2.121 °
Scan from : 5° (2θ)
Scan to : 105° (2θ)
Step size : 0.0167° (2θ)
Time per step : 149 seconds
Scan duration : 2 hours

3.2.2.1 *In-situ* X-ray diffraction (*in-situ* XRD)

Experiment 1 was performed using *in-situ* XRD. The catalyst (2 g) was packed into a stainless steel holder. The Philips X'Pert Pro multi-purpose diffractometer (XRD-2 system) was used for the analyses. The sample was treated with hydrogen and oxygen in consecutive steps that were repeated. The first cycle was a reduction step (R). The reduction was done with 99.9999% H_2 (Ultra High Purity) with a flow rate of 100 ml(STP)/min. The sample was heated at 5°C/min to a maximum temperature of 425°C. It was held at 425°C for 2 hours. The sample was cooled down to room temperature under helium with a flow rate of 100 ml (STP)/min. The second step was an oxidation step. A mixture of 5 vol% O_2/He was introduced at room temperature with a flow rate of 100 ml(STP)/min. The sample was heated at 3°C/min to 300°C. The sample was cooled down to room temperature and then flushed for 1 hour with He with a flow rate of 100 ml (STP)/min. The two cycles were repeated to give the sequence RORO.

These RORO experiments were analysed by X'Pert HighScore Plus software to identify the crystalline phases present in the samples. Topas4 was used for phase analysis using the fundamental parameter approach [83]. This approach is different from the analytical approach, since it integrates the instrumental parameters with experimental parameters. The true instrument contribution to each peak from the known instrument geometry is calculated.

The full pattern refinement technique was used to determine the average crystallite sizes. Full pattern analyses are predicated on the fact that the diffraction pattern is the sum total of all effects, i.e. the instrument and sample. A computer model is used to obtain the best fit for the experimental data [84]. The Rietveld method uses a least squares approach to refine a theoretical line profile until it matches the measured profile. The “pattern decomposition” procedure is a systematic procedure for decomposing a powder pattern in its component Bragg’s reflections without a reference to crystal structure model [84].

3.2.3 X-ray photoelectron spectroscopy (XPS)

XPS analyses were performed with the oxidised catalyst samples (*Experiment 1*, *Experiment 3*, and *Experiment 5*) to give insight on the surface properties of the calcined catalysts, specific on the oxidation state of the cobalt oxides. The XPS measurements were carried out using a Kratos AXIS Ultra spectrometer, equipped with a monochromatic X-ray source and a delay-line detector (DLD). Spectra were obtained using the aluminium anode (Al Kα = 1486.6 eV) operating at 150W. Survey scans were measured at a constant pass energy of 160 eV and region scans at 40 eV. The background pressure was 2 x 10^{-9} mbar.

3.2.4 Transmission electron microscopy (TEM)

Transmitted and diffracted electrons are used in transmission electron microscopy (TEM). The instrument is similar to an optical microscope where the optical lenses are replaced with electromagnetic lenses. In TEM analyses, a primary electron beam of high energy and high intensity is passed through a condenser to produce parallel rays. These rays are impinged on the sample. The transmitted electrons from a two dimensional sample, are magnified by the electron optics to produce a bright-field image [80].

A small amount of catalyst powder was mixed with ethanol. The catalyst/ethanol mixture was transferred drop-wise by pipette onto holey carbon film Cu grids. A JEOL 2010 with a LaB_6 filament as electron source was used for this analysis (CSIR Nanotechnology Centre; Pretoria). This instrument was operated at 200kV. Digital TEM images are obtained on a Gatan camera.

3.2.5 Hydrogen (H_2) chemisorption

Chemisorption is a much stronger interaction than physical adsorption. During the chemisorption process of hydrogen, the adsorbing gas (H_2) splits into atomic H chemically bonded to the adsorption site. This interaction involves the sharing of electrons between the adsorbate and the solid surface and may be regarded as the formation of a surface compound. Chemisorption occurs only on certain surfaces or surface sites. It only occurs when if the adsorptive (H_2) makes direct contact with the surface and therefore only a monolayer can be formed. Chemisorption unlike physical adsorption is difficult to reverse by vacuum and depends on the strength of adsorption. From chemisorption isotherms quantities such as metal dispersion, surface area and active particle size can be derived [85].

The Langmuir equation can be used to describe the adsorption process. It assumes that the surface of a solid contains a fixed number *n* of adsorption sites and only one species at a time can occupy a site. Furthermore, it is assumed that the heat of adsorption of each site is equal and there is no interaction between the adsorbed molecules. At any equilibrated temperature and pressure some fraction θ of the sites are occupied. The Langmuir equations are given below for associative and dissociative adsorption:

Associative chemisorption

$$\theta = \frac{N}{N_S} = \frac{b \cdot P}{1 + b \cdot P}$$

Dissociative chemisorption

$$\theta = \frac{N}{N_S} = \frac{b \cdot P^{0.5}}{1 + b \cdot P^{0.5}}$$

where

θ	fraction of sites that are occupied at equilibrated temperature and pressure
N	number of sites occupied
N_s	total number of accessible adsorption sites
b	adsorption coefficient
P	pressure

The fraction of the total active metal accessible to the reactant molecules N_T is called the dispersion, D. The total amount of active metals added to the support during preparation of the catalyst must be known in order to determine metal dispersion. It is expressed as a percentage:

$$D(\%) = \frac{N_S}{N_{total}} \cdot 100\%$$

The number of sites occupied is typically measured indirectly, viz. via the uptake of the adsorbing gas. Knowing the stoichiometry of the adsorption, the uptake of the adsorbing gas can be related to the number of sites occupied.

$$N = \frac{V_{uptake}}{\underline{V}_{gas}} \cdot F_S \qquad\qquad N_S = \frac{V_{uptake,sat}}{\underline{V}_{gas}} \cdot F_S$$

where

V_{uptake}	volume of active gas chemisorbed (cm^3(STP)/g)
$V_{uptake,sat}$	volume of active gas chemisorbed at saturation (cm^3(STP)/g)
$\underline{V}_{gas}$	molar volume of an ideal gas at STP (22414 cm^3/mol)
F_s	stoichiometric factor for adsorption process

The dispersion can then be calculated from the saturation uptake and the number of moles of active metal present in the sample:

$$D(\%) = \frac{V_{uptake,sat} \cdot M_{metal}}{\frac{w_{metal}(\%)}{100} \cdot \underline{V}_{gas}} \cdot F_S \cdot 100\%$$

where

D	dispersion (%)
$V_{uptake,sat}$	volume of active gas chemisorbed at saturation (cm^3(STP)/g)
$\underline{V}_{gas}$	molar volume of an ideal gas at STP (22414 cm^3/mol)
w_{metal}	weight fraction of the active metal in the sample (%)
M_{metal}	molar mass of active metal in g/mol
F_s	stoichiometric factor for adsorption process

The active metal surface area can now be determined knowing the typical site density of surface metal atoms ($N_{Me,surface}$ – for cobalt: $N_{Co,surface}$ = 14.6 $Co_{surface}/nm^2$). is that portion of the total metal on the surface that is accessible to gases. The active metal area (m^2/g) is calculated as follows:

$$A_m\left(\frac{m^2}{g}\right) = \frac{N_s \cdot N_{Avogadro}}{N_{Co_{surface}} \cdot 10^{18}\left(\frac{nm^2}{m^2}\right)} = \frac{\frac{V_{uptake,sat}}{\underline{V}_{gas}} \cdot F_s \cdot N_{Avogadro}}{N_{Me_{surface}} \cdot 10^{18}\left(\frac{nm^2}{m^2}\right)}$$

$$A_m\left(\frac{m^2}{g}\right) = 1.8402 \cdot V_{uptake,sat}\left(\frac{cm^3}{g}\right) \cdot F_s\left(\frac{mol}{mol}\right)$$

where

A_m	surface area cobalt metal (m^2/g)
$N_{Avogadro}$	Avogadro's number ($6.022 \cdot 10^{23}$ atoms/mol)
$N_{Me_{surface}}$	Number of surface metal atoms per nm^2 (for cobalt $14.6/nm^2$)

The active particle size can also be estimated assuming spherical or hemi-spherical particles. The particle diameter (d_{Co}) can be calculated from the dispersion, since for a spherical crystallite:

$$D(\%) = \frac{N_s}{N_{total}} \cdot 100\% = \frac{\pi \cdot d_{Me}^2 \cdot N_{Me_{surface}}}{\frac{\pi}{6} \cdot d_{Me}^3 \cdot \frac{\rho_{Me} \cdot 10^{-21}\frac{cm^3}{nm^3}}{M_{Me}} \cdot N_{Avogadro}} \cdot 100\%$$

where

d_{Me}	diameter of spherical or hemispherical metal particle (nm)
ρ_{Me}	density of metal (cm^3/g)

Substituting all the values for metallic cobalt ($N_{Co,surface}$ = 14.6 $Co_{surface}/nm^2$; ρ_{Co} = 8.9 g/cm^3; M_{Co} = 58.9332 g/mo) yields:

$$D(\%) = \frac{96.3}{d_{Me}(nm)} \qquad \text{or} \qquad d_{Me}(nm) = \frac{96.3}{D(\%)}$$

The amount of chemisorbed hydrogen was measured using an ASAP 2010 (Micromeritics Corp., USA) instrument. Prior to analysis approximately 0.25 g of sample was degassed at 100ºC until the vacuum reached a constant instrument base pressure below 10 μmHg. The sample was activated by reduction. The sample was heated to 425°C at 2°C/min and kept at this temperature for 420 minutes under a flow of H_2 (H_2 5.0 =99.999%; 100 ml(NTP)/min). These samples were then cooled down in vacuum and static chemisorption was carried out at 100°C using H_2 as an adsorbate with an equilibration interval of 30 s. The H_2-chemisorption method as entered in the instrument is summarised in Table 3.4.

Table 3.4: *Hydrogen chemisorption method used on ASAP instrument*

Task	Task name	Gas	T (ºC)	Rate (ºC/min)	Hold Time min)
1	Flow	H_2	425	2	420
2	Flow	H_2	400	2	30
3	Evacuation	-	400	2	180
4	Evacuation	-	100	2	120
5	Leak Test	-	100	2	-
6	Analysis	H_2	100	2	-

3.2.6 Temperature programme reduction (TPR)

Temperature programmed reduction (TPR) is a method where a reducing gas mixture (H_2 diluted in argon) flows over an oxide sample. The temperature is raised at a constant rate. Hydrogen is consumed when reduction of the metal takes place. The change in thermal conductivity of the mixture gas is detected by TCD and registered as an electrical signal.

Reduction behaviour was determined using temperature programmed reduction (TPR) measurements on a Micromeritics Autochem 2920 (Micromeritics Corp., USA). The sample (mass ≈ 0.15 g) was placed in a quartz glass reactor. Prior to the TPR measurements, samples were dried *in-situ* at 120°C for 10 min in helium (He-flow = 10 ml(STP)/min). The samples were reduced in a 10% H_2/Ar gas mixture with a flow rate of 75 ml(STP)/min. A cold trap before the TCD detector, filled with a mixture of dry ice and liquid nitrogen was used to remove the water formed during the reduction process. TPR analyses were done at a heating rate of 10°C/min.

3.3 Catalyst testing in a fixed bed reactor

3.3.1 Reactor system set-up

Catalysts were tested for Fischer-Tropsch synthesis activity in an AE (Autoclave Engineer) fixed bed reactor system. There are four reactors in a system that is controlled autonomously. Each unit contained the following pieces of equipment:

- Gas feed system
- Reactor in an oven
- On-line GC

A schematic drawing of the fixed bed reactor set-up is shown in Figure 3.9.

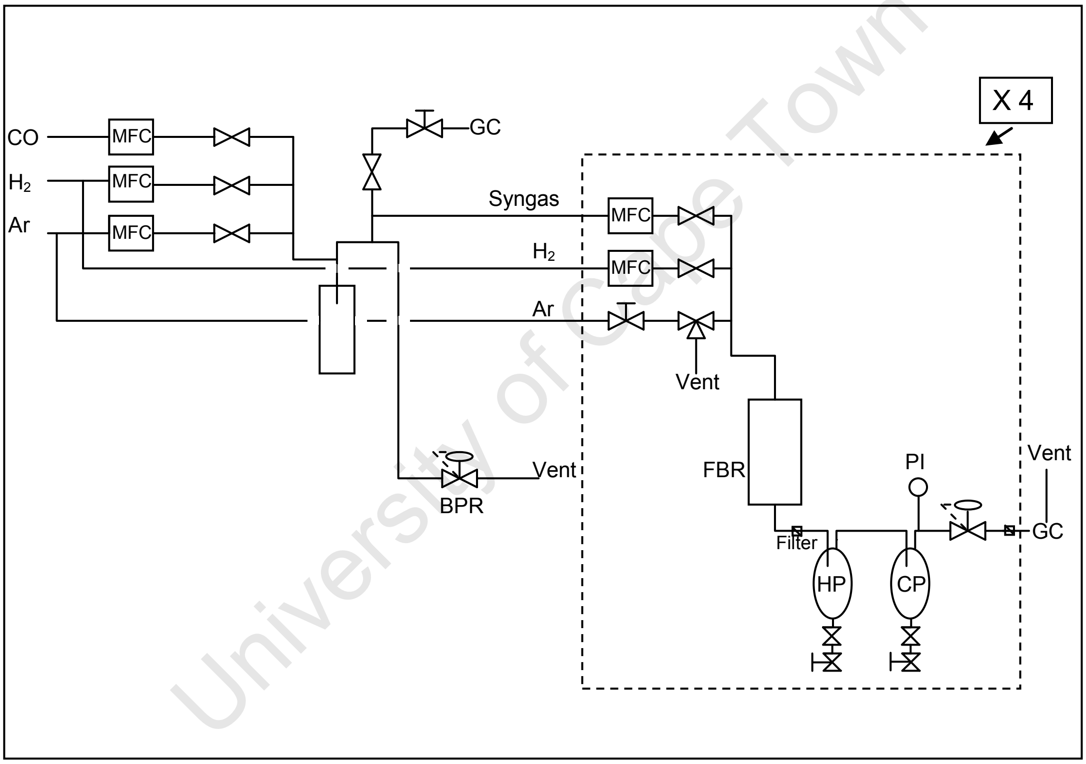

Figure 3.9: *Schematic drawing of fixed bed reactor set-up used for Fischer-Tropsch synthesis*

3.3.1.1 Gas feed system

The gas feed system had been designed such that it was possible to blend the reactors feed gas in one single feed tank. The feed system had its own line that went to a Dani 1000 chromatograph (GC). This allowed the setting of the correct mixture required for the run. This feed was distributed to the three fixed bed reactors, which were used for the testing of the catalysts. The flow from the tank to the reactors was controlled by mass flow controllers (MFC). Each reactor was directly connected to a hydrogen line via a mass flow controller which was used during catalyst reduction.

3.3.1.2 Fixed bed reactor in oven

There were four fixed bed reactors in ovens of which three reactors were used. The reactors had solenoid valves on both the hot and cold knock out pots. These valves could be used to automate the draining of the knock out pots.

The fixed bed reactors made of 316 SS (stainless steal) had a tube length of 400 mm and an internal diameter of 7 mm. The frit is used to prevent blockage and to keep the glass wool position. After the catalyst was loaded, the catalyst bed height was 35 mm. Figure 3.10 shows a photo and a schematic drawing of the fixed bed reactor used in this study. The reactor loaded with catalyst is illustrated in the drawing in Figure 3.10.

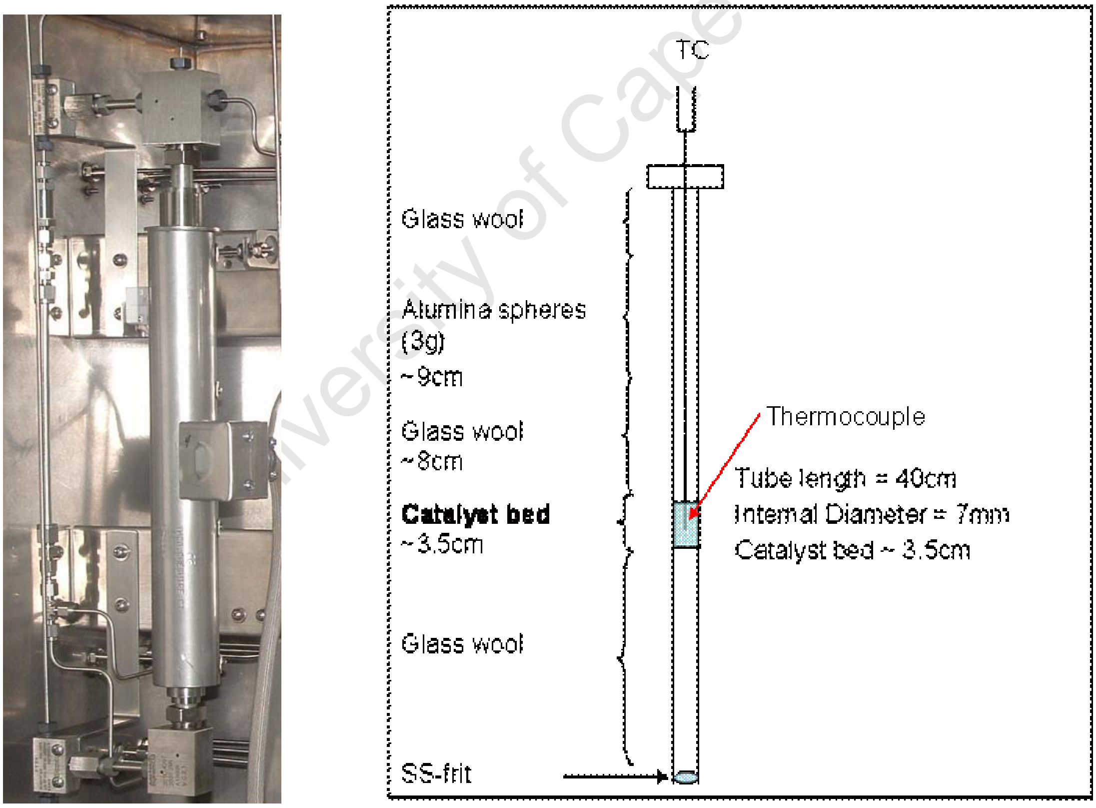

Figure 3.10: *AE fixed bed reactor in an oven (left) and drawing of fixed bed reactor loaded with catalyst (right)*

3.3.1.3 Loading of fixed bed reactor

The fixed bed tube was loaded from the bottom without taking out the thermocouple. The position of the thermocouple was 5 to 10 mm from the top of the catalyst bed.

The reactor is first packed with a glass wool plug, followed by an alumina guard bed (3 g, small spheres of 2 mm in size) followed by another glass wool plug. The catalyst (0.4 g) was mixed with carborundum (2g, 320 gritt) with a spatula in a weighing boat. The catalyst bed (~3.5 – 4cm) is then packed with the middle of the bed at the thermocouple tip. This was followed by a glass wool plug and stainless steel frit. In order to ensure consistent repeatable loading of the catalyst bed always at the thermocouple tip, a 1/8” tubing with markings of the different packing positions was used.

3.3.1.4 Cold pressure testing

The fixed bed reactors were loaded as described. A pressure test was conducted prior the activation of the catalyst under hydrogen. Fischer-Tropsch testing was commenced after reduction was completed.

After loading, the fixed bed reactor was reconnected by fastening the bottom nut and two top two nuts. Two thermocouples (internal thermocouple and thermocouple of the heater element) were placed in position. The pressure test was done by closing the outlets of the 3 cold knock pots. Argon was used to pressurize the 3 reactors to 30 bar. The pressure drop was monitored over the system for about 3 hours. This should not be more than 0.3 bar within the 3 h test.

3.3.1.5 On-line gas chromatograph (GC)

The feed gas and tail gas of each reactor was analysed using a Dani 1000 chromatograph (GC) with thermal conductivity detectors (TCD) to quantify the inorganic components and methane. The GC was equipped with two packed-column injector injectors and two thermal conductivity detectors (TCD) were used to analyze for the inorganic compounds and methane in the gas stream. A valve-system and two packed columns were used per channel. The columns used were Restek Shin Carbon 80/100 µ, Packed 2m x 45.7mm and Restek PPQ Molecular Sieve 5Å, Packed 1m x 45.7mm. Helium with a flow rate of 30 ml/min (actual flow) was used as carrier gas for the one channel which was used to analyze the gas sample for CO, CO_2, CH_4, Ar, and N_2. On the other channel, H_2 was analyzed and Ar with a flow rate of 30 ml/min (actual flow) was used as carrier gas. Table 3.4 summarizes the columns and gas chromatographic conditions used during GC analyses.

The on-line GC-TCD was calibrated using an external standard calibration gas (containing 10.96% CH_4, 37.43% H_2, 2.54% N_2, 12.95% Ar, 25.23% CO and 10.90% CO_2). The chromatogram of the external standard showing CO, CO_2, CH_4, Ar, and N_2 is shown in Figure 3.11.

The Fischer-Tropsch synthesis feed gas and products were sampled in a 24hr period and analysed using a gas chromatograph.

Table 3.5: *Conditions for gas chromatographic analysis using TCD detection*

Channel	**Front**[1]	**Back**[2]
Components detected	CO, CO_2, CH_4, Ar, N_2	H_2
Carrier gas	He	Ar
Flow rate	30	30
T_{oven}, °C	110	110
$t_{analysis}$, min	8	8

[1] Column: Restek Shin Carbon 80/100 µ, packed 2m x 45.7mm
[2] Column: Restek PPQ Molecular Sieve 5Å, packed 1m x45.7mm

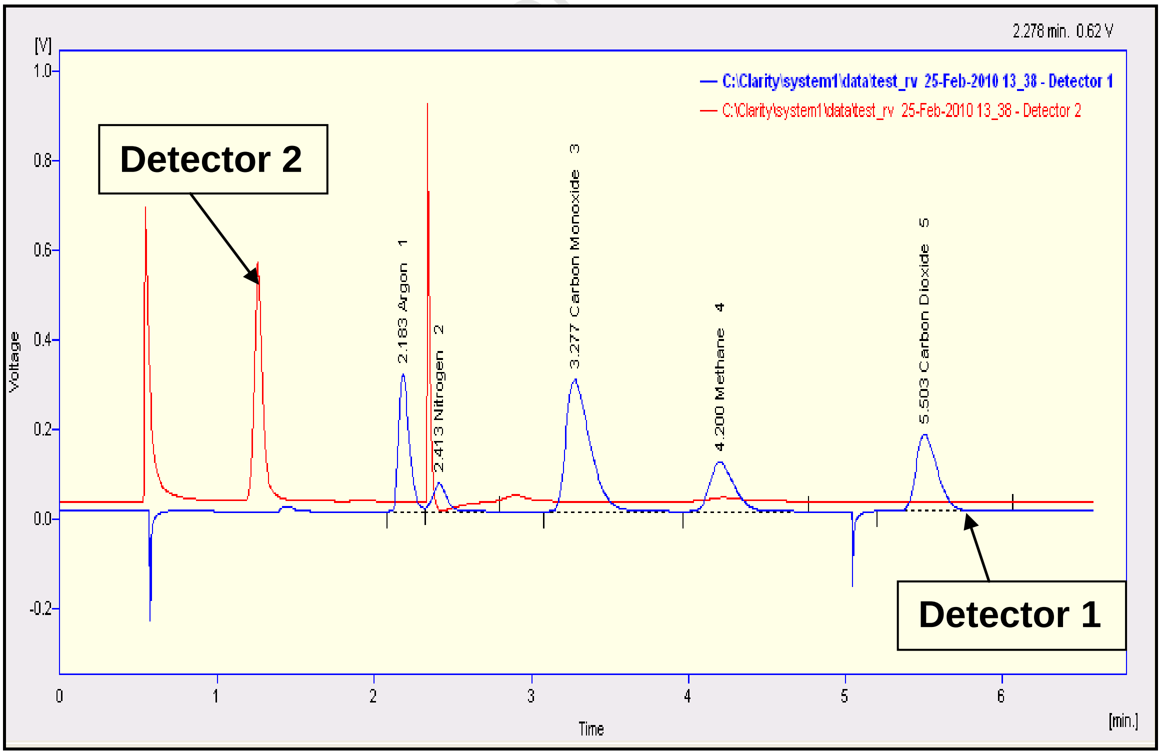

Figure 3.11: *Chromatogram of external standard showing 10.96% CH_4, 37.43% H_2, 2.54% N_2, 12.95% Ar, 25.23% CO and 10.90% CO_2*

3.3.2 Catalyst testing

3.3.2.1 Activation of catalyst

The activation of the catalyst was conducted at atmospheric pressure. The procedure used was similar to the reduction procedure described in section 3.1.4. The samples were reduced in pure hydrogen. The sample was heated to 425°C at 1°C/min where it was kept for 6 hours. The space velocity was 2100 ml (STP)/hr/$g_{catalyst}$. Therefore, the flow rate of H_2 was 14 ml (STP)/min. The reactors were cooled down to 200°C under H_2. The oven temperature is kept at 180°C during reduction and catalysis.

3.3.2.2 Fischer-Tropsch synthesis

After reduction the reactor was pressurized using argon to 15.2 bar. Synthesis gas was added with a MFC at 15.2 bar and 200°C. The flows to the separate reactors were controlled with mass flow controllers. The reaction was started with a GHSV of synthesis gas of 27700 ml(STP) ($CO+H_2$)/hr/$g_{catalyst}$. This was decreased after 24 hours to 9176 ml(STP)/hr/$g_{catalyst}$ to obtain a CO conversion of ca. 10%. The reactor temperature was ramped at 0.5°C/min to 230°C. A H_2/CO ratio of 1.57-1.6 was used with 10 volume % argon.

3.3.3 Data evaluation

The evaluation of the catalysts was done by comparing the activity and the selectivity for methane obtained in the Fischer-Tropsch synthesis over the catalyst samples. Very little heavier products were produced with these catalysts and therefore the focus was only on methane selectivity.

3.3.3.1 Flow rates of compounds from TCD GC analyses

Argon was added as an internal standard to the fresh feed at a known flow rate. This known flow rate of argon was used as a basis for all flow rate calculations. The flow rates of the inorganic compounds (H_2, CO and CO_2) and CH_4 could be calculated using the concentrations (in mole percent) of the compounds obtained in the GC TCD analysis of the feed gas and tail gas [86].

$$F_i = f_i \cdot F_{Ar} \cdot \frac{A_i}{A_{Ar}}$$

Where

f_i	specific response factor for compound *I* relative to the response for Ar (as determined from GC calibration)
F_i	flow rate of compound i
F_{Ar}	flow rate of Argon
A_i	peak area of compound *i* in GC-trace of TCD
A_{Ar}	peak area of compound argon in GC-trace of TCD

3.3.3.2 Conversion

Conversion is the amount of reactants that are converted relative to the amount of reactants fed to the reactor. The overall conversion of CO was calculated by subtracting CO flow rate in the tail gas (TG) from CO flow rate in the feed gas (FG). This subtraction was calculated as a fraction from the CO flow rate in the feed gas (FG) [86].

$$X_{CO} = \frac{F_{CO,feed} - F_{CO,tail}}{F_{CO,feed}} \cdot 100\%$$

where

X_{CO}	CO-conversion (%)
$F_{CO,feed}$	molar flow rate of CO in feed gas
$F_{CO,tail}$	molar flow rate of CO in tail gas

3.3.3.3 Integral rate of the Fischer-Tropsch synthesis

The integral rate of CO consumption towards the formation of Fischer-Tropsch products per unit mass catalyst is defined as the integral Fischer-Tropsch rate of the reaction. It is a direct indication of a catalyst activity in the Fischer-Tropsch reaction. It indicates the CO usage converted to Fischer-Tropsch products. This excludes the conversion of CO to CO_2 via the water gas shift reaction [86], which in the case of cobalt-based Fischer-Tropsch synthesis will be minimal, since the water-gas shift reaction does not play an important role during Fischer-Tropsch synthesis over cobalt-based catalysts [18].

$$r_{FT} = \frac{(F_{CO,feed} - F_{CO,tail}) - (F_{CO_2,feed} - F_{CO_2,tail})}{m_{cat}}$$

where

r_{FT}	Fischer-Tropsch reaction rate (mol/g/s)

m_{cat} catalyst mass loaded into the reactor (g)

3.3.3.4 Methane selectivity

The selectivity of a particulate hydrocarbon is defined as the amount of a chosen product formed (e.g. CH_4), relative to the amount of CO converted to Fischer-Tropsch products (excluding therefore CO_2). The methane flow rate can be quantified by using TCD analyses as described [86].

$$S_{CH_4} = \frac{F_{CH_4,tail}}{(F_{CO,feed} - F_{CO,tail}) - (F_{CO_2,feed} - F_{CO_2,tail})} \cdot 100\%$$

where

S_{CH_4} methane selectivity in C-%

CHAPTER 4

RESULTS

A model supported-cobalt catalyst was prepared to investigate whether re-dispersion occurs during oxidation and subsequent reduction of a cobalt catalyst. A supported-cobalt catalyst was subjected to consecutive oxidation and reduction treatments to obtain a better understanding of re-dispersion (see Table 3.1). An aluminium oxide (Ceralox APA-0.5) with a low surface area of 8.1 m^2/g was used as a support to prepare the model catalyst with a cobalt loading of 8 mass %.

4.1 Catalyst preparation

Supported-cobalt catalysts were prepared with Ceralox APA-0.5 alumina as support. The catalyst was prepared by impregnation of the support with cobalt nitrate solution. 10 g of cobalt was loaded on 90 g of support. The main batch (*Experiment 1*) was prepared by impregnation of the support with cobalt nitrate solution. This batch was used to produce other catalysts in either their reduced or oxidised state. One sample was oxidised at 10 bar (gauge pressure) to compare high pressure oxidation with oxidation at atmospheric pressure (0.86 bar).

4.1.1 Elemental analysis

Inductively coupled plasma (ICP) analysis was used to determine the metal loading on the prepared catalyst. The results of the ICP analyses are given in Table 4.1. From the obtained cobalt loading, the loading of the catalyst with Co_3O_4 was calculated. The analysis was done in duplicate and an average of 8.2 mass-% cobalt was obtained. A rather large deviation on the cobalt loading was obtained. The repeat analysis was performed one year later than the original analyses. The storage of the calcined catalyst on the shelf may have resulted in the adsorption of water and/or other compounds which will reduce the determined cobalt content (adsorption of 8 mass-% of water would result in this change of the measured cobalt loading). This error could have been reduced by not only determining the cobalt content, but also the aluminium content in the catalyst sample. This effect is over and above the normal error in measurement for ICP.

The calcined mass of the catalyst was used during the determination of the cobalt content with ICP. However, to reduce the influence of the catalyst mass on the analyses (in particular during reduction and re-oxidation), the amount of cobalt is presented as mass cobalt per gram α-Al_2O_3 as well (see Table 4.1).

Table 4.1: *Cobalt loading (mass-%) in the model catalyst*

Sample	Co-loading mass-%	Co_3O_4-loading mass-%	Co/Al_2O_3 g/g
Exp 1	8.5	11.6	0.096
Exp 1 (repeat)	7.8	10.6	0.087
Average	8.2	11.1	0.092

4.1.2 Oxygen consumption during high-pressure oxidation

Following the oxidation and reduction, one catalyst sample was re-oxidised at 10 bar gauge pressure (the high-pressure oxidation). The oxygen concentration in the effluent was monitored during the high-pressure oxidation (the experimental set-up is shown in Figure 3.6). Figure 4.1 shows the measured outlet oxygen concentration as a function of time (the temperature recorded by the second thermocouple in the catalyst bed as a function of time is displayed as well; the thermocouple was placed 4 cm from the bottom of the reactor). The oxygen concentration is lower than 21% because the oxygen concentration in the Afrox air cylinder had an allowable variation of 19% to 21%.

The oxidation of metallic cobalt starts at ca. 150°C. This oxidation temperature was also reported in the literature with TPO experiments recorded on SiO_2-Al_2O_3 supported-cobalt catalysts [87]. From the drop in the oxygen concentration as a function of time, the uptake of oxygen by the catalyst can in principle be determined. It was estimated that 0.1 mmol of O_2 was taken up by 1 g of catalyst in the temperature range between 150 and 245°C. This indicates that either the cobalt is not completely oxidized to either CoO or Co_3O_4 (an average stoichiometric formula of $CoO_{0.14}$ was determined) or the method used here is far too inaccurate to determine the oxygen uptake.

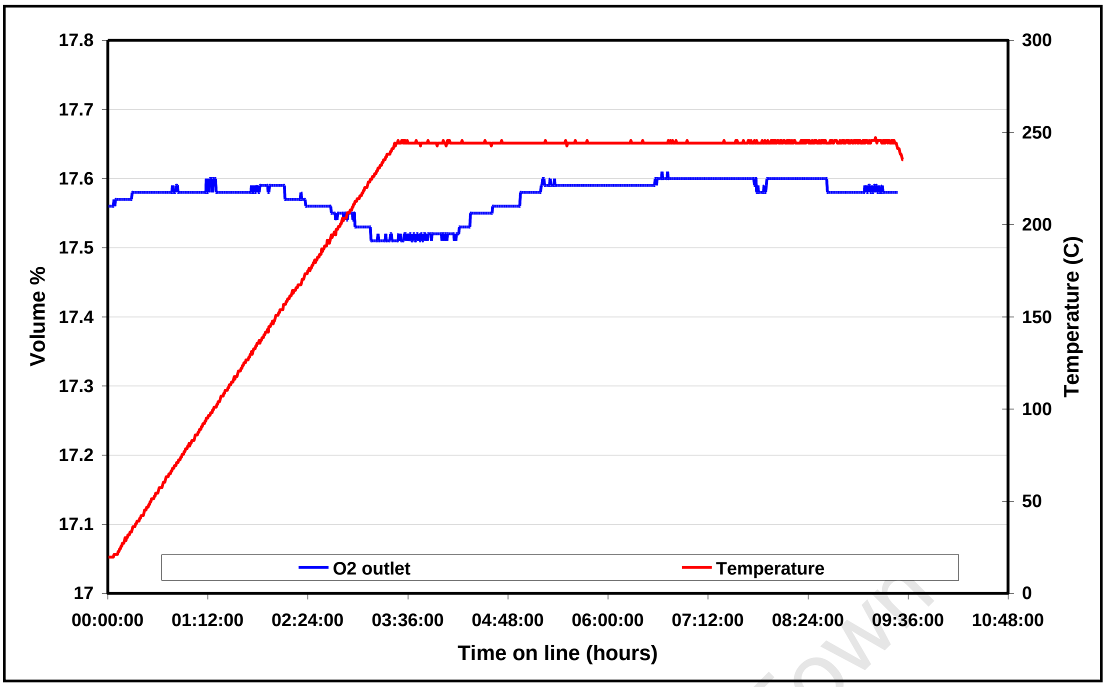

Figure 4.1: *Concentration of oxygen in the outlet and temperatures measured during high-pressure oxidation (Experiment 5)*

4.2 Catalyst characterization

The catalysts were characterized using XRD, *in-situ* XRD, XPS, TEM, H_2 chemisorption, and TPR to elucidate the effect of consecutive oxidation reduction cycles on the physico-chemical characteristics of the catalyst sample.

4.2.1 X-ray diffraction (XRD)

Ex-situ X-ray diffraction was used to identify the crystalline phases and to determine crystallite sizes using Rietveld refinement. Co_3O_4 and CoO crystallites exhibit well-defined XRD patterns, which makes XRD suitable as a characterization technique. Crystallite sizes can be determined from powder XRD-patterns and relative accurate sizes can be determined in the range of 4 – 50 nm. For very small and very large crystallites the accuracy for measuring crystallite sizes is lower. The XRD technique is not very sensitive to the measurement of very small crystallites sizes (<2-3nm) because the peaks are getting too broad. Peak broadening can also be caused by the presence of strained or imperfect crystals [88].

Different oxidation-reduction treatments (OROR; O = oxidation and R = reduction) were conducted to generate the different samples. One sample was oxidised at 10 bar gauge pressure to compare high pressure oxidation with oxidation at atmospheric pressure. After their pre-treatment, the reduced samples were unloaded in dry ice prior to the XRD analysis.

Figure 4.2 shows the obtained XRD-pattern of the freshly calcined catalyst sample, i.e. prior to the first reduction step (*Experiment 1*). Cobalt is present as Co_3O_4 as evidenced by the diffraction peaks at a diffraction angle of 2Θ = 36.5^{o}, 43,0^{o}, 52.6^{o}, 70.3^{o}, and 77.5^{o} (using Co-Kα radiation). The diffraction pattern of Co_3O_4 can be clearly distinguished from the diffraction pattern of the support, i.e. α-Al_2O_3, which is a distinct advantage in comparison to the XRD-analysis of Co/γ-Al_2O_3 where the diffraction peaks of Co_3O_4 overlap with those of the support.

The different average crystallite sizes of the various phases present in the catalyst after the various pre-treatment steps are shown in Table 4.2 and the relative abundance of the crystallite phases are shown in Table 4.3.

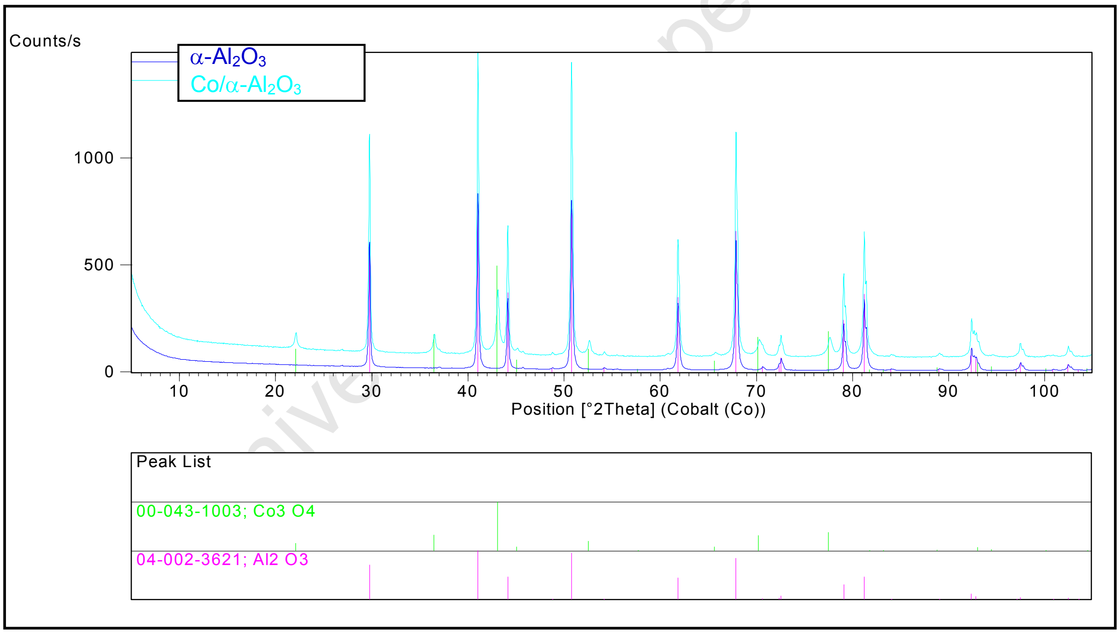

Figure 4.2: *XRD-pattern of α-Al_2O_3 and Co/α-Al_2O_3 after calcination (Experiment 1)*

The crystallite size of the support (α-Al_2O_3) after the preparation of the calcined, model catalyst without any further treatment (i.e. in *Experiment 1)* was very similar to the crystallite size of α-Al_2O_3, i.e. 152 and 141 nm. These average crystallite sizes can be considered to be identical taking into account that size determination using XRD is not that accurate for these large crystallites. The crystallite size of the support (α-Al_2O_3) increased after the first reduction step to 189 nm. This may be due to sintering during reduction, since water generated in the reduction process may accelerate the sintering process. Further reduction and oxidation treatments did not have any influence on the crystallite size of α-Al_2O_3.

Table 4.2: *Average crystallite sizes of the support (α-Al_2O_3) the various cobalt phases after the various treatments as determined by ex-situ XRD*

Sample name	Oxidation/ reduction steps	$d_{\alpha\text{-}Al_2O_3}$ (nm)	$d_{Co_3O_4}$ (nm)	d_{CoO} (nm)	$d_{fcc\text{-}Co}$ (nm)	$d_{hcp\text{-}Co}$ (nm)
Support		141	-	-	-	-
Exp 1	O	152	33	-	-	-
Exp 2	OR	189	-	-	34	6
Exp 3	ORO	188	9	14	-	21
Exp 4	OROR	187	-	-	-	-
Exp 5	OR_HP O	191	6	-	-	-

Table 4.3: *Relative abundance (in mass-%) of crystalline phases detected by ex-situ XRD after the various treatments*

Sample name	Oxidation/ reduction steps	α-Al_2O_3	Co_3O_4	CoO	fcc-Co	hcp-Co
Support		100	0	0	0	0
Exp 1	O	91	9	0	0	0
Exp 2	OR	94	0	0	1	4
Exp 3	ORO	92	6	< 1	0	1
Exp 4	OROR	100	0	0	0	0
Exp 5	OR_HP O	91	9	0	0	0

The relative abundance of Co_3O_4 in the calcined catalyst sample (*Experiment 1*) as determined by Rietveld refinement of the XRD-pattern was ca. 9 % m/m Co_3O_4 (a similar amount was determined after *Experiment 5*, in which the reduced catalyst sample was exposed to high pressure oxidation), which is lower than the calculated value of 11 % from ICP analyses (see 4.1.1). This means that some cobalt could not be detected by XRD.

The oxidation of a reduced catalyst sample (*Experiment 3*) does not go to completion in the time frame of the experiments. Cobalt(II)oxide and metallic cobalt were detected after reduction and re-oxidation of the sample. However, the amounts of CoO and metallic cobalt are very small with a relative abundance of 1 mass-% or less for each.

The passivation of the samples after reduction by unloading the catalyst sample in dry ice under argon was successful as evidenced by the absence of XRD-visible cobalt oxide phases in the sample. fcc-Co and hcp-Co were detected after reduction of the calcined catalyst (*Experiment 2*). The cobalt metal loading determined using *ex-situ* XRD in *Experiment 2* (5 %) was low when compared with the ICP value of 8.2 % (see 4.1.1). After the second reduction (*Experiment 4*) no metallic cobalt was detected, probably due to a too small crystallite size (the lower size limit in crystallite size determination using XRD is ca. 3-5 nm, depending on the noise level). The metal loading in all reduced samples is significantly less than expected, implying that quite of large fraction of the cobalt has become ‘XRD-invisible’, i.e. too small to detect.

The Co_3O_4 crystallite size (see Table 4.2) decreased from 33 nm after the 1st oxidation step to 9 nm after the second oxidation step (ORO - *Experiment 3*). ORO treatment resulted in a smaller Co_3O_4 crystallite than found for the freshly prepared catalyst. The smallest Co_3O_4 crystallite size of 6 nm was obtained with the high pressure oxidation step of a previously reduced catalyst sample. The differences in the average crystallite size of Co_3O_4 are shown In Figure 4.3.

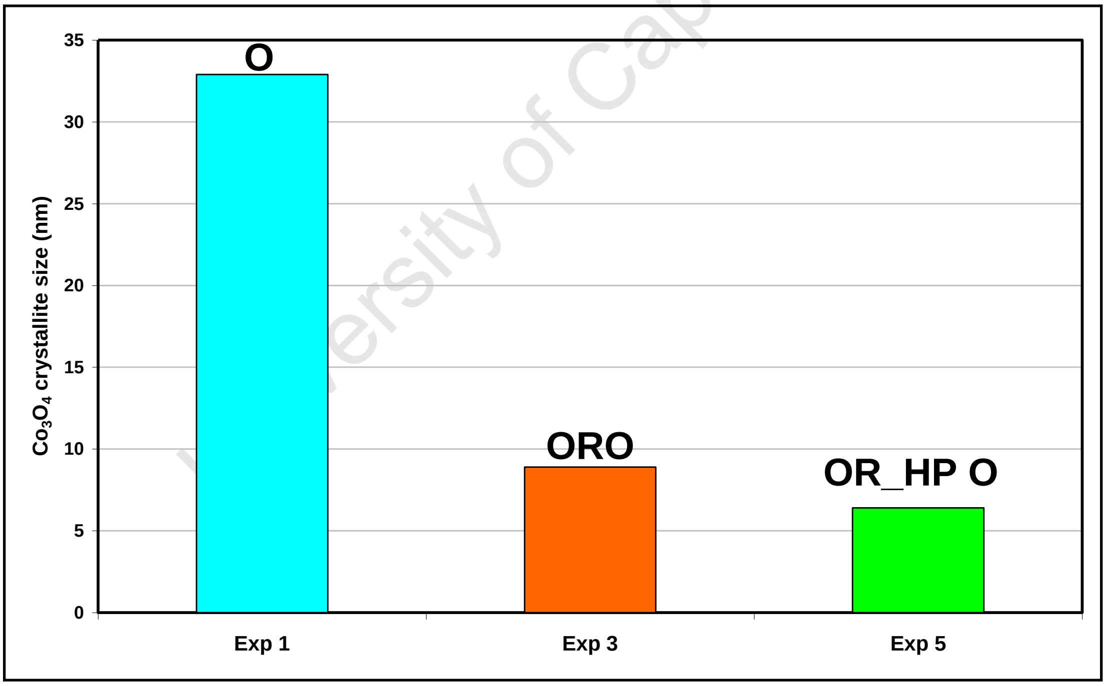

Figure 4.3: *Co_3O_4 crystallite sizes in the model alumina supported cobalt catalyst after preparation (O: Experiment 1), re-oxidation of the reduced catalyst (ORO: Experiment 3) and re-oxidation of the reduced catalyst at high pressure (OR_HP O: Experiment 5)*

4.2.2 Oxidation-reduction cycles monitored using *in-situ* X-ray diffraction (XRD)

In-situ XRD was used to determine crystallite sizes and phase changes during consecutive reduction and oxidation steps after the initial calcination of the catalyst precursor (i.e. after *Experiment 1*).

It should however be noted that the treatment conditions differed between the *ex-situ* samples and the treatment in the *in-situ* experiment. The reduction of the calcined catalyst precursor was performed for only 2 hrs (instead of 10 hrs for the *ex-situ* experiment) at 425°C (obtained with a heating rate of 5°C/min instead of 1°C/min) under hydrogen with a space velocity of 3000 ml(STP)/hr/$g_{catalyst}$ (instead of 2000 ml(STP)/hr/$g_{catalyst}$). The different heating rates employed during the reduction step and the shorter reduction time may have resulted in differences between the *ex-situ* XRD and *in-situ* XRD results.

The subsequent *in-situ* oxidation step of the *in-situ* reduced catalyst sample was performed in 5% O_2/He, and hence 4 times lower partial pressure of oxygen. Furthermore, the *in-situ* oxidation was performed at a higher temperature (300°C instead of 250°C) using a higher heating rate (3°C/min vs. 1°C/min) for a shorter time (no hold time at 300°C instead of 6hrs at 250°C) with a lower space velocity of oxygen (150 vs. 300 ml(STP) O_2/hr/$g_{catalyst}$, and the the overall gas space velocity was 3000 instead of 1430 ml (STP)/hr/$g_{catalyst}$).

4.2.2.1 Relative abundance of the cobalt phases during reduction-oxidation cycles

In Figure 4.4, the change in relative abundance of the various crystallite phases is shown as a function of time on line and exposure to various atmospheres at various temperatures during the *in-situ* XRD-experiment. The reduction regions are highlighted light blue and the oxidation regions are highlighted light pink.

During the first reduction step a slight initial increase in the abundance of the Co_3O_4 phase is observed after which the abundance Co_3O_4 declined with a simultaneous increase in the CoO phase. The cobalt metal hcp and fcc phases started to form after almost all the Co_3O_4 had been transformed into CoO. This implies that the reduction of Co_3O_4 follows a two step process, viz. $Co_3O_4 \rightarrow CoO \rightarrow Co$ as previously noted [41,87]. No CoO was observed at temperatures higher than ca. 340ºC. The hcp-Co and fcc-Co formed initially in a ratio of 1:1 after which relatively more hcp-Co is formed. At the temperature (ca. 320°C) at which an increased formation of hcp-Co was observed relative to fcc-Co a shoulder is observed in the abundance of the CoO phase implying a lower rate of reduction of CoO to the additional hcp-Co.

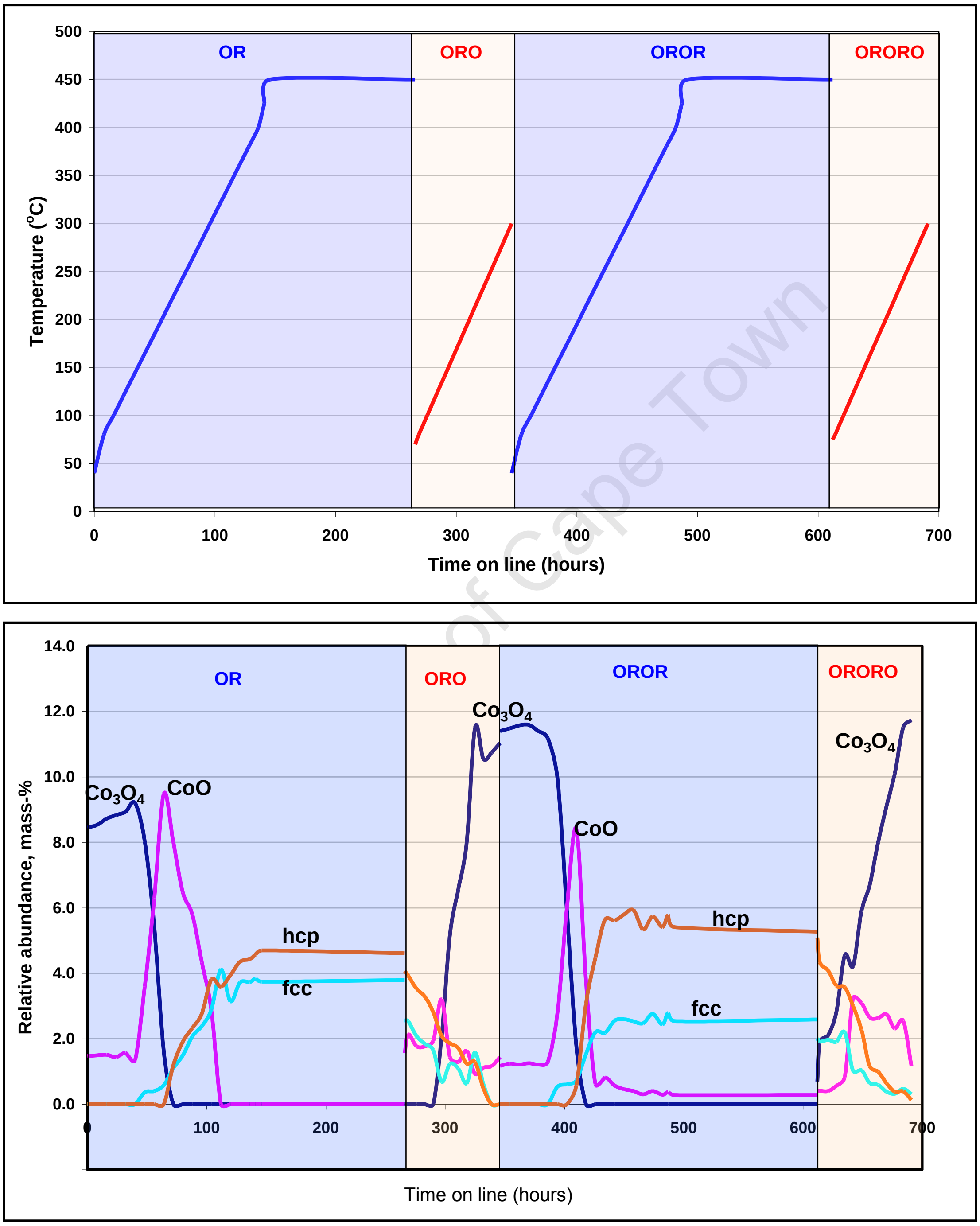

Figure 4.4: *Relative abundance of various cobalt phases during consecutive reduction and oxidation steps as monitored using in-situ XRD (blue shaded area: reduction; red shaded area: oxidation)*

The measured abundance of the CoO phase during the first oxidation step starts at 1.6 mass % where it has ended on 0 mass % after the first reduction. This indicates that oxidation occurs immediately upon introduction of the O_2/He stream at room temperature. A higher abundance of Co_3O_4 was observed following the oxidation of the reduced sample in comparison to the abundance of Co_3O_4 in the starting material. The phase change to Co_3O_4 was rapid during the oxidation step. It was easier to oxidise the sample than to reduce then because the rate of formation of Co_3O_4 (as evidenced by the slope of the abundance of Co_3O_4 as a function of time) during the oxidation was higher than the rate of consumption of Co_3O_4 during the 1st reduction step. The relative amount of the CoO phase formed was less during oxidation than during the first reduction step. It might be concluded that the oxidation of metallic cobalt may proceeds directly to Co_3O_4.

During the second reduction step, like in the first reduction step a slight initial increase in the abundance of the Co_3O_4 phase is observed after which the abundance of Co_3O_4 decreased with a simultaneous increase in the abundance of the CoO phase. During this step it seems that less CoO is formed compared to that formed in the first reduction step. The cobalt metal hcp and fcc phases started to form when almost all the Co_3O_4 had been converted to CoO. No CoO was observed at temperatures higher than ca. 260ºC. hcp-Co and fcc-Co formed initially in a ratio of 1:1 for a very short period. At temperatures higher than ca. 240ºC relatively more hcp-Co is formed than fcc-Co. The preferential formation of hcp-Co in comparison to fcc-Co occurred during the second reduction step at lower temperature than formed during the first reduction step. After the second reduction the amount of fcc-Co in the fraction of metallic cobalt (i.e. fcc-Co plus hcp-Co) is lowered from 45 mass % to 32 % and the Co hcp increased from 55 mass % to 67 % (see Table 4.4) in comparison to the 1st reduction step.

Table 4.4: *Relative abundance of crystalline metallic cobalt phases (% (m/m) after the reduction steps in the in-situ XRD experiments (in brackets fraction of a particular metallic cobalt phase is given)*

Sample name	**Oxidation/ reduction steps**	**Co(fcc)**	**Co(hcp)**	**Total Co^0**
in-situ reduction step 1	OR	3.8 (45%)	4.6 (55%)	8.4
in-situ reduction step 2	OROR	2.6 (32%)	5.3 (67%)	7.9

The second oxidation step seems very similar to the first oxidation step. The phase change to Co_3O_4 was rapid during the oxidation step and only a small amount of CoO phase was formed followed by the formation of Co_3O_4. It seems that the oxidation step is not significantly influenced by the history of the catalyst sample in contrast to the reduction process.

4.2.2.2 Mass ratio of cobalt to alumina during consecutive reduction-oxidation cycles

The mass cobalt metal per the mass of the α-Al_2O_3 was calculated in order to understand the differences in amount of Co_3O_4 formed during the two oxidation steps observed during the *in-situ* XRD. The total amount of cobalt metal per gram α-Al_2O_3 was plotted as a function of time on line for the whole of the *in-situ* XRD experiments, i.e. the consecutive reduction-oxidation-reduction-oxidation run (see Figure 4.5). The total amount of cobalt per gram α-Al_2O_3 was 0.097 ± 0.015 g. However, an increase in mass of cobalt relative to the mass of α-Al_2O_3 is observed during the last step of the *in-situ* XRD experiments. It might be speculated that this behaviour is due to the formation of XRD-invisible alumina.

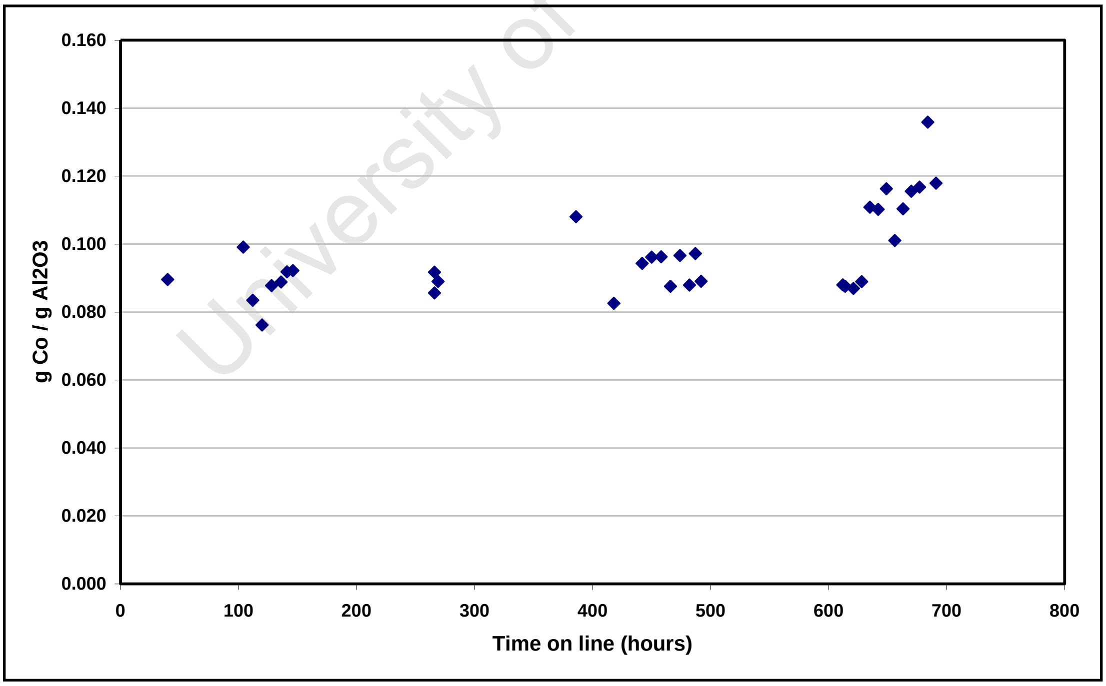

Figure 4.5: *Abundance of total cobalt relative to the abundance of α-Al_2O_3 during the consecutive oxidation reduction cycles of the model alumina supported cobalt catalyst*

4.2.2.3 *Change in the average crystallite size of alumina and cobalt phases during consecutive reduction-oxidation cycles*

During the first reduction step the crystallite size of the support (α-Al_2O_3) increased with time on line from 140 nm to 170 nm (see Figure 4.6), as was also observed during the *ex-situ* XRD studies. This might be ascribed to water-aided sintering during the reduction process. The consecutive oxidation and reduction steps do not seem to change the average crystallite size of α-Al_2O_3 further, but a small further increase was observed during the last oxidation step.

The Co_3O_4 crystallite sizes decreases marginally up to a temperature of 180°C during the first reduction step after which a sudden decrease in both the amount of Co_3O_4 and the size of Co_3O_4 is observed. The average crystallite size of CoO increases during the first reduction step and passes through a maximum. It might be speculated that initially small CoO crystallites break off during the reduction of large crystallites of Co_3O_4, which are subsequently further reduced to metallic cobalt. The subsequent oxidation of the reduced catalyst sample yields CoO and Co_3O_4. The average crystallite size of CoO shows some scatter, but does not seem to change much (10.4 ± 2.4 nm), whereas the average crystallite size of Co_3O_4 increases with increasing oxidation temperature (from ca. 3 to 9 nm). The average crystallite size of Co_3O_4 remains at ca. 9 nm during the consecutive reduction step, whereas the average crystallite size of CoO increases strongly from 5 nm to ca. 120 nm. This may indicate that the reduction of the few large crystallites of CoO is kinetically hindered and survive the rather high reduction temperature. A decrease in the average crystallite size of CoO (down to ca. 5 nm) is observed during the consecutive oxidation step. Initially, small Co_3O_4 crystallites are observed (ca. 5 nm) during this oxidation step, whose average size increases with increasing oxidation temperature (up to ca. 9 nm).

The average crystallite size of hcp-Co remained relatively constant (at ca. 5 nm) during the reduction-oxidation cycles in the *in-situ* XRD experiment. During the last oxidation step an increase in the average crystallite size of the remaining hcp-Co was observed implying the presence of (some) large hcp-Co crystallites after the 2nd reduction step, which are difficult to reduce.

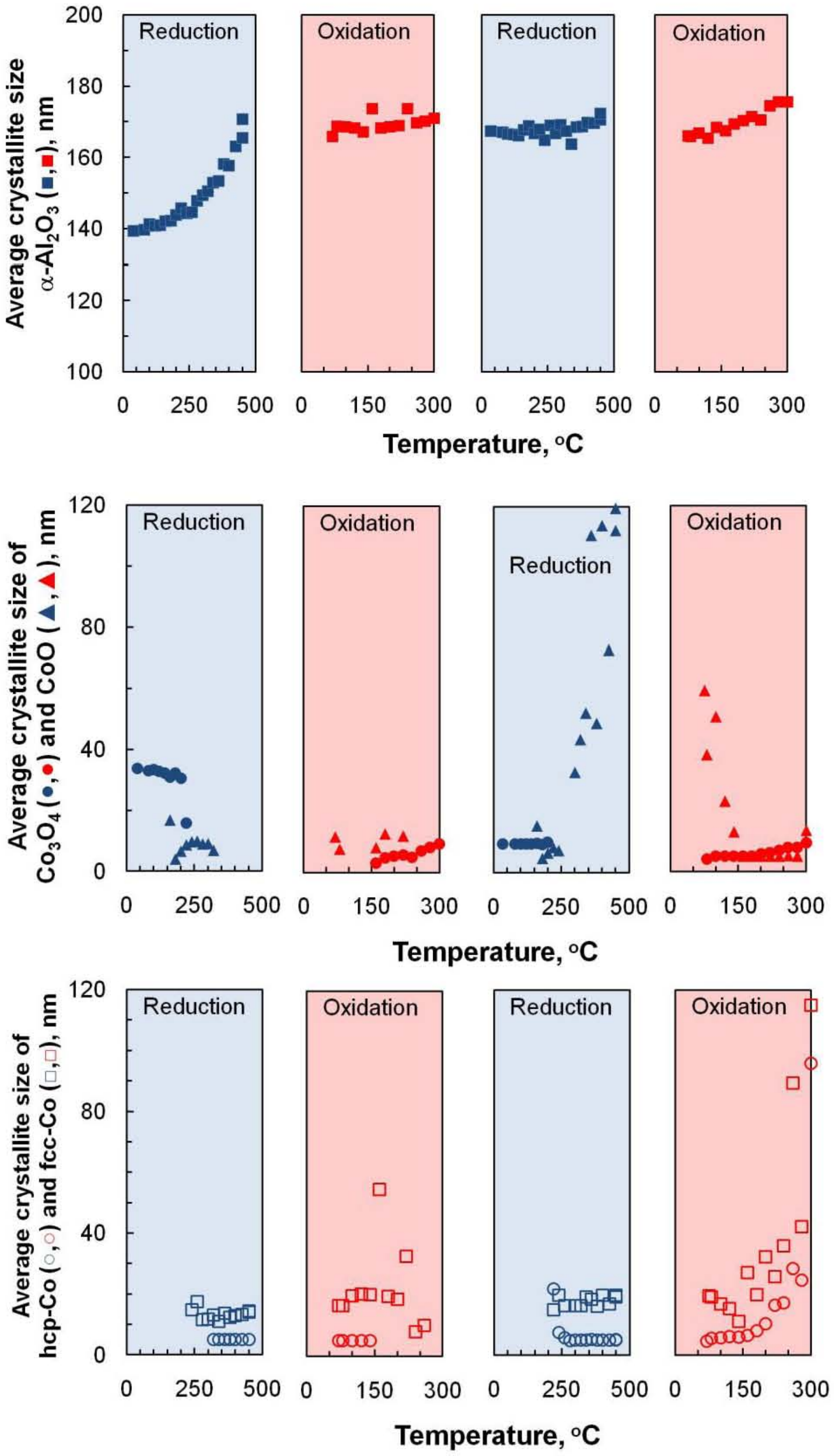

Figure 4.6: *Average crystallite sizes of* α*-*Al_2O_3 *(top),* Co_3O_4 *and CoO (middle) and hcp-Co and fcc-Co (bottom) during the consecutive oxidation reduction cycles of the model alumina supported cobalt catalyst*

The average crystallite size of fcc-Co is much larger than that of hcp-Co (with 13-14 nm for fcc-Co vs. ca. 5 nm for hcp-Co upon reduction of the freshly calcined catalyst). In general, the obtained crystallite sizes for fcc-Co are ca. 3 times larger than the average crystallite size for hcp-Co with exception of those found after the 2nd oxidation step when the average crystallite size of the remaining cobalt crystallites is large.

4.2.3 X-ray photoelectron spectroscopy (XPS)

XPS analyses were performed to give insight on the surface properties of the calcined catalysts, specific on the oxidation state of the cobalt oxides. In Figure 4.7 the Co_{2p}-region of the XPS-spectra obtained with the model catalysts after *Experiment 1*, *Experiment 3* and *Experiment 5* are compared with the XPS spectra of bulk Co_3O_4 and CoO reference materials. Two large peaks were observed in the spectra, i.e. $Co_{2p_{3/2}}$ and $Co_{2p1/2}$. High spin Co^{2+} compounds such as CoO exhibit strong satellite lines which are located 5-6 eV above the photo line whereas the low spin compound Co_3O_4 (Co^{3+}/Co^{2+} in a 2:1 ratio) exhibit very weak satellite peaks that

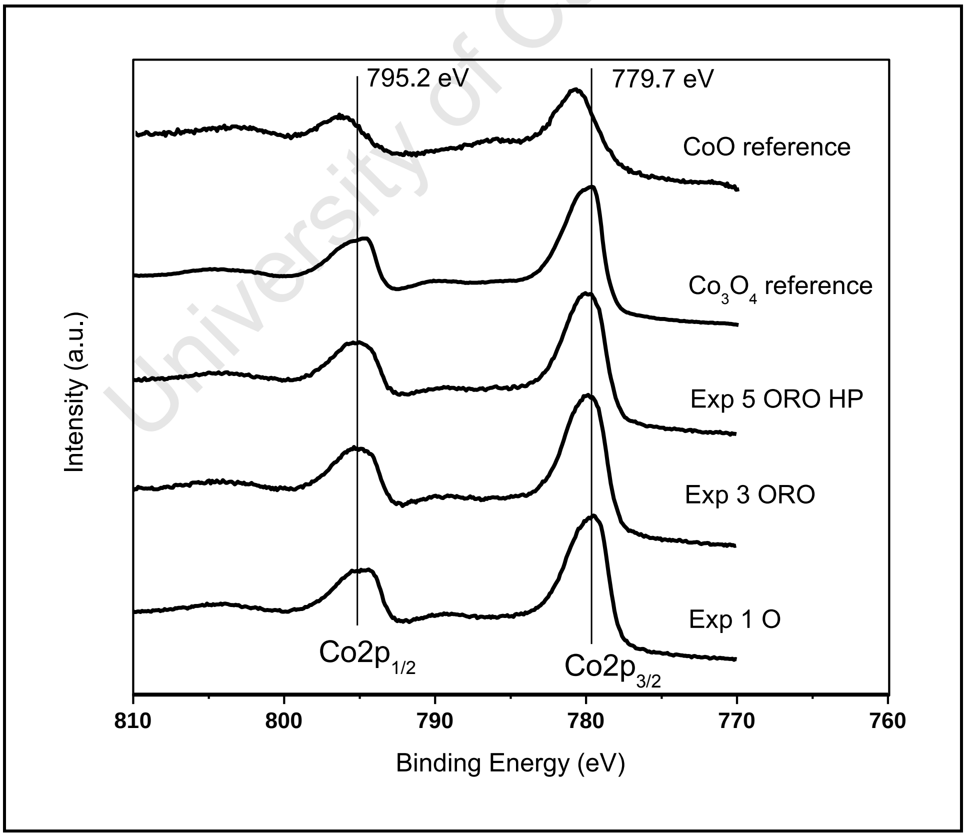

Figure 4.7: *Co_{2p} region of XPS spectrum of the model alumina supported cobalt catalyst after Experiment 1, Experiment 3 and Experiment 5 (the reference spectra for CoO and Co_3O_4 are shown as well)*

are normally 10-11eV from the main photoline [4]. Weak shake-up satellite peaks were observed for the model catalysts after *Experiment 1*, *Experiment 3* and *Experiment 5* showing that Co_3O_4 is present in the samples. The binding energy of the samples is similar to that of Co_3O_4 and doublet separation is around 15.5 eV. This all indicates that Co_3O_4 is the dominant phase on the surface of all the oxidised catalysts.

4.2.4 Transmission electron microscopy (TEM)

TEM analyses were performed to support the XRD studies and to obtain images of the morphological changes and changes in crystallite sizes. TEM analyses were also performed on the support.

4.2.4.1 Support (Ceralox APA-0.5 alumina)

TEM images were obtained of the support before it was used for impregnation (see Figure 4.8) and a support sample that was exposed to similar conditions as the model catalyst during calcination and reduction (see Figure 4.9). During the reduction experiment of the support, water vapour was added to simulate the reduction of a supported cobalt catalyst. The aim was to observe if water, during reduction, may have caused any roughening of the support. There is no visual difference between the untreated support and the support treated at 425°C with hydrogen (92 ml (STP)/min/$g_{support}$) saturated with water (p_{H_2O} = 2.7 kPa) implying absence of roughening of its surface as a consequence of the treatment in a hydrogen/water mixture.

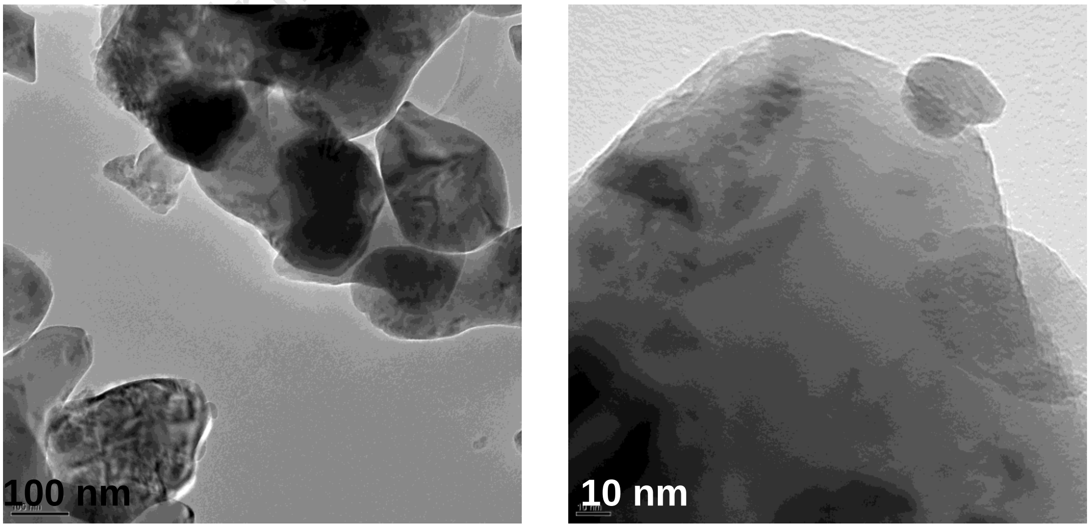

Figure 4.8: *TEM-images of Ceralox APA-0.5 alumina (lot number C816982) as received*

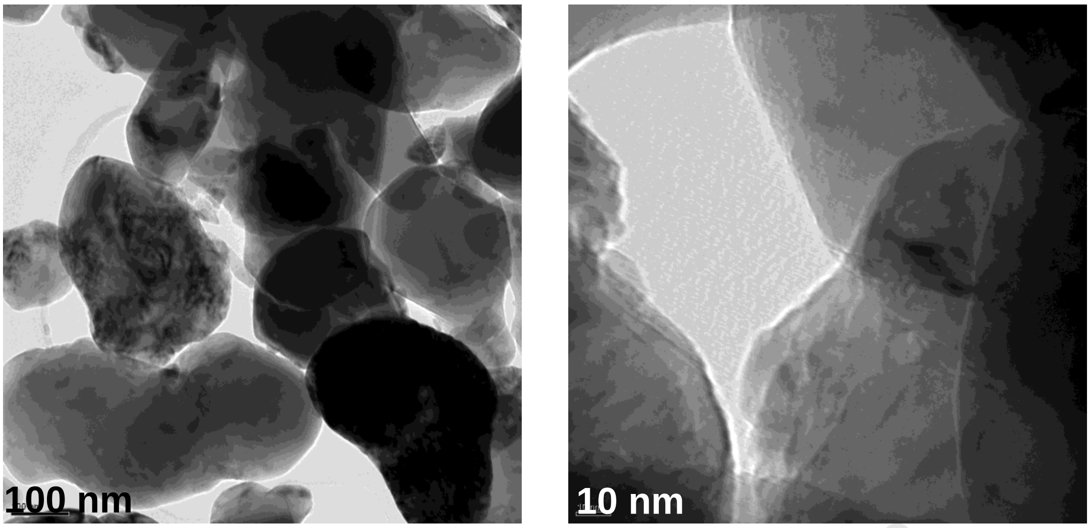

Figure 4.9: *TEM-images of Ceralox APA-0.5 alumina (lot number C816982) after oxidative treatment and subsequent treatment in hydrogen saturated with water*

4.2.4.2 Experiment 1 (calcined model catalyst)

Figure 4.10 shows the TEM-image of the freshly calcined catalyst sample. Cobalt is not homogeneously distributed over the surface of the support and it is partially present in clusters. The formation of cobalt clusters in catalysts prepared with cobalt nitrate has been observed previously [89] and has been attributed to the formation of cobalt nitrate droplets during the drying process. Some Co_3O_4 seems to crystallize out in “worm”-like structures.

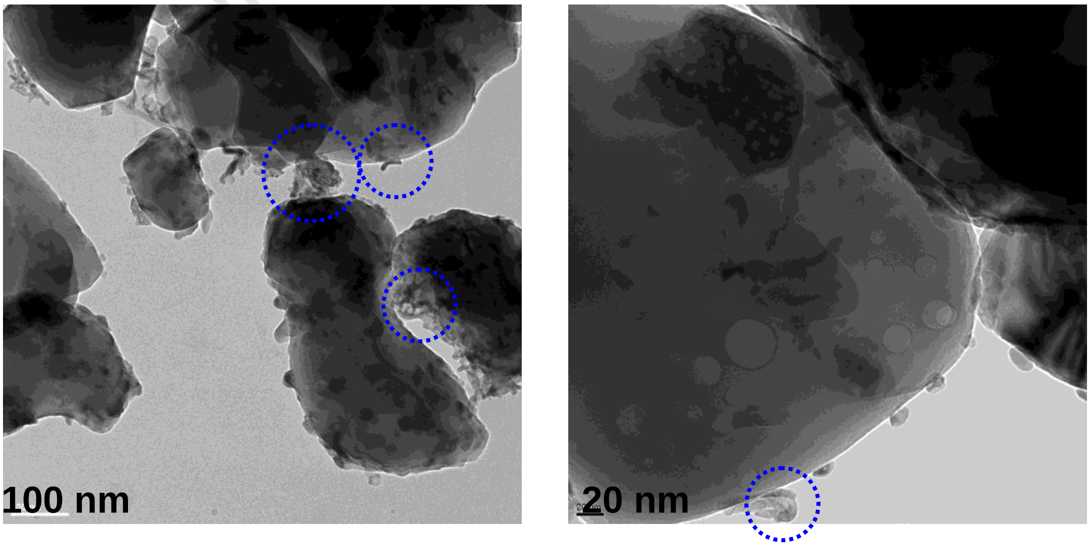

Figure 4.10: *TEM-images of the calcined model alumina supported cobalt catalyst (after Experiment 1); encircled regions show “worm”-like crystallites)*

4.2.4.3 Experiment 2 (passivated, reduced model catalyst)

The reduced sample was unloaded in dry ice and an oxide layer was formed around the metal particle. This oxide layer can be seen in the enlargement shown in Figure 4.11 (blue dots) and has a thickness of approximately 2 nm. The formation of a thin oxide layer upon passivation can be explained by the Cabrera-Mott theory [76]. This low temperature oxidation theory is based on the formation of an oxide layer which grows by migration of cobalt ions through the layer. After the formation of an initial oxide layer of a certain thickness, thermal activated ion migration is necessary for further growth of the oxide layer.

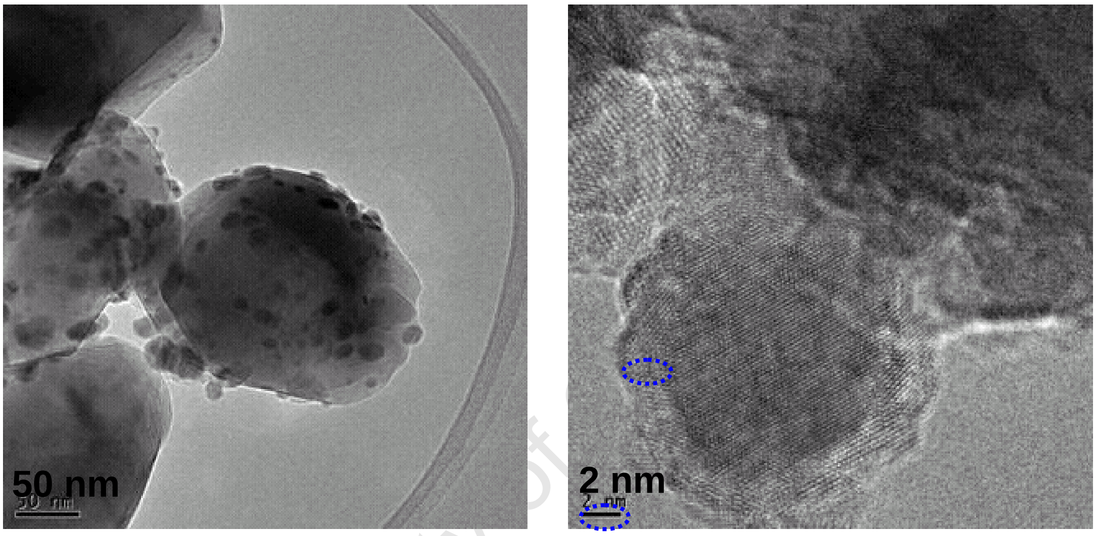

Figure 4.11: *TEM-images of the passivated catalyst after Experiment 2 (OR) (right: cobalt particles on spherical alumina support particles; left: enlargement of a cobalt particle showing the formation of a thin oxide layer due to passivation)*

The crystallite size of cobalt was estimated from the TEM-image (see Figure 4.12 - crystallite size estimated from the encircled crystallites) to be 10.6, 15.4, 13.8 and 9.0 nm.

4.2.4.4 Experiment 3 (re-oxidised, reduced model catalyst)

The oxidation of a previously reduced sample leads to the formation of hollow spheres (see Figure 4.13), as previously reported for the oxidation of nano-sized cobalt crystallites [74,75]. The shell of the hollow sphere can be seen as a darker ring. The formation of hollow spheres during the oxidation of a previously reduced catalyst sample can be described by the Kirkendall effect. This effect occurs when the mutual diffusion rates of two components, e.g. cobalt and oxygen differ by a

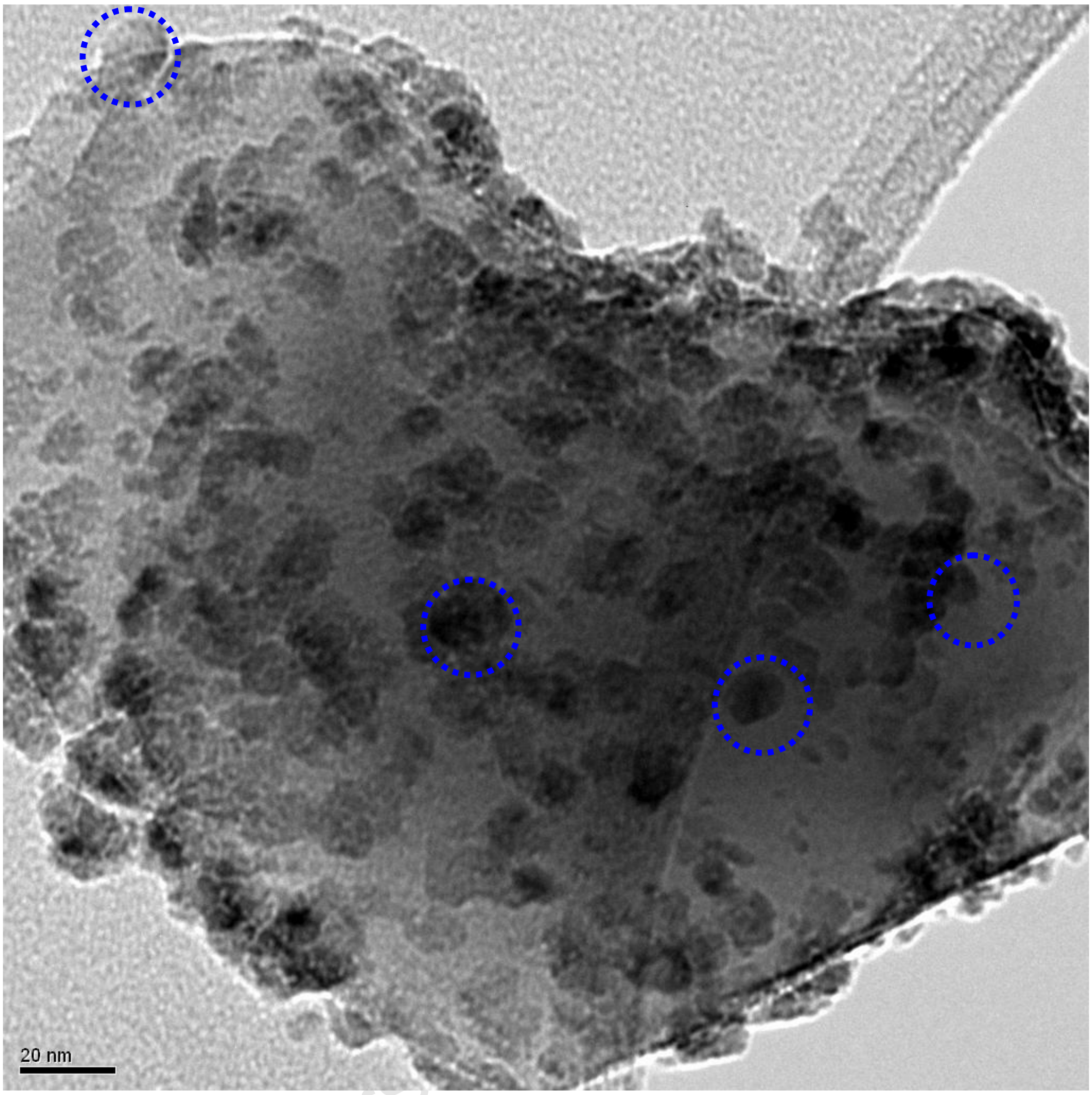

Figure 4.12: *TEM-image of the passivated catalyst after Experiment 2 (OR) (circled crystallites were used to estimate the crystallite size)*

considerable amount [74]. A hollow sphere will be formed when the outward diffusion of the cobalt is much faster than the inward diffusion of the oxygen. The outer shell of the hollow sphere is made up from different crystalline domains (see Figure 4.14) and hence the diameter of the shell is not constant. The average diameter of the crystallites in the shell of the hollow spheres is 9 nm (± 2.8 nm). The diameter of the irregular crystalline domains varied from 5 nm to 13 nm.

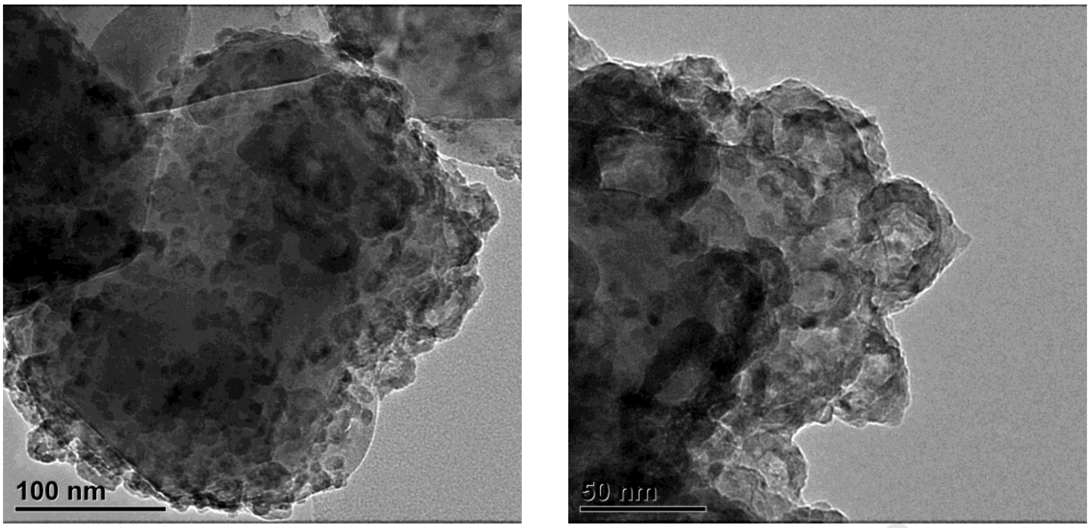

Figure 4.13: *TEM-images of the model catalyst after Experiment 3 (oxidation of the reduced model alumina supported catalyst - ORO) showing the hollow sphere formation during ORO cycle*

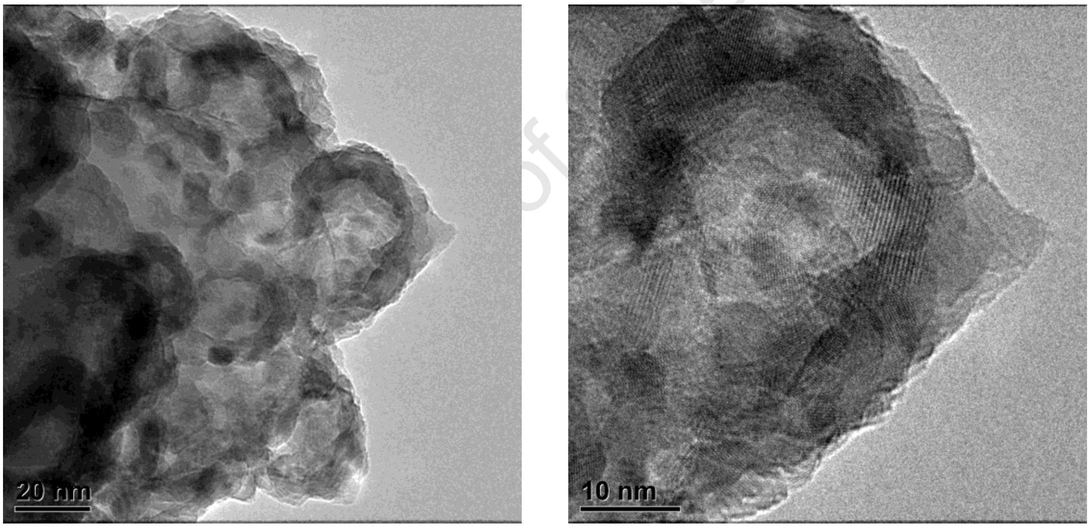

Figure 4.14: *TEM-images of the model catalyst after Experiment 3 (oxidation of the reduced model alumina supported catalyst - ORO) showing the shell of the hollow spheres formed during ORO*

4.2.4.5 Experiment 4 (passivated sample after reduction of the re-oxidised model catalyst)

Small crystallites were formed during the second reduction step following the formation of hollow spheres in the oxidation of the previously reduced catalyst (see Figures 4.15). The crystallites seem to be hemispherical in size (see Figure 4.16) with estimated crystallite sizes of 2.8, 3.4, 3.1 and 3.3 nm (see Figure 4.17 - measured crystallites surrounded with a circle).Lattice fringes can be observed on a variety of crystallites, from which observed lattice spacings of 2.30 Å, 2.32 Å and 2.41 were determined. The observed lattice spacing does correspond most likely to the (222) reflection of Co_3O_4 ($d_{(222)}$ = 2.333 Å) [90] or α-Al_2O_3 ($d_{(110)}$ = 2.379 Å) [91], but cannot be related to the typical dominant reflections fcc-Co ($d_{(110)}$ = 2.506 Å; $d_{(111)}$ =2.047 Å), hcp-Co ($d_{(100)}$ = 2.165 Å), CoO ($d_{(111)}$ = 2.461 Å; $d_{(200)}$ = 2.131 Å).

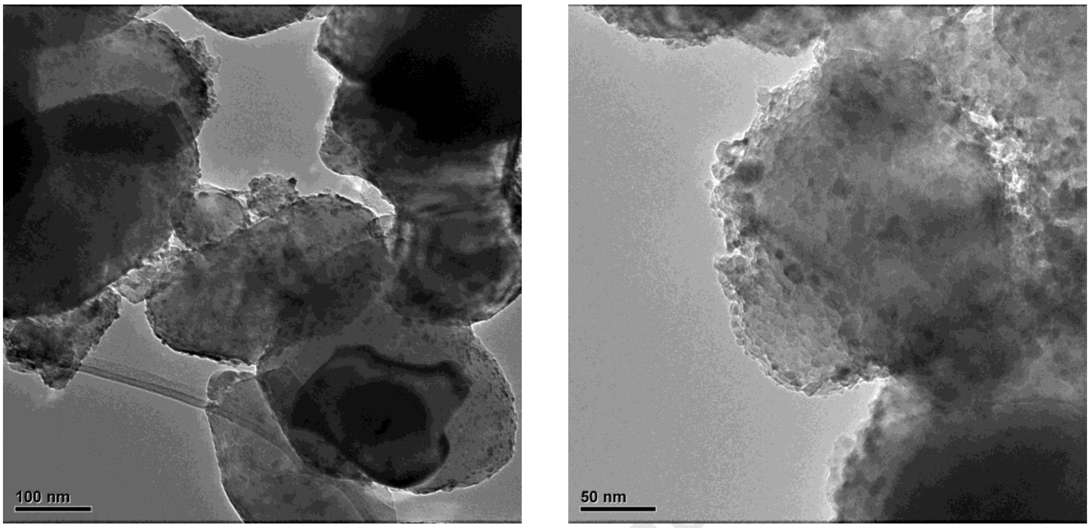

Figure 4.15: *TEM-images of the passivated model catalyst after Experiment 4 (reduction of the re-oxidised, reduced model alumina supported catalyst - OROR) showing the formation of small cobalt crystallites during OROR*

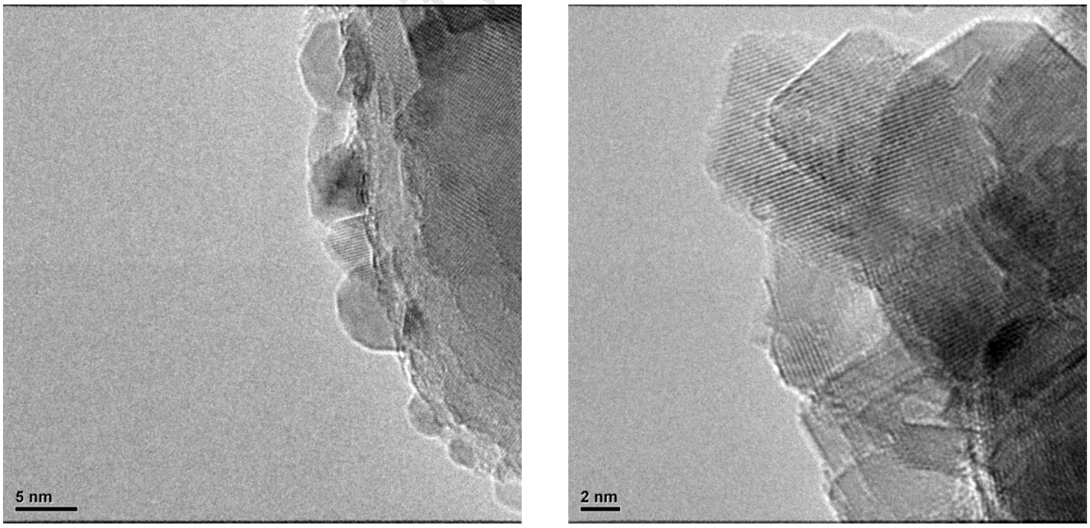

Figure 4.16: *TEM-images of the passivated model catalyst after Experiment 4 (reduction of the re-oxidised, reduced model alumina supported catalyst - OROR) showing the formation of small, hemispherical cobalt crystallites and the lattice spacing in the cobalt crystallites*

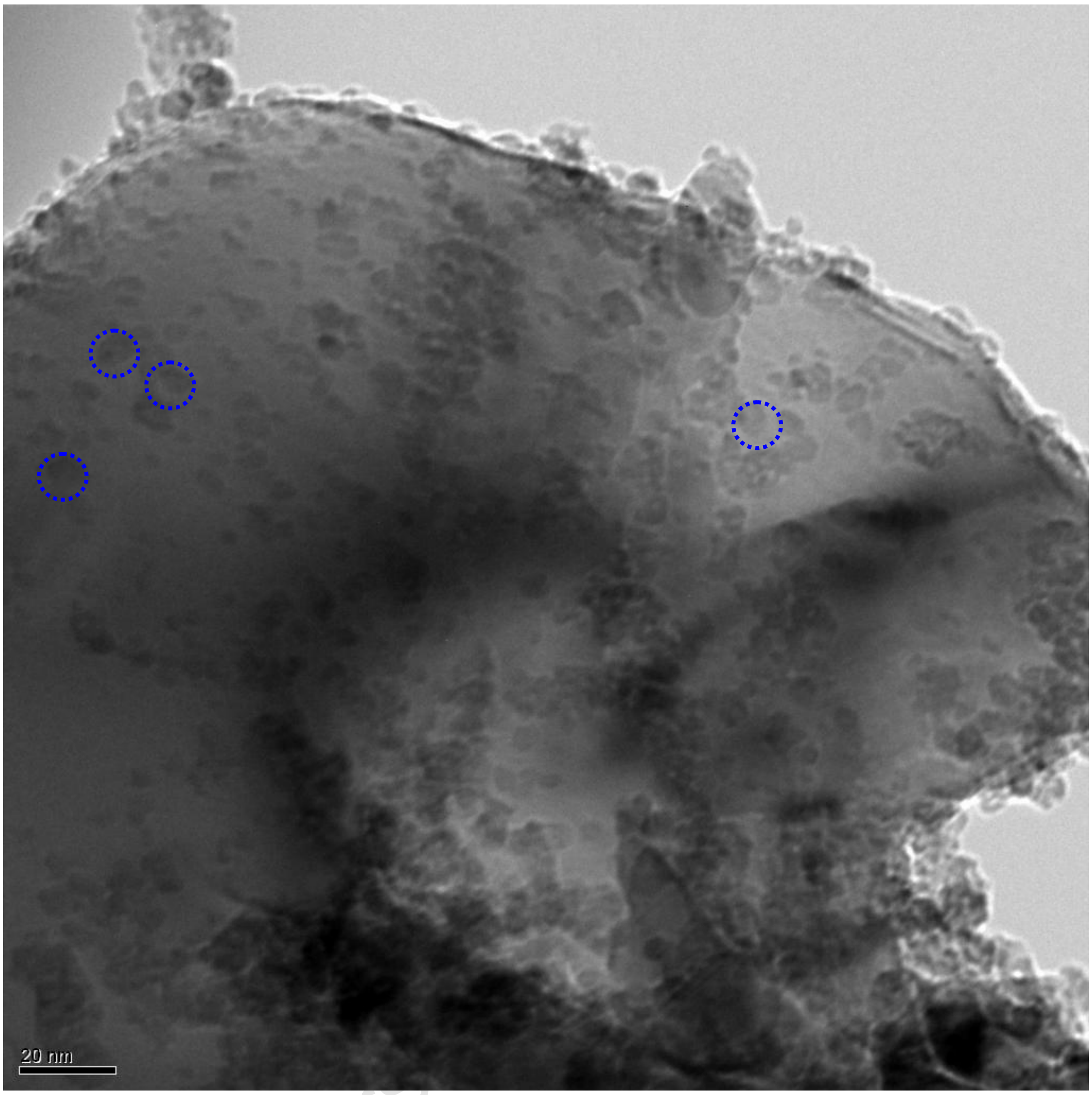

Figure 4.17: *TEM-image for the estimation of the crystallite size in the passivated model alumina supported cobalt catalyst after Experiment 4 (OROR catalyst)*

4.2.4.6 Experiment 5 (reduced model catalyst re-oxidised at high pressure)

Hollow sphere formation via the Kirkendall effect can also be observed in the samples oxidised at high pressure following a reduction step (see Figure 4.18). Measurements of the outer shell of the hollow sphere showed that the oxidation under pressure resulted in a smaller ring width than the oxidation at atmospheric pressure. An average shell diameter of 6.4 nm (± 1.5 nm) was determined in the high pressure oxidation, whereas the oxidation at atmospheric pressure yielded an average shell diameter of 9.0 nm (*vide supra*).

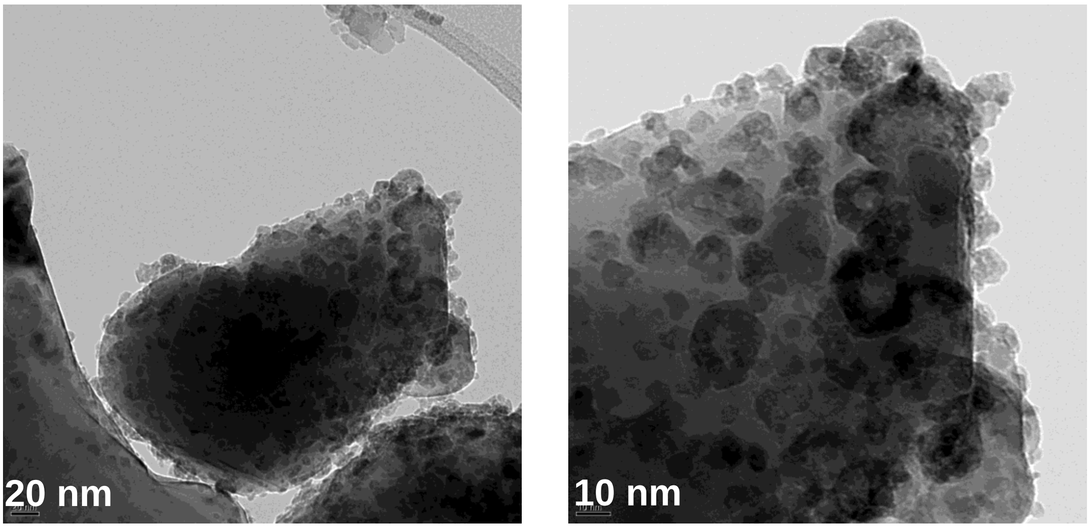

Figure 4.18: *Hollow sphere formation after high pressure oxidation in air at 10 bar gauge pressure of the reduced model catalyst (Experiment 5)*

4.2.5 H_2 chemisorption

Hydrogen chemisorption is a widely used method for characterisation of the surface of metal-supported particles. Metallic surface area and the dispersion of cobalt in the catalysts that were oxidised were determined with H_2 chemisorption. The sample was reduced prior the H_2 chemisorption analysis. Approximately 0.25 g of sample was degassed and then heated to 425°C at 2°C/min and kept at this temperature for 7 hours under a flow (100 ml (NTP)/min) of hydrogen.

The observed isotherms for hydrogen adsorption over the alumina supported model cobalt catalysts in the oxidised form (i.e. the freshly calcined model catalyst - *Experiment 1*, the re-oxidised, reduced model catalyst - *Experiment 3*, and the reduced model catalyst after re-oxidation at high pressure - *Experiment 5*) are shown in Figure 4.19. The isotherms are characterized by a strong hydrogen adsorption leading to rapid saturation at a relatively low hydrogen pressure followed by the uptake of hydrogen leading to weakly adsorbed species. The hydrogen chemisorption was modelled as a dual Langmuir-isotherm assuming the dissociative adsorption of hydrogen, in which the inhibition term in the second isotherm was neglected:

$$V_{H_2-\text{adsorbed}} = V_{m,1} \cdot \frac{K_1 \cdot p_{H_2}^{0.5}}{1 + K_1 \cdot p_{H_2}^{0.5}} + V_{m,2} \cdot K_2 \cdot p_{H_2}^{0.5}$$

The latter can be justified since the hydrogen uptake at high pressure does not seem to approach saturation. The modelling parameters required to describe the H_2-chemisorption are shown in Table 4.5.

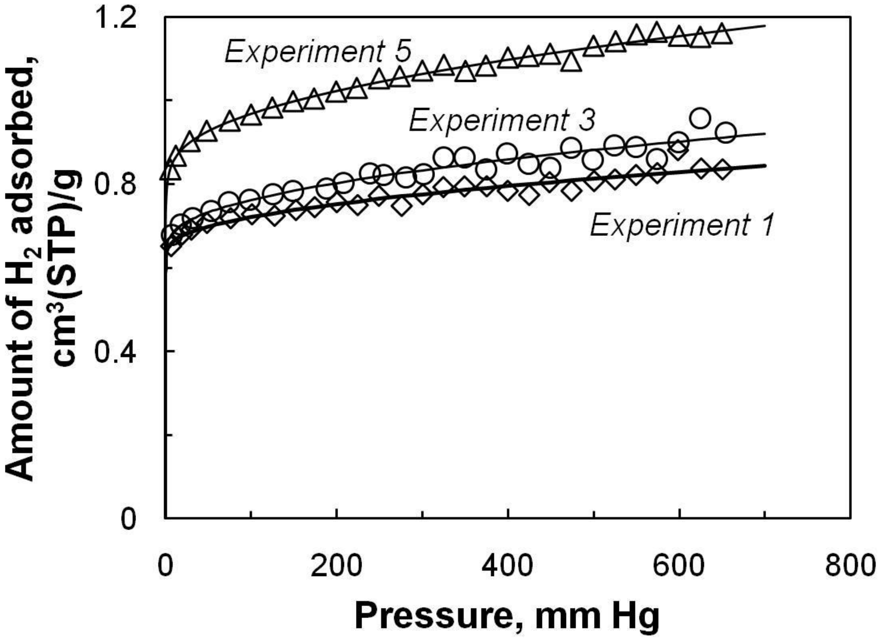

Figure 4.19: *Isotherms of the hydrogen uptake at 100°C on the alumina supported, model cobalt catalyst (all samples reduced prior to H_2-chemisorption at 425°C for 7 hrs)*
(solid lines represent model fits – see text)

Table 4.5: *Evaluation of the H_2-chemisorption on the model catalysts according to*

$$V_{H_2-\text{adsorbed}} = V_{m,1} \cdot \frac{K_1 \cdot p_{H_2}^{0.5}}{1 + K_1 \cdot p_{H_2}^{0.5}} + V_{m,2} \cdot K_2 \cdot p_{H_2}^{0.5}$$

(data indicated with 95% confidence interval)

Sample name	Oxidation / reduction steps	$V_{m,1}$ cm^3(STP)/g	K_1 mm Hg^{-1}	$V_{m,2} \cdot K_2$ $10^{-3} \cdot cm^3$(STP)/g
Exp 1	O	0.65 ± 0.04	19.3 ± 78.4	7.3 ± 1.5
Exp 3	ORO	0.67 ± 0.02	13.1 ± 24.1	9.4 ± 0.7
Exp 5	OR_HP O	0.86 ± 0.02	6.4 ± 3.8	12.3 ± 0.9

The amount of strongly adsorbed hydrogen to form a monolayer is approximately the same for the reduced calcined (*Experiment 1*) and the reduced, re-oxidised, reduced sample (*Experiment 3*). The reduction of the sample subjected to high pressure oxidation after reduction (*Experiment 5*), resulted in a significantly higher amount of hydrogen taken up to form a monolayer.

The adsorption constant for the formation of strongly adsorbed hydrogen does show a decrease for the re-oxidised, reduced samples, but no definite conclusion can be made due to the large uncertainty in the determination of the adsorption constant. More data points at lower hydrogen pressure (i.e. below 6 mm Hg) needs to be collected in order to obtain a greater confidence in the values obtained for the adsorption constant.

The second Langmuir isotherm is characterized by the product of the adsorption constant and the amount of hydrogen adsorbed to form a monolayer of the weakly adsorbed hydrogen. These parameters could not be resolved, since the second isotherm does not seem to approach saturation. The oxidation of the reduced model catalyst increases the value for the combined constant. This could imply that the strength of the weakly adsorbed hydrogen increases or the amount of weakly adsorbed hydrogen increases, or both.

4.2.5.1 Metal surface area

The active metal area is that portion of the total metal on the surface that is accessible to gases. The active metal area (m^2/g) can be estimated from the hydrogen chemisorption data assuming that all metal surface yields strongly adsorbed hydrogen. It is further assumed during these analyses that the site density for hcp-Co and fcc-Co is 14.6 atoms/nm^2. The metal surface area shows the same trend as the amount of hydrogen taken-up to form a monolayer, since it is directly derived from it without taking into account other physical characteristics of the sample.

Table 4.6: *Amount of hydrogen taken up to form a monolayer ($V_{m,1}$) in the H_2 chemisorption at 100^{o}C over the alumina supported, model cobalt catalysts subjected to the various treatments, and the calculated metal surface area (S_{Me}), dispersion (D) and cobalt crystallite size (d_{Co}) assuming 100% reduction*

Sample name	Oxidation / reduction steps	$V_{H2,mono}$ cm^3(STP)/g	S_{Me} m²/g	D %	d_{Co} nm
Exp 1	O	0.65	2.4	4.2	23.1
Exp 3	ORO	0.67	2.5	4.3	22.3
Exp 5	OR_HP O	0.86	3.2	5.5	17.5

4.2.5.2 Dispersion

The dispersion is the fraction of the total active metal loaded on the sample that is accessible to the reactant molecule, i.e. hydrogen. Therefore the total amount of metal added to the support during preparation must be known.

The dispersion calculated here is the number of metallic surface cobalt atoms relative to the total amount of cobalt present in the sample, irrespective of their oxidation state. The dispersion was determined using the cobalt loading determined by ICP analysis (see Table 4.1). ICP analyses showed that an 8.2 mass % cobalt loading was obtained although it was aim for an 10 mass % loading. A loading of 10 mass % versus an 8.2 mass % loading would result in a decrease of the cobalt dispersion of 18 %, i.e. instead of a dispersion of 4.4% a dispersion of 3.6% would be obtained.

4.2.5.3 Cobalt crystallite size

The active particle size can be estimated from hydrogen chemisorption data. It was assumed that the catalyst was fully reduced following the H_2-treatment prior to the chemisorption measurement. Furthermore, it was assumed that the particles were spherical or hemi-spherical shape. The particle diameter (d_{Co}) was calculated by dividing the volume of the reduced crystallites by the active area per gram of pure metal. The so calculated cobalt crystallite sizes are in the range of 17-22 nm.

4.2.6 Temperature programmed reduction (TPR)

TPR was performed to determine reduction profiles of the different calcined samples. The samples were dried *in-situ* at 120°C for 10 min in He (He-flow = 10 ml (STP)/min) prior the analyses. The mass of catalyst used varied between 0.1525 g to 0.1670 g. The samples were reduced in a 10% H_2/Ar gas mixture with a flow rate of 75 ml (STP)/min and a heating rate of 10°C/min.

The amount of hydrogen consumed during temperature programmed reduction is given in Table 4.7. The hydrogen consumption is normalized per mol of cobalt assuming a cobalt loading of 8.2 mass-% in the calcined catalyst (see Chapter 4.1). The obtained H_2/Co-ratios are less than would have been expected, if all cobalt is present as Co_3O_4. The amount of hydrogen consumed during the TPR-experiment is lower for the samples which have been subjected to an oxidation/reduction cycle. In particular, the reduction of the sample, which was oxidised at high pressure following the reduction, shows a significant lower consumption of hydrogen during the temperature programmed reduction.

Table 4.7: *Amount of hydrogen consumed during the temperature programmed reduction (TPR)*

Sample name	Oxidation / reduction steps	$H_{2,consumed}$ mmol/g_{cat}	H_2/Co mol/mol
Exp 1	O	1.70	1.22
Exp 3	ORO	1.66	1.19
Exp 5	OR_HP O	1.49	1.07

The temperature programmed reduction (TPR) profile of the 3 oxidised alumina supported, model cobalt catalysts, viz. *Experiment 1* (O), *Experiment 3* (ORO) and *Experiment 5* (OR_HPO) are shown in Figure 4.20, where the rate of hydrogen consumption (expressed in μmol H_2 per second per gram catalyst) is shown as a function of the temperature. The reduction of unsupported Co_3O_4 proceeds via two stages, viz. reduction of Co_3O_4 to CoO followed by the reduction of CoO to metallic cobalt, resulting in two distinct maxima in the rate of hydrogen consumption as a function of temperature [31,41,87]. The TPR-profile of the calcined model catalyst (*Experiment 1*) shows a shoulder in the region 160-200^{o}C, two peak maxima at 315 ^{o}C and 345^{o}C respectively followed by a shoulder at ca. 500^{o}C. The first peak maximum obtained in the TPR-profile of the calcined model catalyst is at a slightly higher temperature than that reported in literature for Co/α-Al_2O_3 [42] (i.e. 315^{o}C versus 295^{o}C reported in literature [42]). This might be attributed to a difference in the average crystallite size of Co_3O_4 (32.9 nm in the calcined model catalyst versus 18.2 nm in [42]).

The TPR-profiles of the re-oxidised, reduced samples do not show clearly a two step reduction for the reduction of Co_3O_4, although the central peak maximum seems to be surrounded by some shoulders.

In order to resolve these TPR-profiles better, the TPR profile was deconvoluted with a set of Gaussian peaks. A TPR-profile does not correspond exactly to a Gaussian curve, but it yields an indication about the number of reduction processes taking place and their magnitude. A minimum set of Gaussian curves was used, and it was fitted using a conjugate gradient method minimizing:

$$\sum \left| \left(r_{H_2,\text{measured}} \right) - \left(r_{H_2,\text{calculated}} \right) \right| = \text{minimum}$$

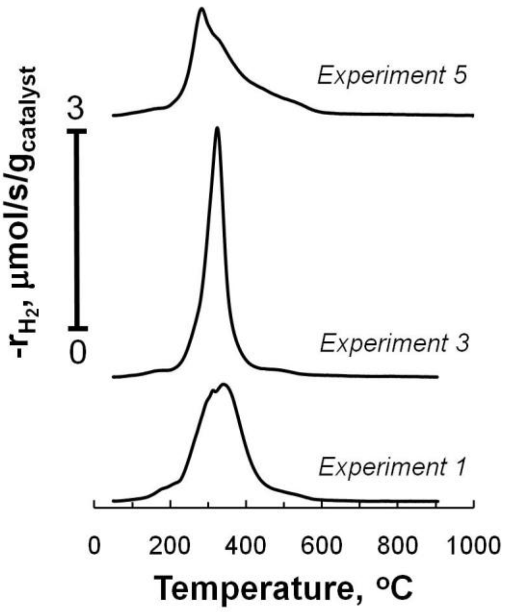

Figure 4.20: *TPR-profile of the calcined model catalyst (Experiment 1), the re-oxidised reduced model catalysts, with the re-oxidation step in air at atmospheric pressure (Experiment 3) and at 10 bar gauge pressure (Experiment 5)*

with

$$-r_{H_2,\mathrm{calculated}}(T) = \sum_i \frac{A_i}{\sqrt{2\pi \cdot \sigma_i^2}} \cdot e^{\frac{-(T - T_{\max,i})^2}{2 \cdot \sigma_i^2}}$$

where

$-r_{H_2,\mathrm{measured}}$	measured rate of hydrogen consumption as a function of temperature
$-r_{H_2,\mathrm{calculated}}$	calculated rate of hydrogen consumption as a function of temperature
i	number of Gaussian functions required to describe the TPR-profile
A_i	magnitude of the reduction process i
σ_I	'variance' of the Gaussian fit i
$T_{\max,i}$	temperature at which the rate of hydrogen consumption is maximum for the reduction process i

Figure 4.21 shows the obtained fits of the Gaussian curves to the experimentally determined TPR-profiles (included as well is the difference between the experimentally curve and the calculated curve). A set of 4 Gaussian curves was

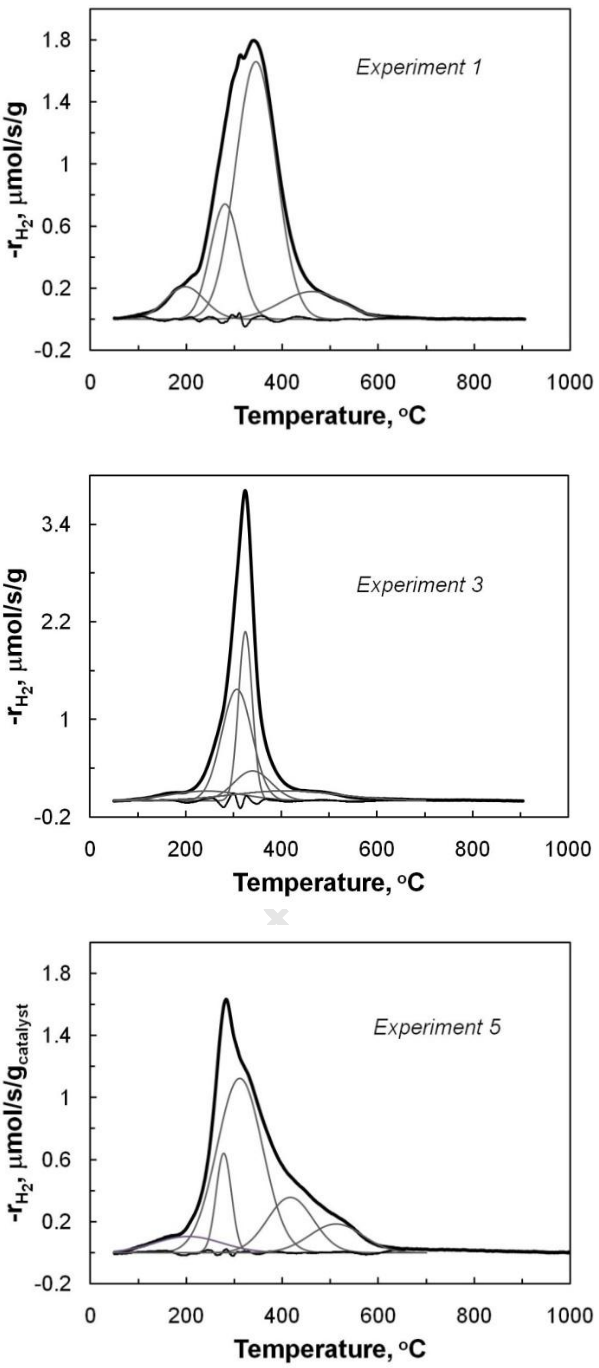

Figure 4.21: *Fitting of the experimental TPR-profiles to a set of Gaussian curves (Fat solid line: measured TPR-curve; gray curves: fitted Gaussian curves; thin solid line: difference between measured and the sum of the fitted curves)*

Top: *calcined model catalyst (Experiment 1)*

Middle: *re-oxidised reduced model catalysts, with the re-oxidation step in air at atmospheric pressure (Experiment 3)*

Top: *re-oxidised reduced model catalysts, with the re-oxidation step in air at 10 bar gauge pressure (Experiment 5)* needed to adequately describe the TPR-profile of the calcined model catalyst (*Experiment 1*), whereas a set of 5 Gaussian curves were required to obtain an adequate fitting of the experimental TPR-profiles of the re-oxidised, reduced model catalysts (*Experiment 3* and *Experiment 5*). The obtained fits for the experimental TPR-profiles of *Experiment 1* and *Experiment 5* to a set of Gaussian curves is very good, whereas the fit of the TPR profile of *Experiment 3* is adequate showing some difficulties in describing the main reduction peak using only 3 Gaussian curves (a better fit might have been expected by including an additional Gaussian curve).

The quantitative evaluation of the deconvoluted TPR-profiles is given in Table 4.8. All TPR-profiles are preceded by a shoulder in the temperature range 198-244°C. The amount of hydrogen consumed attributable to this cycle is approximately 8% of the total hydrogen consumption. This shoulder is typically ascribed to the reduction of residual cobalt nitrate [42]. However, the persistence of this peak after oxidation-reduction cycles makes this assignment doubtful, at least for the observed low temperature shoulder for *Experiment 3* and *Experiment 5*. This experiment should be repeated to clarify the origin of this shoulder. The outlet composition should be

Table 4.8: *Fitting parameters for the Gaussian curves to describe the experimentally obtained TPR-profiles*

		Experiment 1	***Experiment 3***	***Experiment 5***
1st peak	T_{max}, °C	198	244	204
	σ, °C	40	78	70
	A, $\mu mol\cdot{}^{o}C/g_{cat}/s$	0.2	0.1	0.1
	fraction of H_2-consumption[1]	8%	8%	7%
2nd peak	T_{max}, °C	281	307	278
	σ, °C	30	32	16
	A, $\mu mol\cdot{}^{o}C/g_{cat}/s$	0.7	1.4	0.6
	fraction of H_2-consumption[1]	20%	39%	10%
3rd peak	T_{max}, °C	345	325	312
	σ, °C	42	14	48
	A, $\mu mol\cdot{}^{o}C/g_{cat}/s$	1.7	2.1	1.1
	fraction of H_2-consumption[1]	62%	27%	54%
4th peak	T_{max}, °C	462	340	417
	σ, °C	65	40	47
	A, $\mu mol\cdot{}^{o}C/g_{cat}/s$	0.2	0.4	0.4
	fraction of H_2-consumption[1]	10 %	13 %	17%
5th peak	T_{max}, °C		409	512
	σ, °C		118	55
	A, $\mu mol\cdot{}^{o}C/g_{cat}/s$		0.1	0.2
	fraction of H_2-consumption[1]		13%	11%

[1] Fraction of the hydrogen consumption as determined from the area of the Gaussian curve relative to the sum of the areas of all Gaussian curves

monitored, e.g. by connecting to a mass spectrometer to verify whether nitrogen containing-species are being released and whether the hydrogen consumption is equalled by the water formation.

The hydrogen consumption in the range 280-400°C is typically ascribed to the two-step reduction of Co_3O_4 and the reduction of weakly bound CoO [42]. The temperature programmed reduction of the freshly calcined model catalyst, The hydrogen consumption attributed to the two peaks in this temperature region for *Experiment 1*, has a ratio of 1:3.1, which is in good agreement with the two-step reduction process of Co_3O_4 (which should be 1:3 for Co_3O_4). The hydrogen consumption in this temperature region for *Experiment 3* could only be described adequately by 3 Gaussian curves, with the first curve shifted towards a higher temperature in comparison to the TPR-curve obtained for *Experiment 1*. Hence, it is doubtful that the first Gaussian curve in this temperature range can be ascribed solely to the reduction of Co_3O_4 to CoO. The TPR-profile for *Experiment 5* in this temperature region was well described using 2 Gaussian curves with the first peak maximum at a similar temperature as found in the TPR profile for *Experiment 1* (i.e. 278 vs. 281°C). It might be argued that this Gaussian curve does represent the reduction of Co_3O_4 to CoO in the temperature programmed reduction for *Experiment 5* as well. The amount of hydrogen consumed for the first Gaussian curve in this temperature range for Experiment 5 in comparison to the second Gaussian curve is however much less than the expected ratio of 1:3 (a ratio of 1:5.3 is determined) implying that not only Co_3O_4 is reduced in this temperature range, but also divalent cobalt, e.g. weakly bound CoO. It can be further noted that the temperature at which the hydrogen consumption is maximum for the second Gaussian curve in this temperature range has shifted for *Experiment 5* to 312°C from 345°C for *Experiment 1* implying a more facile reduction of this type of cobalt present in the catalyst sample.

The reduction peaks and shoulders appearing at temperature range higher than 400°C are ascribed to cobalt species interacting more strongly with the alumina support [42]. These peaks are typically much broader than the Gaussian peaks describing the reduction of cobalt in the range 280-400°C. This may indicate that a single Gaussian curve actually describes a multitude of reduction processes, since the occurrence of a single reduction process with a maximum in the TPR at slightly higher temperatures is expected to be described with a slightly broader peak. The TPR-profile of *Experiment 1* shows a broad shoulder in the temperature range which can be described with a single Gaussian curve with a maximum at 462^{o}C. The amount of hydrogen consumed to reduce these cobalt species amounts to 10.4% of the total hydrogen consumption to reduce the catalyst sample from *Experiment 1*. The high temperature region (T>400^{o}C) in the TPR-profile for *Experiment 3* can be described by a very broad Gaussian curve with a maximum of 409^{o}C. This implies that this Gaussian curve describes the reduction of cobalt species ranging from 350-550^{o}C. Hence, conclusions regarding the type of species attributable to this Gaussian curve cannot be made. The high temperature region (T>400^{o}C) in the TPR-profile for *Experiment 5* can be described by two Gaussian curves with variances slightly larger than the variances obtained in the region 280-400^{o}C. The maxima of the Gaussian curves with a maximum at a temperature larger than 400^{o}C are at 409 ^{o}C and 515^{o}C respectively. The amount of hydrogen attributable to each of the Gaussian curves is 17.4% and 10.6% of the total hydrogen consumption respectively. A comparison with the TPR-profile of *Experiment 1* shows that the highest peak maximum is shifted towards higher reduction temperatures. It might be concluded that the additional reduction-oxidation cycle (and in particular the high pressure oxidation) resulted in a stronger interaction of some of the cobalt with alumina resulting in a shift in the high-temperature reduction temperature towards higher temperatures.

4.3 Catalyst testing in a fixed bed reactor

Three catalysts, i.e. *Experiment 1*(O), *Experiment 3* (ORO) and *Experiment 5* (OR_HP O), were tested for activity and methane selectivity in the Fischer-Tropsch synthesis in a fixed bed reactor system. These samples were reduced in pure hydrogen at 425°C at for 6 hours and a space velocity of 2100 ml (STP) H_2/hr/$g_{catalyst}$ prior to the Fischer-Tropsch synthesis.

4.3.1 CO conversion as a function of time on line

Figure 4.22 shows the CO-conversion as a function of time on line. The reaction was started at a constant space velocity of 0.134 mmol CO/s/$g_{catalyst}$. After ca. 1.5 days on line the space velocity was adjusted by changing the gas velocity to achieve a CO-conversion of ca. 10%. It seems that after 1 day on line the freshly calcined catalyst sample is more active than the catalyst sample, which underwent reduction and subsequent re-oxidation as evidenced by the higher conversion level obtained (although this result should be taken with caution at this stage seeing that the levels of conversion are quite low).

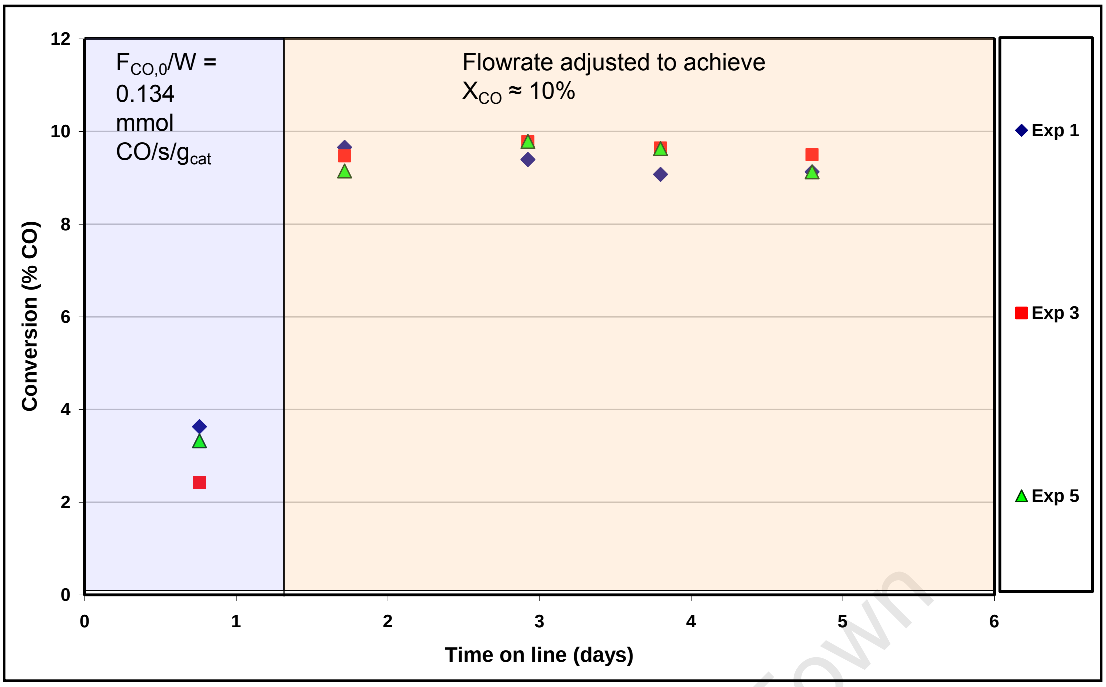

Figure 4.22: *CO conversion during Fischer-Tropsch synthesis with Experiment 1, Experiment 3 and Experiment 5*

The adjustment of the synthesis gas flow rate did result in CO-conversions of ca. 10%, and the catalytic activity of the samples can now be compared based on the flow rate used to achieve this conversion level.

4.3.2 Rate of the Fischer-Tropsch synthesis

The rate of the Fischer-Tropsch synthesis was determined from the flow rate of CO and the CO-conversion. This corresponds to an integral rate of the Fischer-Tropsch synthesis. However, the conversion levels were kept low on purpose (differential reactor) so that it corresponds roughly to the rate of reaction at the inlet partial pressures of CO and H_2. The rate of the Fischer-Tropsch synthesis is now a direct measure of catalyst activity towards the Fischer-Tropsch reaction.

Figure 4.23 shows the rate of the Fischer-Tropsch synthesis in mol of CO converted per second and mass of catalyst as a function of time on line. The FT activity of *Experiment 1*(O) and *Experiment 5* (OR_HP O) were very similar with *Experiment 3* (ORO) showing a lower activity per gram of catalyst.

The activity of all three catalysts seems to decline with time on line. However, it should be kept in mind that the first data point was recorded at a low conversion level of CO resulting in a higher uncertainty in the actual value of the rate at that time.

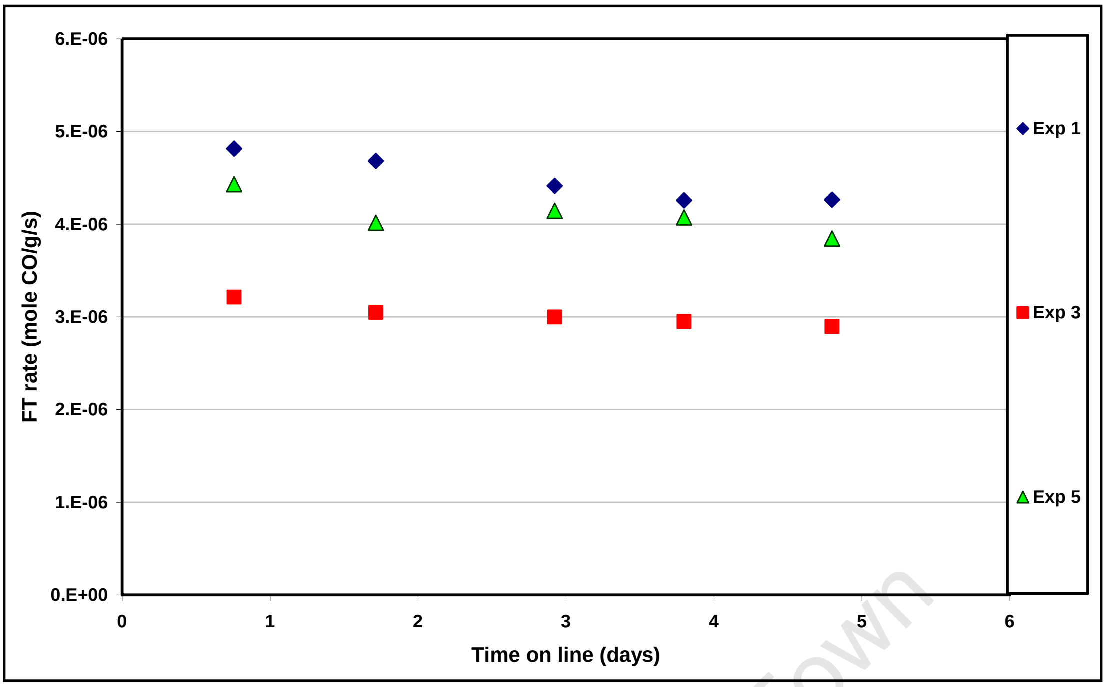

Figure 4.23: *Rate of the Fischer-Tropsch synthesis as a function of time on line for Experiment 1, Experiment 3 and Experiment 5*

Omitting the rate obtained after 1 day on line from the deactivation analysis, it can be concluded that the activity of the freshly calcined catalyst sample (*Experiment 1*) shows a steady decline in activity with time on line (between 1.7 days on line and 4.8 days on line the catalyst sample lost 9% of its catalytic activity). In a similar manner, the catalyst activity of the other samples after 4.8 days on line can be compared to the catalyst activity after 1.7 days on line. The catalyst activity of the re-oxidised, reduced sample (*Experiment 3*) was reduced in this time interval by 5%, and the catalyst activity of the reduced sample, which was re-oxidised at high pressure, was reduced in this time interval by 4%.

4.3.2.1 Investigating the reproducibility of the Fischer-Tropsch synthesis rate data

A repeat run was performed with the freshly calcined catalyst (*Experiment 1*) with the oxidised, reduced sample (*Experiment 3*). The freshly calcined catalyst was, however started up with a higher space velocity of 0.168 mmol CO/s/$g_{catalyst}$ before adjusting the flows to achieve a conversion level of CO of ca. 10%. The oxidised, reduced catalyst sample was started up at a lower space velocity of 0.054 mmol CO/s/$g_{catalyst}$ before adjusting the space velocity to achieve a conversion level of CO of ca. 10%. The repeated FT runs were labelled as *Experiment 1_b* and *Experiment 3_b*, respectively. Figure 4.24 shows the rate of the Fischer-Tropsch synthesis (in mole of

CO converted per second and gram of catalyst) as a function of time on line. It can be seen that *Experiment 3_b* and *Experiment 3* were similar, but the repeat run of *Experiment 1* (*Experiment 1_b*) resulted in a much lower activity. The catalyst activity seems to drop sharply going from on 1 day on line to 2 days on line. This might be attributed to a high, initial deactivation rate. However, it should be kept in mind that the initial data was obtained with a high synthesis gas flow rate and a low CO conversion resulting in an uncertainty regarding this data point. At this stage the low activity obtained in *Experiment 1_b* cannot be explained and further investigations are required.

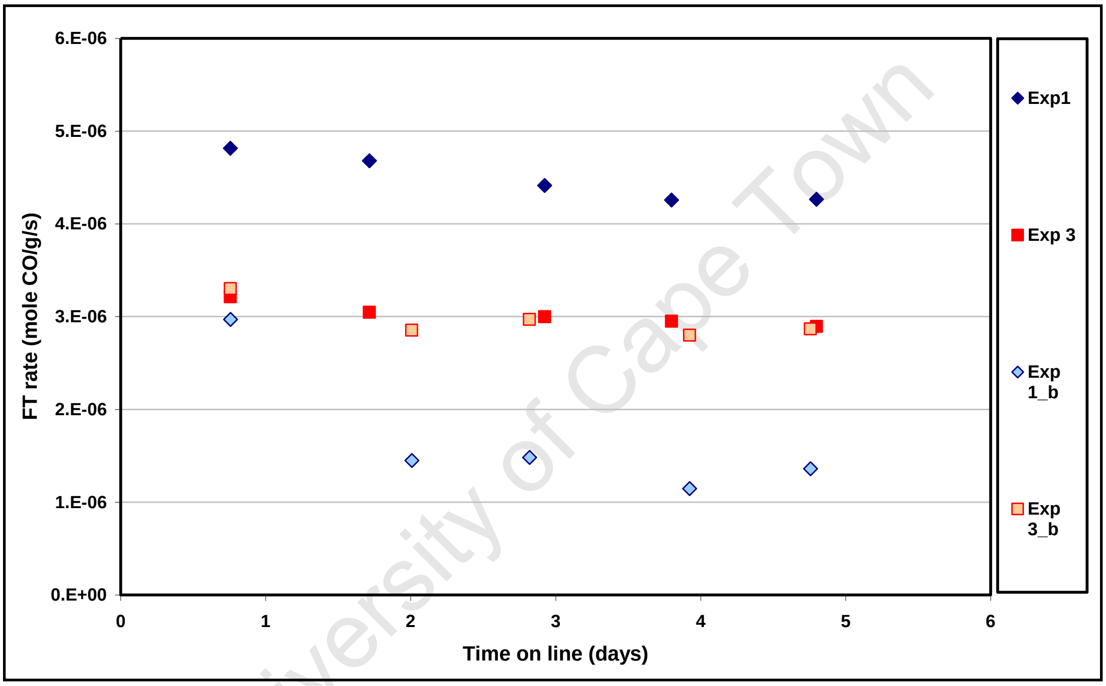

Figure 4.24: *Repeatability of the Fischer-Tropsch synthesis with Experiment 1, and Experiment 3*

4.3.3 Methane selectivity

As a measure of the selectivity of the catalyst, the methane selectivity in C-% was determined as a function of time on line (see Figure 4.25). The methane selectivity was only recorded when the CO conversion is ca. 10%. The methane selectivity of the freshly calcined catalyst (*Experiment 1*) is slightly higher than that obtained with the other catalyst samples (*Experiment 3* and *Experiment 5*). All catalyst samples seem to reach a relatively high methane selectivity of ca. 16 C-% independent of the catalyst sample. In the repeat run, *Experiment 1_b*, a similar methane selectivity was obtained, whereas in *Experiment 3_b* a slightly lower methane selectivity was obtained. However, it should be noted that the methane selectivity is in a narrow band and that the variations are small.

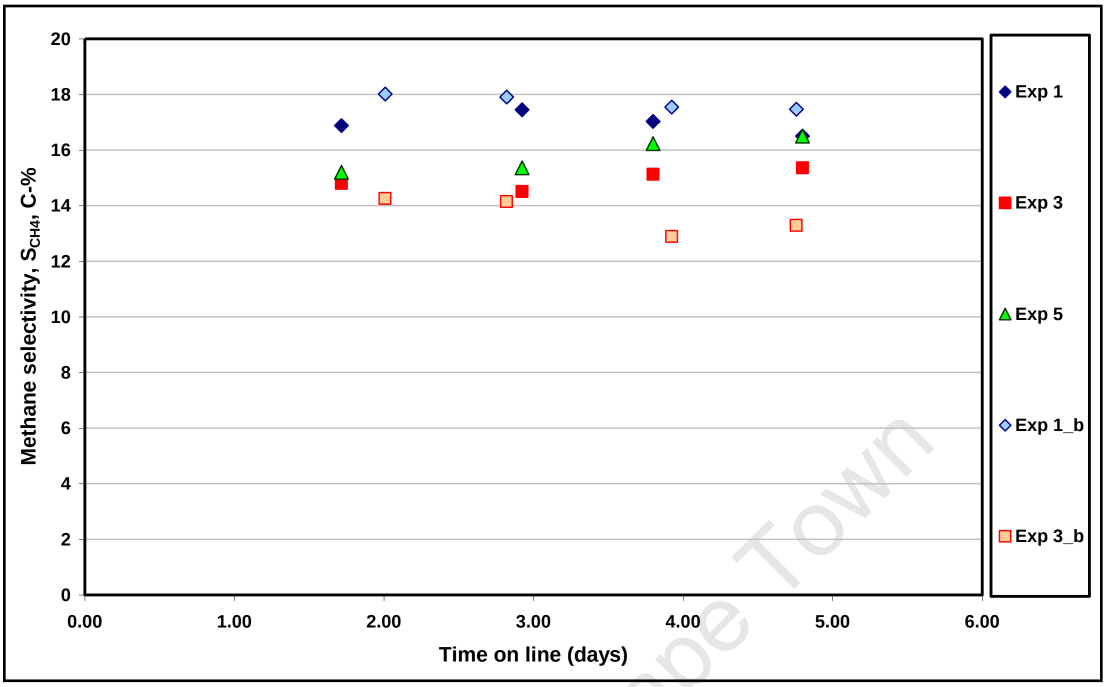

Figure 4.25: *Methane selectivity in the Fischer-Tropsch synthesis over the model catalysts after Experiment1, Experiment 3 and Experiment 5*

CHAPTER 5

DISCUSSION

5.1 Catalyst characterization

A variety of techniques was applied to characterize the treatment of the model catalyst, $Co/\alpha\text{-}Al_2O_3$. The studied treatment of the catalyst comprises of the oxidised (or freshly calcined) catalyst (*Experiment 1*), the reduced catalyst (*Experiment 2*), the re-oxidised reduced catalyst (*Experiment 3*), the reduced, re-oxidised, reduced catalyst (*Experiment 4*), and the re-oxidised reduced catalyst, which was re-oxidised at elevated pressure (*Experiment 5*). The various characterization techniques should yield information regarding similar properties of the catalyst.

5.1.1 Cobalt loading

Several characterization techniques can yield information regarding the cobalt loading on the prepared catalyst, i.e. ICP, *ex-situ* and *in-situ* XRD. The cobalt catalyst was either in an oxidised or reduced state prior to applying the characterization technique depending on the experimental environment it was exposed. To reduce the influence of the different phases and to prevent influences of the calcined mass on the determination of the cobalt loading, the results are presented as mass cobalt per gram $\alpha\text{-}Al_2O_3$. These calculated values of the mass cobalt metal per mass $\alpha\text{-}Al_2O_3$ support are compared in Table 5.1.

The cobalt loading obtained with *in-situ* XRD correlates well with the result obtained with AAS-ICP, despite the relatively large spread in values. The relatively lower cobalt mass relative to the mass of $\alpha\text{-}Al_2O_3$ calculated from the *ex-situ* XRD data of the oxidised samples is probably due to the presence of XRD-invisible cobalt oxide crystallites (the very low cobalt content determined by *ex-situ* XRD is probably due to the passivation procedure used, which may have resulted in the formation of XRD-invisible cobalt phases).

The amount of hydrogen consumed in the temperature programmed reduction of the oxidised sample (Experiment 1) shows a good correlation with with the ICP and the *in-situ* XRD measurement, if cobalt is predominantly present as Co_3O_4.

Table 5.1: *Mass cobalt (g) per mass α-Al_2O_3 (g) determined by ICP, ex-situ XRD and in-situ XRD*

Analyses	**Mass cobalt per gram α-Al_2O_3**
ICP	0.096
in-situ XRD	0.097 +/- 0.014
ex-situ XRD[1]	0.071+/- 0.003

[1] Cobalt content in oxidised samples

In general, the results indicate that the cobalt loading corresponds to 0.095 ± 0.014 g Co/g α-Al_2O_3 (or 8.5 ± 1.1 wt.-% Co in the calcined catalyst corresponding to 11.6 ± 1.5 wt.-% Co_3O_4 in the calcined catalyst or 8.8 ± 1.1 wt.-% Co in the reduced catalyst). The catalyst synthesis method was aimed to achieve 0.11 g Co/g α-Al_2O_3 by assuming that cobalt nitrate was present as $Co(NO_3)_2.6H_2O$, and that α-Al_2O_3 was completely dry after drying at 120°C. The discrepancy can be explained by either assuming that cobalt nitrate contained more water (8.5 mol of water per mol of cobalt instead of 6), or that the catalyst is hygroscopic and water is associated with the catalyst sample submitted for ICP-analysis. The latter explanation may be correct seeing that the repeat ICP-analysis, which was performed a few months later, yielded a lower cobalt content. This would imply that the cobalt loading determined by XRD underestimates the cobalt content due to the presence of XRD-invisible cobalt species. Hence, future work must ensure that the cobalt catalyst is stored under controlled conditions ensuring a constant water content of the calcined catalyst.

5.1.2 Metallic cobalt phases in reduced catalyst samples

Both hexagonal closed packed (hcp) cobalt and face centred cubic (fcc) cobalt were detected by *in-situ* XRD in the reduced catalyst samples. According to Khodakov et al. [23] both fcc-Co and hcp-Co were detected in cobalt supported on a silica catalyst, but that the reduction of Co_3O_4 on zirconia and alumina led to predominantly fcc-Co. Ghampson et al. [93] also observed both fcc-Co and hcp-Co in reduced cobalt-based Fischer-Tropsch catalysts supported on siliceous support materials. They observed that the crystallite size of hcp-Co remained small and constant, but that the crystallite size of fcc-Co decreased with decreasing support diameter, e.g. on MCM-41 and SBA-15.

The amount of hcp-Co relative to the amount of fcc-Co was higher after the second reduction step of the *in-situ* XRD experiment, i.e. the percentage of hcp-Co increased from 55 mass-% to 67 mass-%, and the amount of fcc-Co decreased from 45 mass-

% to 32 mass-% and the Co hcp increased from 55 mass % to 67 % (see Table 4.2). Face centred cubic (fcc) cobalt should be the preferred phase at the final reduction temperature of 425°C as bulk cobalt metal undergoes a martensitic formation from hcp-Co to fcc-Co when heated to 425°C [94]. Ghampson et al. [93] postulated that the hcp-Co could form during heating up to the transition temperature during reduction and then remain as hcp-Co because it is stabilised by their environment. The transition of hcp-Co to fcc-Co is known to be kinetically limited and temperatures as high as 800^{o}C might be required to achieve this transition [95].

Table 5.2: *Relative abundances of crystalline phases (% m/m) of reduced in-situ samples*

Sample name	**Oxidation / reduction steps**	**Co(fcc)**	**Co(hcp)**	Total
in-situ reduction step 1	OR	3.8 (45%)	4.6 (55%)	8.4
in-situ reduction step 2	OROR	2.6 (32%)	5.3 (67%)	7.9

5.1.3 Crystallite size as determined by XRD and TEM

5.1.3.1 Average crystallite size of Co_3O_4

Figure 5.1 shows the Co_3O_4 crystallite sizes measured during *ex-situ* XRD and *in-situ* XRD. In general the measurements correlate well. The crystallite size of Co_3O_4 of the freshly calcined catalyst is estimated to be ca. 33 nm. The oxidation of the reduced catalyst sample leads to a significant reduction in the average crystallite size and a value of 8.9 nm is estimated using *ex-situ* XRD and 9.3 nm using *in-situ* XRD. The only difference between the crystallite size determination using *ex-situ* XRD and *in-situ* XRD can be observed in the last oxidation step.

The third oxidation step yielded similar crystallite sizes of Co_3O_4, when the sample was oxidised at low pressure (as in the *in-situ* XRD experiment).

A smaller average crystallite size of Co_3O_4 was obtained using *ex-situ* XRD. However, it should be noticed that this sample was exposed to oxidation at 10 bar. Hence, it must be concluded that the high-pressure oxidation resulted in the formation of even smaller Co_3O_4 crystallites.

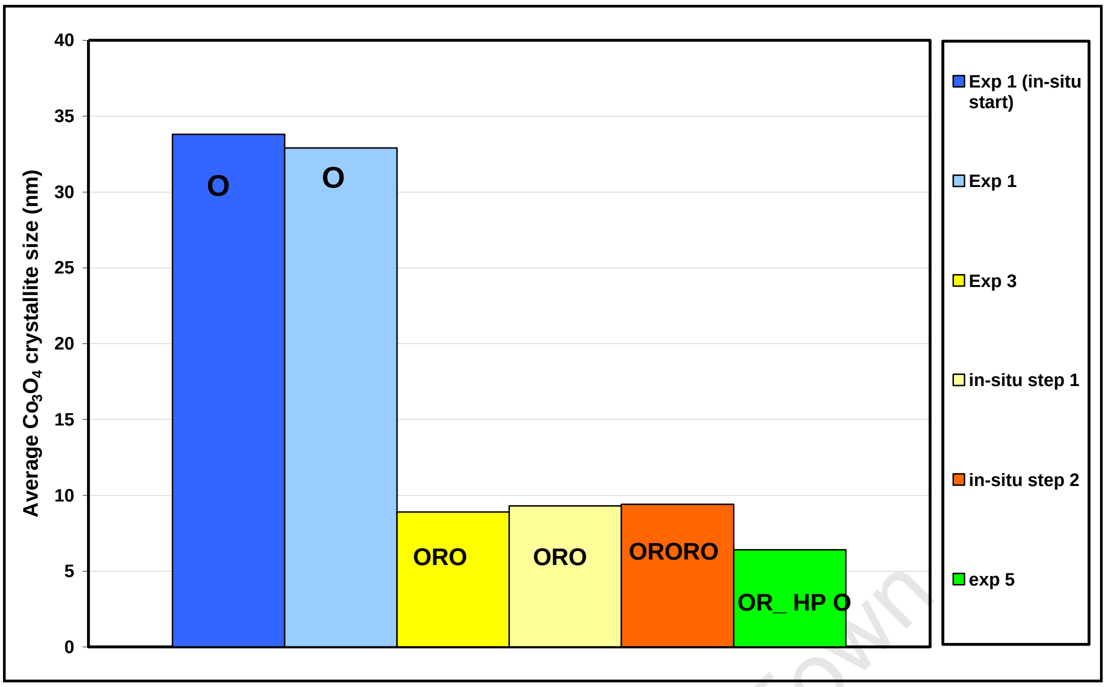

Figure 5.1: *Crystallite sizes of Co_3O_4 after the various oxidation steps: ex-situ and in-situ XRD data*

The formation of “smaller” Co_3O_4 crystallite size upon high pressure oxidation can be rationalized based on the TEM-measurements. In *Experiment 1* (O) the diameter of a solid crystallite is measured (see Figure 4.9), but with *Experiment 3* and *Experiment 5* (see Figure 4.11 and Figure 4.15) only crystalline domains in the shell of the hollow sphere is measured. This hollow sphere formation is clearly visible with TEM. Measurements of the shell of the hollow sphere (TEM images) showed that the oxidation under pressure, *Experiment 5*, resulted in a smaller shell width than *Experiment 3* that was conducted at atmospheric pressure. A shell width of 6.4 nm (± 1.5 nm) was measured in *Experiment 5* and a shell width of 9 nm (± 2.8 nm) is measured in *Experiment 3*. The difference in the thickness of the Co_3O_4 shell surrounding the hollow sphere during the high-pressure oxidation and atmospheric oxidation is illustrated in Figure 5.2. The presence of a thinner shell following the oxidation at high pressure in comparison to the shell following the oxidation at atmospheric pressure can be explained by a higher outward rate of diffusion of the cobalt than with the diffusion of cobalt during the oxidation at atmospheric pressure. Differences in the size of the hollow spheres with and without oxidation at high pressure are difficult to observe due to the large range in sizes of the Co_3O_4 hollow spheres observed in the TEM images.

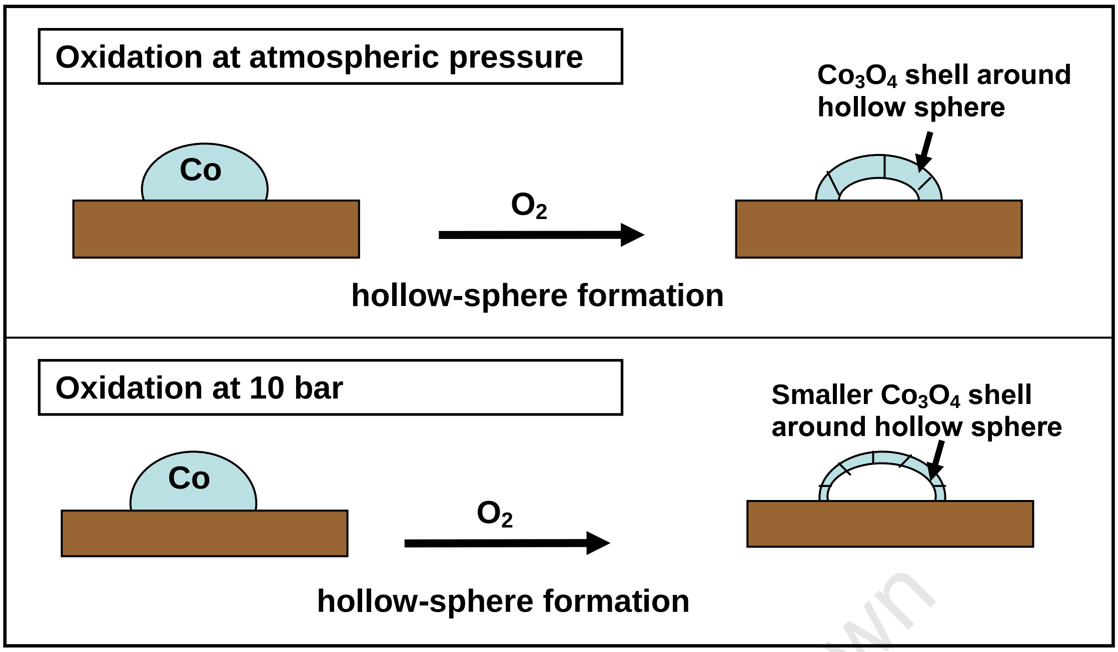

Figure 5.2: *Illustration of the formation of Co_3O_4 via the Kirkendall effect at atmospheric pressure and at 10 bar*

5.1.3.2 Average crystallite size of metallic cobalt

Both fcc-Co and hcp-Co were detected with *ex-situ* XRD of the reduced catalyst sample (*Experiment 2*). After the second reduction (*Experiment 4*) no cobalt metal was detected using *ex-situ* XRD possible due to the passivation step with dry ice.

Both fcc-Co and hcp-Co were detected during and after the reduction steps of the *in-situ* XRD. The crystallite size of the most abundant hcp-Co was determined to be only ca. 5 nm, whereas fcc-Co was present as larger crystallites ranging from 15 nm to 19 nm. Kitakami et al. [96] found that there is a close relationship between the particle size and the crystal phase. They calculated that fcc-Co polymorphs smaller than 100 nm are more stable than hcp-Co. The hexagonal closed packed (hcp) Co phase becomes more dominant with an increase in particle diameter. Hence, fcc-Co phase was expected to be the dominant phase in these samples, since smaller crystallites favour the face centred cubic structure. Ghampson et al. [93] also observed very small crystallites of hcp-Co, as indicated by rather broad diffraction peak in the *in-situ* XRD diffractogram. This unusual observation of small cobalt crystallites being present as hcp-Co might be explained by preferential formation of hcp-Co upon reduction of small Co_3O_4 crystallites and a kinetically hindered transformation of hcp-Co to fcc-Co [95].

The crystallite sizes estimated from a TEM-image of *Experiment 2* were 10.6, 15.4, 13.8 and 9.0 nm. The estimated crystallite sizes of cobalt crystallites of *Experiment 4* were 2.8, 3.4, 3.1 and 3.3 nm. Comparison of the TEM images between these two experiments gives the impression that the metal crystallite sizes are bigger after *Experiment 2* than *Experiment 4*. This may imply that smaller crystallites are obtained after reduction when a sample was oxidised for a second time and cobalt oxide is present as small crystallites in a shell surrounding a hollow sphere. This is illustrated in Figure 5.3 where an oxide layer of 2 nm is visible after *Experiment 2* that can be explained with the Cabrera-Mott theory [76]. It is also clearly visible from these images that a small cobalt metal crystallite particles can be observed after *Experiment 4*, some of these particles are smaller than 5 nm.

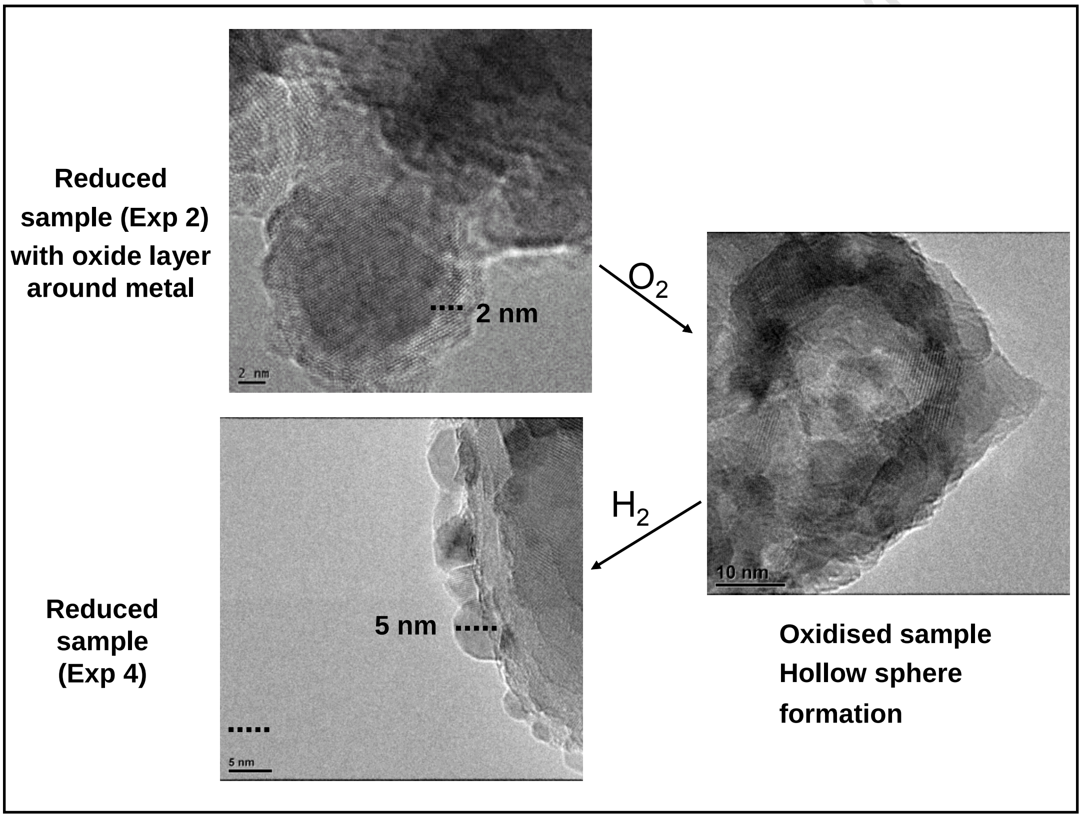

Figure 5.3: *Illustration of the formation of small metal particles after hollow sphere formation*

The difference in the crystallite size determined by XRD and by TEM can be ascribed to the presence of small crystallites, which are too small for detection by XRD (the lower size limit in crystallite size determination using XRD is ca. 3-5 nm depending on the noise level).

5.1.4 Cobalt metal surface area determined by H_2 chemisorption and *in-situ* XRD

The analysis of the H_2-chemisorption analysis in terms of available metal surface area involves a few assumptions, viz. hydrogen chemisorbs dissociatively, the uptake of hydrogen to form a monolayer is given by the intercept of the H_2-isotherm (i.e. the observed increase in hydrogen uptake with increasing hydrogen pressure at hydrogen pressures larger than 100 mm Hg is solely due to the uptake by the support and possible residual cobalt oxide), and the number of metallic cobalt atoms per unit surface area is 14.6 Co atoms per nm^2 and is independent of the phase and cobalt crystallite size. The active-site number is then only influenced by the Co particle size, loading amount and degree of reduction [40,97].

No difference was observed between the estimated metal surface area obtained after reduction of the oxidised catalyst sample (*Experiment 1*) and the re-oxidised, reduced catalyst sample (*Experiment 3*). It could have been expected that due to hollow sphere formation that resulted in small reduced particles (as been observed with TEM) that the measured surface area of *Experiment 1* and *Experiment 3* would differ more. H_2 chemisorption results showed that a higher cobalt metal surface area was obtained with high-pressure oxidation.

Based on the determined metallic cobalt crystallite size and the mass fraction of the two metallic cobalt phases determined from *in-situ* XRD, a cobalt metal surface area was calculated. After the first and the second reduction step the metallic cobalt surface area was estimated to be ca. 9.6 $m^2/g_{calcined\ sample}$ based on the *in-situ* XRD measurement. This value is much higher than the value obtained with H_2-chemisorption (2.5-2.6 m^2/g). These calculations assume that all the metal is detected by XRD and that all the metallic cobalt crystallites are accessible to hydrogen for chemisorption, i.e. the metal crystallite is not covered by an oxide over layer. It has already been mentioned that not all metal crystallites are determined by XRD as evidenced from the TEM-images. The low metal surface area measured from H_2-chemisorption may imply that not all metal surface area is accessible to hydrogen.

5.1.5 Reduction of the cobalt determined by TPR and XRD

TPR analyses were done to determine reduction profiles of the different calcined samples. The reactions taking place during the reduction of cobalt(III,II)oxide are:

$$Co_3O_4 + H_2 \rightarrow 3CoO + H_2O$$
$$CoO + H_2 \rightarrow Co + H_2O$$

This reduction process would imply a H_2/Co ratio of 1.33 mol/mol, which was not observed experimentally. The H_2-consumption for the reduction of the freshly calcined catalyst amounted to 1.22 mol/mol, which was further reduced for the oxidised, reduced samples. This would imply that 66% of the cobalt was not present as Co_3O_4. Alternatively, the sample is not completely reduced after the TPR-experiment, but no indications were obtained on the existence of cobalt aluminate type of species, which typically reduce at temperatures around 800-900^oC [31]. The amount of hydrogen consumed during the TPR-experiment was even lower for the catalysts which were previously reduced and re-oxidised. This may imply an even lower amount of cobalt present as Co_3O_4, which is not uniequivocally supported by the ex-situ XRD data, or an incomplete reduction of cobalt in these samples.

Distinct reduction peaks attributable to the consecutive reduction of Co_3O_4 to CoO to metallic cobalt were not observed during the temperature programmed reduction using 10% H_2 in N_2. The reduction steps could only be resolved for *Experiment 1* using Gaussian deconvolution of the TPR-profile. However, the consecutive reaction could be clearly discerned with *in-situ* XRD where 100 % hydrogen was used. The reason for the poor resolution of the TPR-profiles in comparison to the *in-situ* XRD experiment might be attributed to a faster heating rate and lower hydrogen partial pressure used during temperature programmed reduction in comparison to the *in-situ* XRD experiment.

The reduction temperature of *Experiment 3* (ORO) and *Experiment 5* was lower than reduction temperature of *Experiment 1*. *Experiment 5* showed a larger, broader peak from 400°C to 600°C than in *Experiment 1* and *Experiment 3*. According to literature a high reduction peak around 500 - 600°C is due to the reduction of highly dispersed cobalt oxide (CoO) particles strongly interacting with the support [42]. These species are most likely not observable with XRD (and thereby resulting in a lower cobalt visibility in the sample).

The reduction of the second step is strongly influenced by the crystallite size with the smaller crystallite size below 6 nm being more difficult to reduce than larger crystallites of 20 – 70 nm. High reduction temperatures are required if there is a strong interaction between the support and cobalt [31].

Reduction during *in-situ* XRD showed the formation of phases of Co_3O_4 to CoO to Co metal. The on-set of the reduction process (i.e. the start of the reduction of Co_3O_4 to CoO) started with the re-oxidised sample that was previously reduced, at a lower temperature than observed for the reduction of the calcined catalyst sample. Not only the on-set of the reduction of the re-oxidised sample start at a lower temperature, but also the whole reduction process occurred at a lower temperature. This can be observed by the completion of the conversion of CoO to the metal phase. No CoO was observed from ca. 340ºC onwards during reduction of the first step of the *in-situ*-XRD (equals to reduction of *Experiment 1*) in comparison with a lower reduction temperature of the second reduction (equals to reduction of *Experiment 3*) where from ca. 260ºC onwards no CoO was observed.

TPR and *in-situ* XRD results showed that after hollow sphere formation (as observed by TEM) the cobalt-supported catalyst reduced at a lower temperature. It is probably due to a larger surface available because of the crystallites forming part of the hollow sphere leading to more Co_3O_4 sites becoming accessible to the hydrogen. The top part of the hollow sphere also shows less metal support interaction that makes reduction easier. This reduction process is illustrated in Figure 5.4.

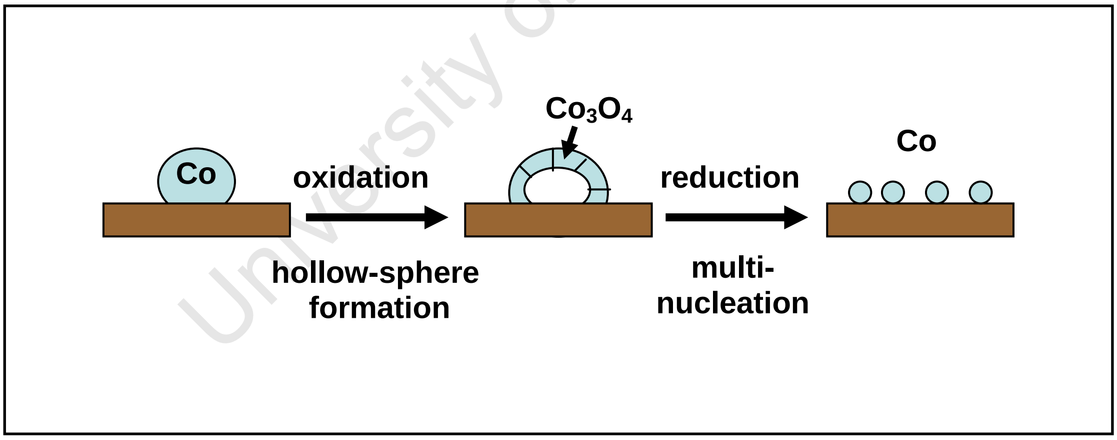

Figure 5.4: *Schematic of reduction of cobalt after hollow sphere formation*

5.2 Effect of OROR on catalyst performance

The activity for the Fischer-Tropsch synthesis per unit mass of catalyst sample of the catalyst samples after *Experiment 1*(O) and *Experiment 5* (OR_HP O) were very similar with *Experiment 3* (ORO) showing a lower activity per gram of catalyst.

The activity of catalyst is thought to be proportional to the metal catalyst surface area [24], except for cobalt crystallites less than 6 nm in size [25,26]. Hence, the rate per unit surface area is of interest. If the surface rate of CO consumption is calculated with the surface area, as determined with H_2 chemisorption it seems as if *Experiment 1* resulted in the most active catalyst and that *Experiment 3* and *Experiment 5* are very similar in activity (see Figure 5.5). The reduced catalytic activity per unit surface area of the model catalysts subjected to an oxidation step after the reduction step might be attributed to a reduced intrinsic rate due to the presence of small cobalt crystallites [25,26] or due to a reduced accessibility of the catalytically active sites.

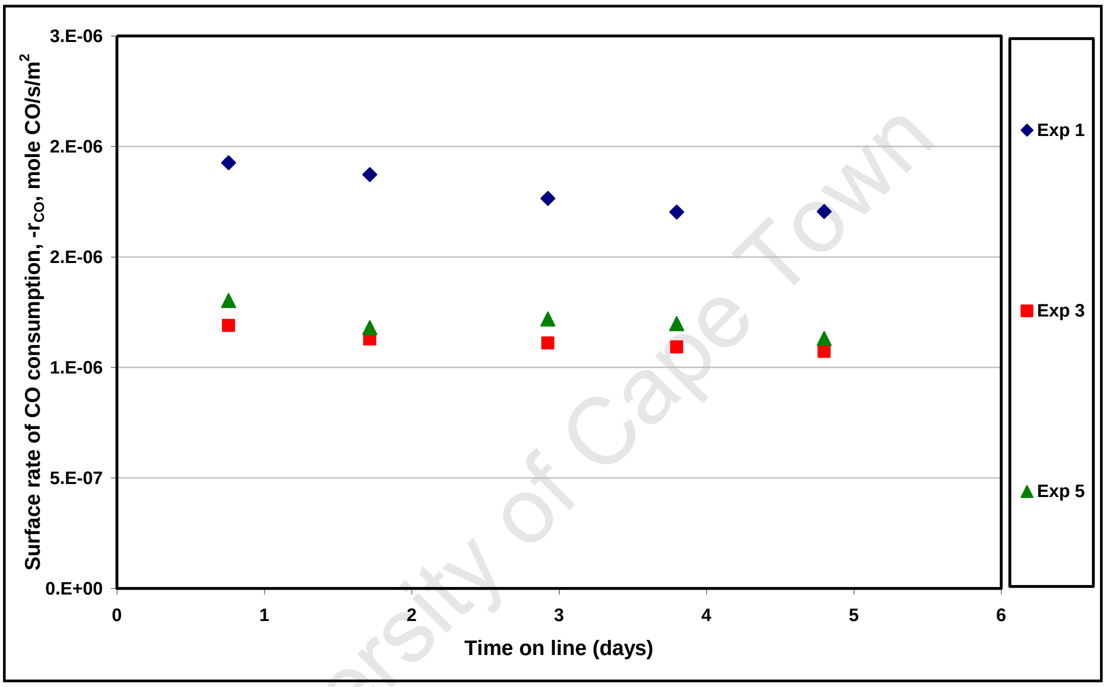

Figure 5.5: *Surface rate of CO consumption of Experiment1, Experiment 3 and Experiment 5 as function of time on line*

CHAPTER 6

CONCLUSIONS AND RECOMMENDATIONS

The aim of this study was to investigate how re-dispersion occurred during consecutive oxidation-reduction steps (OROR) of a supported-cobalt catalyst. These steps may mimic the regeneration process of a spent supported-cobalt Fischer Tropsch synthesis catalyst that consists of an oxidation step followed by a reduction step. For this study, a simplified supported-cobalt catalyst was prepared with a α-Al_2O_3 model support. A model system was chosen to simplify a complex industrial supported catalyst system. In this model system, the porous support was replaced with a low surface area support and no promoters were added.

The results indicated that the cobalt loading corresponds to 0.095 ± 0.014 g Co/g α-Al_2O_3. Discrepancies showed that future work must ensure that the cobalt catalyst is stored under controlled conditions ensuring a constant water content of the calcined catalyst.

TEM-images of the freshly calcined catalyst sample showed that the cobalt oxide particles were not homogeneously distributed over the surface but consisted of particles which were partially presented in clusters. Hollow spheres were observed after the oxidation of the reduced calcined sample. A shell that consists out of small crystalline domains of ca. 9 nm (± 2.8 nm) surrounds the hollow sphere. Hollow spheres were also formed during the high-pressure oxidation of the reduced calcined sample. Smaller crystalline domains of 6.4 nm (± 1.5 nm) were formed in the outer shell.

XRD results confirmed the break-up of crystallites as expected for the formation of the hollow-spheres during the oxidation of a reduced calcined sample. A decrease in average Co_3O_4 crystallite size was observed from 33 nm to 8.9 nm. *In-situ* XRD showed that the oxidation of an oxidised reduced, re-oxidised, reduced catalyst (a third oxidation step) did not result in a smaller average Co_3O_4 crystallite size. The smallest average Co_3O_4 crystallite size of 6.4 nm was obtained during high-pressure oxidation.

The thinner shell (smaller crystalline domains) following the oxidation at high pressure in comparison to the shell formed following the oxidation at atmospheric pressure can be explained by a higher outward rate of diffusion of the cobalt than with the diffusion of cobalt during the oxidation at atmospheric pressure.

Smaller crystallites were observed after the reduction of a hollow sphere than after reduction of a solid oxide particle. This is also confirmed with an increase in metal surface area with a decrease in average Co_3O_4 crystallite size.

Hollow sphere formation leads to a well-dispersed catalyst with a high available surface area. This makes an oxidative regeneration process attractive that will result in an improvement of the the dispersion of cobalt metal on a deactivated catalyst.

The reduction temperatures of oxidised samples after hollow sphere formation were lower than formed from a calcined sample with solid oxide particles. The sample after high-pressure oxidation that contained a shell with the smallest crystallite domains showed a larger, broader peak from 400°C to 600°C probably due to small crystallites below 6 nm that are more difficult to reduce due to intimate contact with the support. *In-situ* XRD showed that not only the on-set of the reduction of the re-oxidised sample start at a lower temperature, but also the whole reduction process occurred at a lower temperature of re-oxidised sample.

The surface rate of CO consumption showed that the catalysts, after hollow sphere formation, are less active. Small cobalt crystallites (smaller than 6 nm) were observed with TEM measurements after the reduction of samples containing hollow spheres. The presence of crystallites smaller than 6 nm may result in lower turn-over-frequencies. If the metal surface area as measured by H_2-chemisorption is an indication of the number of active sites available in a catalyst, it would be expected that the re-oxidised under high-pressure would be the most active catalyst.

It is very important that model supported cobalt catalysts with a narrow range of crystallite sizes should be prepared. Several catalysts with different crystallites sizes will help to exclude factors where too small crystallites cannot be detected and it will help to understand the influence of crystallite size on activity and re-dispersion. A supported cobalt catalysts should be prepared with a narrow range of crystallite sizes that varied from below 6 nm. With particles smaller than 6 nm, the turnover frequencies can be investigated.

Metal particles with a narrow range of crystallite sizes will help to determine if there is a difference in the size of the void of the hollow sphere of a catalyst re-oxidised at atmospheric pressure or at pressure.

Metal particles with a narrow range of crystallite sizes above 6 nm will exclude the difficulty to analyse small particles with XRD that is limited by the detection limit of XRD (the lower size limit in crystallite size determination using XRD is ca. 3-5 nm depending on the noise level). It will help with the investigation if there is indeed an increase in Fischer Tropsch synthesis activity with a better re-dispersed catalyst after hollow sphere formation. This would link activity with a higher metal surface area after the reduction of a re-oxidised catalyst. This will also help to confirm that Co_3O_4 crystallite size can be linked with Fischer Tropsch synthesis activity and a better dispersed catalyst after reduction.

CHAPTER 7

REFERENCES

[1] M. Claeys,, E. van Steen
"Basic studies"
in "Fischer-Tropsch Technology" (A.P. Steynberg, M.E. Dry, Eds.)
Studies Surface Science and Catalysis **154** (2004), 601-680.

[2] P.J. van Berge, R.C. Everson
"Cobalt as an alternative Fischer-Tropsch catalyst to iron for the production of middle distillates"
In "Natural Gas Conversion IV" (M. de Pontes, C.P. Nicolaides, J.H. Scholz, M.S. Scurrell, Eds.)
Studies Surface Science and Catalysis **102** (1996), 207-212.

[3] A.M. Saib, A. Borgna, J. van de Loosdrecht, P.J. van Berge, J.W. Niemantsverdriet
"XANES study of the susceptibility of nano-sized cobalt crystallites to oxidation during realistic Fischer–Tropsch synthesis "
Applied Catalysis A: General **312** (2006) 12-19.

[4] D.J. Moodley
"On the deactivation of Fischer-Tropsch synthesis catalyst"
PhD thesis, University of Eindhoven (2008).

[5] M.J. Overett, B. Breedt, E. Du Plessis, W. Erasmus, J. Maloka, J. Van de Loosdrecht
"Sintering as a deactivation mechanism for an alumina supported cobalt Fischer-Tropsch synthesis catalyst"
Preprints Papers - American Chemical Society, Division Petrochemistry **53(2)** (2008), 126.

[6] E. van Steen, M. Claeys
"Fischer-Tropsch catalysts for the Biomass-to-Liquid (BTL)-process"
Chemical Engineering & Technology **31(5)** (2008), 655-666.

[7] A.M. Saib, D.J. Moodley, I.M. Ciobîcã, M.M. Hauman, B.H. Sigwebela, C.J. Weststrate, J.W. Niemantsverdriet, J. Van de Loosdrecht
"Fundamental understanding of deactivation and regeneration of cobalt Fischer–Tropsch synthesis catalysts"
Catalysis Today **154** (2010), 271-282.

[8] R. Huang, X. Zhan, K. Agee, K.B. Arcuri, J. Inga
"Syntroleum catalyst regeneration process for a gas-to-liquid plant"
Preprints Papers-American Chemical Society, Division Petrochemistry **50(2)** (2005), 185.

[9] R. Huang, K.L. Agee, K.B. Arcuri, F. Schubert
"Process for regenerating a slurry Fischer-Tropsch catalyst"
US Patent 02/0183403 (2002).

[10] A. Tavasoli, R.M.M. Abbasiou, A.K. Dalai
"Deactivation behaviour of ruthenium promoted Co/γ-Al_2O_3 catalysts in Fischer-Tropsch synthesis"
Applied Catalysis A: General **346** (2008), 58-64.

[11] N.A. Tsakoumis, M. Rønning, Ø. Borg, E. Rytter, A. Holmen
"Deactivation of cobalt-based Fischer-Tropsch catalysts: a review"
Catalysis Today **154** (2010), 162-182.

[12] H. Karaca, O.V. Safonova, S. Chambrey, P. Fongarland, P. Roussel, A. Griboval-Constant, M. Lacroix, A.Y. Khodakov
"Structure and catalytic performance of Pt-promoted alumina supported cobalt catalysts under realistic conditions of Fischer-Tropsch synthesis"
Journal of Catalysis **277** (2011), 14-26.

[13] J.E. Stulga, P. Wynblatt, J.K. Tien
"Particle splitting and redispersion phenomena in model alumina-supported platinum catalysts"
Journal of Catalysis **62** (1980), 59-69.

[14] J. Okai, H. Kubicka
"Influence of oxidation-reduction treatment on activity of Re/γ-Al_2O_3-catalysts diluted with γ-Al_2O_3"
Applied Catalysis A: General **209** (2001), 375-381.

[15] A.P. Steynberg
"Introduction to Fischer-Tropsch technology"
in "Fischer-Tropsch Technology" (A.P. Steynberg, M.E. Dry, Eds.)
Studies Surface Science and Catalysis **154** (2004), 1-63.

[16] M.E. Dry
"Chemical concepts used for engineering purposes"
in "Fischer-Tropsch Technology" (A.P. Steynberg, M.E. Dry, Eds.)
Studies Surface Science and Catalysis **154** (2004), 196-257.

[17] L. Dancuart, A.P. Steynberg
"Fischer-Tropsch based GTL technology: a new process"
in "Fischer-Tropsch Technology" (A.P. Steynberg, M.E. Dry, Eds.)
Studies Surface Science and Catalysis **154** (2004), 379-399.

[18] M.E. Dry
"FT catalysts"
in "Fischer-Tropsch Technology" (A.P. Steynberg, M.E. Dry, Eds.)
Studies Surface Science and Catalysis **154** (2004), 533-600.

[19] G. Huff jr., C.N. Satterfield
"Intrinsic kinetics for the Fischer-Tropsch synthesis on a reduced fused magnetite catalyst"
Industrial Engineering Chemistry Process Design Development **23** (1984), 696-705.

[20] I.C. Yates, C.N. Satterfield
"Intrinsic kinetics of the Fischer-Tropsch synthesis on a cobalt catalyst"
Energy & Fuels **5** (1991), 168-173.

[21] E. van Steen, H. Schulz
"Polymerisation kinetics of the Fischer-Tropsch CO hydrogenation using iron and cobalt based catalysts"
Applied Catalysis A: General **186** (1999), 309-320

[22] D. Wei, J.G. Goodwin jr., R. Oukaci, A.H. Singleton
"Attrition resistance of cobalt F-T catalysts for slurry bubble column use"
Applied Catalysis A: General **210** (2001), 137-150.

[23] A.Y. Khodakov, W. Chu, P. Fongarland
"Advances in the development of novel cobalt Fischer-Tropsch catalysts for synthesis of long chain hydrocarbons and clean fuel"
Chemical Reviews **107** (2007), 1692-1744.

[24] E. Iglesia

“Design, synthesis, and use of cobalt-based Fischer-Tropsch synthesis catalysts”
Applied Catalysis A: General **161** (1997) 59-78.

[25] G.L. Bezemer, J.H. Herman, P.C.E. Kuipers, H. Oosterbeek, J.E. Holewijn, X.Xu, F. Kapteijn, A.J.van Dillen, K.P. de Jong
“Cobalt particle size effects in the Fischer-Tropsch reaction studied with carbon nanofiber supported catalysts”
Journal of the American Chemical Society **128** (2006), 3956-3964.

[26] J.P. den Breejen, P.B. Radstake, G.L. Bezemer, J.H. Bitter, V. Frøseth, A. Holmen, K.P. de Jong
“On the origin of the cobalt particle size effects in Fischer-Tropsch catalysis”
Journal of the American Chemical Society **131** (2009), 7197-7203.

[27] A.M. Saib, M. Claeys, E. van Steen
“Silica supported cobalt Fischer-Tropsch catalysts: Effect of pore diameter of support”
Catalysis Today **71** (2002),395-402.

[28] Ø. Borg, S. Eri. E.A. Blekkan, S. Storsæter, H. Wigum, E. Rytter, A. Holmen
“Fischer-Tropsch synthesis over γ-alumina supported cobalt catalysts: Effect of support variables”
Journal of Catalysis **248** (2007), 89-100.

[29] G. Jacobs, T.K. Das. Y. Zhang, J. Li, G. Racoillet, B.H. Davis
“Fischer-Tropsch synthesis: support, loading, and promoter effects on the reducibility of cobalt catalysts”
Applied Catalysis A: General **233** (2002), 263-281

[30] S. Storsæter,, B. Tøtdal, J.C. Walmsley, B.S. Tanem, A. Holmen
“Characterization of alumina-, silica- and titania-supported cobalt Fischer-Tropsch catalysts”
Journal of Catalysis **236** (2005), 139-152.

[31] G. Jacobs, Y. Ji, B.H. Davis, D. Cronauer, A.J. Kropf, C.L. Marshall
“Fischer-Tropsch synthesis: Temperature programmed EXAFS/XANES investigation of the influence of support type, cobalt loading, and noble metal promoter addition to the reduction behavior of cobalt oxide particles”
Applied Catalysis A: General **333** (2007), 177-191.

[32] W. Chu, P.A. Chernavskii, L. Gengembre, G.A. Pankina, P. Fongarland, A.Y. Khodakov
”Cobalt species in promoted cobalt alumina-supported Fischer–Tropsch catalysts”
Journal of Catalysis **252** (2007) 215-230.

[33] A.Y. Khodakov
“Enhancing cobalt dispersion in supported Fischer-Tropsch catalysts via controlled decomposition of cobalt precursors”
Brazilian Journal of Physics **39** (2009), 171-175.

[34] J. van de Loosdrecht, S. Barradas, E.A. Caricato, P.J. van Berge, J.L. Visagie
“Support modification for cobalt based slurry phase Fischer-Tropsch catalysts”
Preprints of symposium “Production of Fuels and Chemicals from Synthesis Gas”, Divison of Fuel Chemistry, 220th ACS meeting, Washington DC, USA, 20-24 August 2000, 587-591.

[35] G.L. Bezemer, P.B. Radstake, V. Koot, A.J. van Dillen, JW.Geus, K.P. de Jong
“Preparation of Fischer–Tropsch cobalt catalysts supported on carbon nanofibers and silica using homogeneous deposition-precipitation”
Journal of Catalysis **237** (2006) 291-302.

[36] B.C. Dunn, P. Cole, D.J. Covington, E.C. Heider, J. Gasser, E.M. Eyring, H.L.C. Meuzelaar, R.J. Pugmire

"Fischer-Tropsch catalysts supported on sol-gel-derived silica"
Preprints Papers – American Chemical Society Fuel Chemistry Division **48**(1) (2003), 212.

[37] Y.Q. Zhuang, M. Claeys, E. van Steen
"Novel synthesis route for egg-shell, egg-white and egg-yolk type of cobalt on silica catalysts"
Applied Catalysis A: General **301** (2006), 138-142.

[38] M. Bakhtiari, F. Khorasheh, A. Zamanian, A. Nakhaepour, M. Irani
"Preparation, evaluation and characterization of monolithic catalysts for Fischer-Tropsch synthesis"
Petroleum and Coal **50(3)** (2008), 56-61.

[39] J.R.A. Sietsma, H. Friedrich, A. Broersma, M. Versluis-Helder, A.J. van Dillen, P.E. de Jong, K.P. de Jong
"How nitric oxide affects the decomposition of supported nickel nitrate to arrive at highly dispersed catalysts"
Journal of Catalysis **260** (2008), 227-235.

[40] P.A. Chernavskii, A.Y. Khodakov, G.V. Pankina, J.-S. Giradon, E. Quinet,
"In situ characterization of the genesis of cobalt metal particles in silica-supported Fischer-Tropsch catalysts using Foner magnetic method"
Applied Catalysis A; General **306** (2006) 108-119.

[41] E. van Steen, G.S. Sewell, R.A. Makhote, C. Micklethwaite, H. Manstein, M. de Lange, C.T. O'Connor
"TPR study on the impregnation of impregnated Co/SiO_2 catalysts"
Journal of Catalysis **162** (1996), 220-229.

[42] S. Rane, Ø. Borg, J. Yang, E. Rytter, A. Holmen
"Effect of alumina phases on hydrocarbon selectivity in Fischer-Tropsch synthesis"
Applied Catalysis A: General **388** (2010), 160-167.

[43] Y. Zhang, D. Wei, S. Hammache, J.G. Goodwin jr.
"Effect of water vapor on the reduction of Ru-promoted Co/Al_2O_3"
Journal of Catalysis **188** (1999), 281-290.

[44] R.L. Espinoza, J.L. Visagie, P.J. van Berge, F.M. Bolder
"Catalysts"
US patent 5733839 (1998) assigned to Sastech Ltd.

[45] G. Jacobs, A. Sarkar, Y. Ji. M. Luo, A. Dozier, B.H. Davis
"Fischer-Tropsch synthesis: assessment of the ripening of cobalt clusters and mixing between Co and Ru promoter via oxidation-reduction-cycles over lower Co-loaded Ru-Co/Al_2O_3 catalysts"
Industrial Engineering Chemistry Research **47** (2008), 672-680.

[46] B. Jongsomijt, J.G. Goodwin jr.
"Cobalt compound formation in Co/Al_2O_3: effect of reduction gas containing CO"
Catalysis Today **77** (2002), 191-204.

[47] V.A. de la Peňa O'Shea, N. Homs, J.L.G. Fierro, P. Ramírez de la Piscina,
"Structural changes and activation treatment in a Co/SiO_2 catalyst for Fischer–Tropsch synthesis"
Catalysis Today **114** (2006) 422-427.

[48] P.L.J. Gunter, J.W. Niemantsverdriet, F.H. Ribeiro, G.A.Somorjai,
"Surface science approach to modelling catalysts"
Catalysis Review – Science and Engineering **39** (1997), 77-168.

[49] J.A. Moulijn, A.E. van Diepen, F. Kapteijn,
"Catalyst deactivation, is it predictable? What to do?"
Applied Catalysis A: General **212** (2001) 3-16.

[50] C.H. Bartholomew
"Mechanisms of catalyst deactivation"
Applied Catalysis A: General **212** (2001) 17-60.

[51] H. Wright, A. Raje, R.L. Espinoza
"Pressure-swing catalyst regeneration procedure for Fischer-Tropsch catalyst"
Patent WO 02/092227 A1 (2002) assigned to ConocoPhilips Co.

[52] T.L. van der Walt, P.S. Nkwanyana, B.H. Sigwebela, J. van de Loosdrecht, E.L. Viljoen
Presentation at Catalysis Society of South Africa (CATSA), 10-13 November, 2002.

[53] D. Schanke, A.M. Hilmen, E. Bergene, K. Kinnari, E. Rytter, A. Ådnanes, A. Holmen
"Reoxidation and deactivation of supported cobalt Fischer-Tropsch catalysts"
Energy & Fuels **10** (1996), 867-872.

[54] P.J. van Berge, J. van de Loosdrecht, S. Barradas, A.M. van der Kraan
"Oxidation of cobalt based Fischer-Tropsch catalysts as a deactivation mechanism"
Catalysis Today **58** (2000), 321-334.

[55] G.L. Bezemer, T.J. Remans, A.P. van Bavel, A.I. Dugulan
"Direct evidence of water-assisted sintering of cobalt on carbon nanofiber catalysts during simulated Fischer-Tropsch conditions revealed with in situ Mössbauer spectroscopy
Journal of American Chemical Society **132** (2010), 8540-8541.

[56] I.M. Ciobîcã, R.A. van Santen, P.J. van Berge, J. van de Loosdrecht
"Adsorbate induced reconstruction of cobalt surfaces"
Surface Science **602** (2008), 17-27.

[57] D.J. Moodley, J. van de Loosdrecht, A.M. Saib, M.J. Overett, A.K. Datye, J.W. Niemantsverdriet
"Carbon deposition as a deactivation mechanism of cobalt-based Fischer-Tropsch synthesis catalysts under realistic conditions"
Applied Catalysis A; General **354** (2009), 102-110.

[58] E. van Steen, M. Claeys, M.E. Dry, J. van de Loosdrecht, E.L. Viljoen, J.L. Visagie
"Stability of nanocrystals: Thermodynamic analysis of the reduction and re-oxidation of cobalt in water/hydrogen mixtures"
Journal of Physical Chemistry B **109** (2005), 3575-3577.

[59] J.C.W. Swart
"A theoretical view on deactivation of cobalt-based Fischer-Tropsch catalysts"
PhD thesis, University of Cape Town (2008).

[60] D.B. Dadyburjor
"Regions of Validity for Models of Regeneration of Sintered Supported Metal Catalysts"
in "Catalyst Deactivation" (B. Delmon, G.F. Froment, Eds)
Studies in Surface Science and Catalysis **6** (1980), 341-152.

[61] U. Lassi
"Deactivation Correlations of Pd/Rh Three-Way Catalysts Designed for Euro IV Emission Limits"
PhD-thesis, University of Oulu (2003).

[62] J.C.W. Swart, I.M. Ciobîcã, R.A. van Santen, E. van Steen
"Intermediates in the formation of graphitic carbon on a flat FCC-Co(111) surface"
Journal of Physical Chemistry C **112** (2008), 12899-12904

[63] J.C.W. Swart, E. van Steen, I.M. Ciobîcã, R.A. van Santen
"Interaction of graphene with FCC-Co(111)"
Physical Chemistry Chemical Physics **11** (2009), 803-807.

[64] J.W. Niemantsverdriet, D.J. Moodley, A.M. Saib, J. van de Loosdrecht
"Formation and influence of carbon on cobalt Fischer Tropsch synthesis catalysts: An integrated review"
Preprints Papers - American Chemical Society, Division Petrochemistry **53(2)** (2008), 122-125.

[65] O. Roelen, H. Heckel, F. Hanish
"Method for the reactivation of catalysts for the hydrogenation of carbon oxyde"
US Patent 2,289,731 (1942) assigned to Hydrocarbon Synthesis Corp.

[66] E.A. Naragon, J.H. Vergillio, A.J. Millendorf
"Regeneration of cobalt catalysts by oxidation"
US Patent 2,626,246 (1953) assigned to Texas Co.

[67] E.A. Naragon, J.H. Vergillio, A.J. Millendorf
"Process for regenerating cobalt catalysts"
Patent CA 508217 (1954) assigned to Texas Development Corporation

[68] X.D. Zhan, K.B. Arcuri, R. Huang, K. Agee, J. Engman, H.J. Robata
"Regeneration of cobalt-based Fischer-Tropsch catalysts"
Preprints Papers - American Chemical Society, Division Petrochemistry **49(2)** (2004), 179.

[69] F.G. van Dongen, J. Eilers, G.J. van Heeringen, W.P. Leenhouts, M.M.G. Senden
"Catalyst activation process and catalyst reactivation process"
RSA Patent 95/10296 (1995)

[70] M.M. Hauman, D.J. Moodley, S.D. Nthute, A.M. Saib, B.H. Sigwebela, J. van de Loosdrecht
Oral presentation, Catalysis Society of South Africa (CATSA), 10-12 November, 2008

[71] C.H. Bartholomew
"Sintering and redispersion of supported metals: Perspectives from the literature of the past decade"
in "Catalyst Deactivation 1997" (C.H. Bartholomew, G.A. Fuentes, Eds.)
Studies in Surface Science and Catalysis **111** (1997), 585- 592.

[72] D. Potoczna-Petru, L. Krajczyk
"Microstructure evolution of Co particles supported on carbon induced by oxidation-reduction treatment"
Journal of Materials Science Letters **14** (1995) 1294-1297.

[73] D. Potoczna-Petru, L. Keiński
"Influence of oxidation-reduction treatment on the interaction of cobalt particles with silica support"
Journal of Materials Science **28** (1993), 3501-3505.

[74] Y. Yin, R.M. Rioux, C.K. Erdonmez, S. Hughes, G.A. Somorjai, A.P. Alivisatos
"Formation of hollow nanocrystals through the nanoscale Kirkendall effect"
Science **304** (2004) 711-714.

[75] P.A. Chernavskii, G.V. Pankina, V.I. Zaikovskii, N. V. Peskov, P.Afanasiev

"Formation of hollow spheres upon oxidation of supported cobalt nanoparticles"
Journal of Physical Chemistry C **112** (2008), 9573-9578.

[76] R. Nakamura, D. Tokozakura, H. Nakajima
"Hollow oxide formation by oxidation of Al and Cu nanoparticles"
Journal of Applied Physics **101** (2007), 074303.

[77] C.M. Wang, D.R. Baer, L.E. Thomas, J.E. Amonette, J. Antony, Y. Qiang, G. Duscher
"Void formation during early stages of passivation: Initial oxidation of iron nanoparticles at room temperature"
Journal of Applied Physics **98** (2005), 094308.

[78] A. Rai,, K. Park, L. Zhou, M.R. Zachariah
"Understanding the mechanism of aluminium nanoparticle oxidation"
*Combustion Theory and Modelling***10** (2006), 843-859.

[79] R. Nakamura, J.-G. Lee, D. Tokozakura, H. Mori, H. Nakajima
"Formation of hollow ZnO through low temperature oxidation of Zn nanoparticles"
Materials Letters **61** (2007), 1060-1063.

[80] J.W. Niemantsverdriet
"Spectroscopy in Catalysis: An Introduction"
3rd Ed., Wiley-VCH Verlag GmbH& Co. KGgA, Weinheim (2007).

[81] R.A. Young
"An introduction to the Rietveld method"
in "The Rietveld Method" (R.A. Young, Ed.), International Union of Crystallography Book Series 5, Reprinted 1996, Oxford Press (1993), Chapter 1.

[82] H.M. Rietveld
"A profile refinement method for nuclear and magnetic structures"
Journal of Applied Crystallography **2** (1969), 65-71.

[83] N.N.
"Topas – Total Pattern Analysis solution"
http://www.bruker-axs.de/uploads/media/TOPAS_Structure_Determination_H88-EXS013_02.pdf

[84] J.R. Connolly
"Introduction quantitative X-ray diffraction methods"
http://epswww.unm.edu/xrd/xrdclass/09-Quant-intro.pdf

[85] P.A. Webb, C. Orr,
"Analytical methods in fine particle technology"
Micromeritics Instrumentation Corp., p. 219 – 230 (1997).

[86] J.A. Malherbe
"The effect of catalysts pre-treatment on the mechanical integrity and synthesis performance of an iron based Fischer-Tropsch catalyst
MSc-thesis, University of Cape Town, p. 77-78 (2006).

[87] G.S. Sewell, E. van Steen, C.T.O'Conner
"Use of TPR/TPO for characterization of supported cobalt catalysts"
Catalysis Letters **37** (1996), 255-260.

[88] P. Scardi, M. Leoni
"Fourier modelling of the anisotropic line broadening of X-ray diffraction profiles due to line and plane lattice defects"
Journal of Applied Crystallography **32** (1999), 671-682.

[89] A. Feller, M. Claeys, E. van Steen

”Cobalt cluster effects in zirconium promoted Co/SiO_2 Fischer-Tropsch catalysts”
Journal of Catalysis **185** (1999) 120-130.

[90] I. Lisiecke, M. Wells, D. Parker, M.P. Pileni
“2D self-organization of core/shell Co_{hcp}/Co nanocrystals”
Langmuir **24** (2008), 4295-4299.

[91] F.R. Feret, D. Roy, C. Boulanger
“Determination of alpha and beta alumina in ceramic alumina by X-ray diffraction”
Spectrochimica Acta Part B: Atomic Spectroscopy **55** (2000), 1051-1061.

[92] F. Arena, A. Parmaliana
“Silica supported molybdena catalysts. Surface structure, reduction pattern, and oxygen chemisorption”
Journal of Physical Chemistry **100** (1996), 19994-20005.

[93] I.T. Ghampson, C. Newman, L. Kong, E. Pier, K.D. Hurley, R.A. Pllock, B.R. Walsh, B. Goundie, J. Wright, M.C. Wheeler, R.W. Meulenberg, W.J. DeSisto, B.G. Frederick, R.N. Austin
“Effects of pore diameter on particle size, phase and turnover frequency in mesoporous silica supported cobalt Fischer-Tropsch catalysts”
Applied Catalysis A: General **388** (2010) 57-67.

[94] D. Antonangeli, L. R. Benedetti, D. L. Farber, G. Steinle–Neumann, A. Auzende, J. Badro, M. Hanfland, M. Krisch
“Anomalous pressure evolution of the axial ratio c/a in hcp cobalt: Interplay between structure, magnetism, and lattice dynamics”
Applied Physics Letters **92** (2008), 111911.

[95] C. Maurizio, G. Mattei, P. Canton, E. Cattaruzza, C. de Julián Fernández, P. Mazzoldi, F. D'Acapito, G. Battaglin, C. Scian, A. Vomiero
“Thermal evolution of cobalt nanocrystals embedded in silica”
Materials Science and Engineering C **27** (2007), 193–196.

[96] O. Kitakami, H. Sato, Y. Shimada, F. Sato, M. Tanaka
“Size effect on the crystal phase of cobalt fine particles”
Physical Review B **56** (1997), 13849-13854.

[97] S. Sun, N. Tsubaki, K. Fujimoto
“Promotional effects of noble metal to Co-based Fischer-Tropsch catalysts prepared from mixed salts”
Chemistry Letters **2** (2000), 176-177.

APPENDIX A

In-situ XRD crystallite size and relative abundances data

Table A.1: *In-situ XRD results of 1st reduction step*

1st reduction	Crystallite size (nm)					Relative abundances (% (m/m))				
Temp (°C)	**Al_2O_3**	**Co_3O_4**	**CoO**	**Co (fcc)**	**Co hcp)**	**Al_2O_3**	**Co_3O_4**	**CoO**	**Co (fcc)**	**Co (hcp)**
40	139.3	33.8	Fix @ 10	-	-	90.1	8.5	1.5	0	0
80	139.6	33.0	Fix @ 10	-	-	90.0	8.5	1.5	0	0
100	141.2	33.4	Fix @ 10	-	-	89.8	8.7	1.5	0	0
120	140.8	32.8	Fix @ 10	-	-	89.7	8.8	1.4	0	0
140	141.0	32.3	Fix @ 10	-	-	89.5	8.9	1.6	0	0
160	142.1	30.9	16.7	-	-	89.5	9.2	1.4	0	0
180	142.2	32.2	3.9	Fix @ 15	-	88.0	8.0	3.6	0.4	0
200	143.8	30.5	6.5	Fix @ 15	-	87.9	5.4	6.3	0.4	0
220	145.7	15.8	8.6	Fix @ 15	-	88.4	1.6	9.5	0.6	0
240	144.2	0	9.6	14.7	Fix @ 6	89.7	0	8.0	1.1	1.2
260	144.6	0	9.8	17.5	Fix @ 6	90.1	0	6.5	1.5	1.9
280	147.7	0	8.9	11.5	Fix @ 6	89.8	0	5.8	2.1	2.3
300	149.4	0	9.0	11.7	Fix @ 6	90.5	0	4.3	2.4	2.8
320	150.4	0	6.8	13.1	5.0	90.4	0	2.9	2.9	3.8
340	152.8	-	-	11.0	5.0	92.3	0	0	4.1	3.6
360	153.4	-	-	13.7	5.0	92.9	0	0	3.1	3.9
380	158.1	-	-	12.2	5.0	91.9	0	0	3.7	4.4
400	157.7	-	-	12.9	5.0	91.8	0	0	3.7	4.4
425	163.0	-	-	13.3	5.0	91.6	0	0	3.8	4.6
450	165.5	-	-	13.9	5.0	91.6	0	0	3.7	4.7
450	170.7	-	-	14.4	5.0	91.6	0	0	3.8	4.6

Table A.2: *In-situ XRD results of 1st oxidation step*

1st oxidation	Crystallite size (nm)					Relative abundances (% (m/m)				
Temp (°C)	Al_2O_3	Co_3O_4	CoO	Co (fcc)	Co (hcp)	Al_2O_3	Co_3O_4	CoO	Co (fcc)	Co (hcp)
70	165.8	0	11.7	16.5	5.0	91.8	0	1.6	2.6	4.1
80	168.7	0	7.6	16.5	5.0	91.4	0	2.1	2.5	3.9
100	168.5	0	Fix @ 15	19.8	5.0	92.6	0	1.8	2.1	3.5
120	168.3	0	Fix @ 15	20.3	5.0	93.1	0	1.8	1.8	3.3
140	167.2	0	Fix @ 15	20.1	5.0	93.6	0	1.9	1.7	2.8
160	173.6	3.1	8.1	54.7	Fix @ 6	92.0	2.1	3.2	0.7	2.1
180	168.2	4.7	12.7	19.6	Fix @ 6	90.3	5.2	1.4	1.2	1.9
200	168.6	5.3	Fix @ 15	18.7	Fix @ 6	89.3	6.6	1.3	1.1	1.7
220	168.8	5.8	12.0	32.8	Fix @ 6	88.4	8.0	1.6	0.6	1.2
240	173.6	5.0	Fix @ 15	8.0	Fix @ 6	84.7	11.5	0.9	1.6	1.3
260	169.6	7.0	Fix @ 15	10.1	Fix @ 6	87.2	10.6	1.1	0.6	0.5
280	170.1	8.2	Fix @ 15	-	-	87.8	10.7	1.2	0	0
300	170.9	9.3	Fix @ 15	-	-	87.5	11.0	1.4	0	0

Table A.3: *In-situ XRD results of 2nd reduction step*

2nd	Crystallite size (nm)	Relative abundances (% (m/m)

reduction										
Temp (°C)	**Al_2O_3**	**Co_3O_4**	**CoO**	**Co (fcc)**	**Co hcp)**	**Al_2O_3**	**Co_3O_4**	**CoO**	**Co (fcc)**	**Co (hcp)**
35	167.4	9.5	Fix @ 15	-	-	87.4	11.4	1.2	0.0	0.0
80	167.1	9.4	Fix @ 15	-	-	87.3	11.5	1.2	0.0	0.0
100	166.5	9.4	Fix @ 15	-	-	87.2	11.6	1.2	0.0	0.0
120	166.4	9.4	Fix @ 15	-	-	87.2	11.6	1.3	0.0	0.0
140	166.0	9.5	Fix @ 15	-	-	87.4	11.4	1.2	0.0	0.0
160	167.6	9.6	15.4	-	-	87.5	11.2	1.3	0.0	0.0
180	168.7	9.3	4.7	Fix @ 20	-	86.7	10.0	2.8	0.5	0.0
200	166.7	10.0	6.5	Fix @ 20	-	87.5	5.9	6.0	0.6	0.0
220	167.8	Fix @ 7.1	8.3	14.9	21.8	88.5	1.8	8.4	0.7	0.6
240	164.8	-	7.3	19.8	7.5	91.6	0.0	3.8	1.5	3.1
260	168.9	-	Fix @ 40	16.3	5.7	92.7	0.0	0.6	2.2	4.5
280	166.7	-	Fix @ 20	Fix @ 20	4.8	91.4	0.0	0.8	2.2	5.6
300	169.1	-	33.0	16.3	5.0	91.3	0.0	0.6	2.6	5.6
320	167.3	-	43.8	16.3	5.0	91.1	0.0	0.5	2.6	5.8
340	163.7	-	52.5	19.2	5.0	91.1	0.0	0.4	2.5	5.9
360	168.5	-	110.6	18.3	5.2	91.9	0.0	0.3	2.5	5.3
380	168.6	-	49.1	16.1	5.0	91.1	0.0	0.4	2.8	5.7
400	169.8	-	113.8	19.8	5.0	91.9	0.0	0.3	2.4	5.4
425	169.6	-	73.1	16.8	5.0	91.1	0.0	0.4	2.8	5.8
450	170.5	-	119.5	19.7	5.0	91.8	0.0	0.3	2.5	5.4
450	172.3	-	112.2	19.1	5.1	91.9	0.0	0.3	2.6	5.3

Table A.4: *In-situ XRD results of 2nd oxidation step*

2nd oxidation	**Crystallite size (nm)**	**Relative abundances (% (m/m)**

Temp (°C)	Al_2O_3	Co_3O_4	CoO	Co (fcc)	Co (hcp)	Al_2O_3	Co_3O_4	CoO	Co (fcc)	Co (hcp)
75	166.0	Fix @ 10	59.5	19.5	4.5	91.8	0.7	0.4	2.0	5.1
80	165.9	4.1	38.4	19.1	5.5	91.5	1.9	0.4	1.9	4.3
100	166.9	5.0	50.9	16.7	5.6	91.5	2.1	0.4	2.0	4.1
120	165.4	5.0	23.1	15.3	6.1	91.1	2.8	0.6	1.9	3.6
140	168.4	5.0	13.0	11.0	5.9	88.9	4.6	0.8	2.2	3.6
160	167.5	5.0	5.0	27.0	6.5	88.5	4.2	3.2	1.0	3.0
180	169.3	5.0	5.0	19.8	8.0	87.7	5.9	3.1	1.0	2.3
200	170.4	5.7	5.0	32.3	10.3	88.6	6.7	2.7	0.7	1.2
220	171.5	6.2	5.0	25.8	16.3	87.8	8.0	2.6	0.6	1.0
240	170.5	6.9	5.0	35.9	17.2	87.1	9.1	2.8	0.4	0.6
260	174.5	7.8	5.2	89.4	28.5	86.9	10.1	2.3	0.3	0.4
280	175.6	7.9	5.0	42.1	24.6	85.1	11.5	2.6	0.5	0.4
300	175.6	9.4	13.5	114.9	95.9	86.7	11.7	1.2	0.3	0.1

APPENDIX B

In-situ XRD-patterns of the first and last obtained pattern of each *in-situ* step

Figure B.1.1: *In-situ XRD-pattern of 1st reduction step at 40°C*

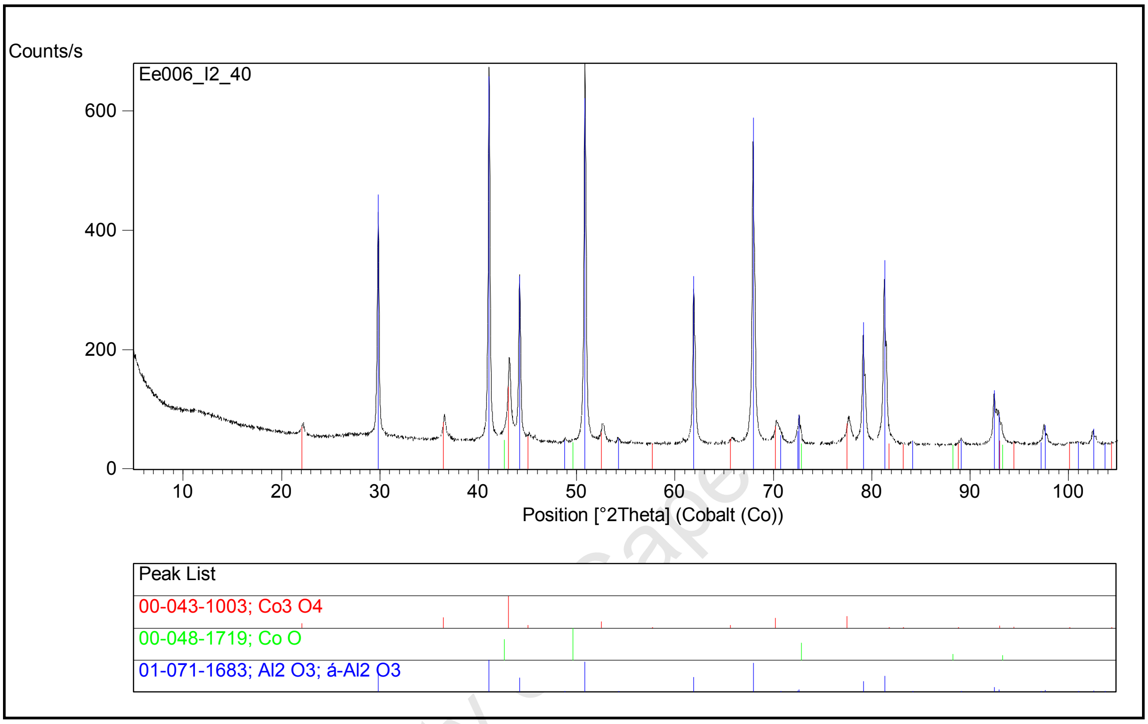

Figure B.1.2: *In-situ XRD-pattern of 1st reduction step at 450°C*

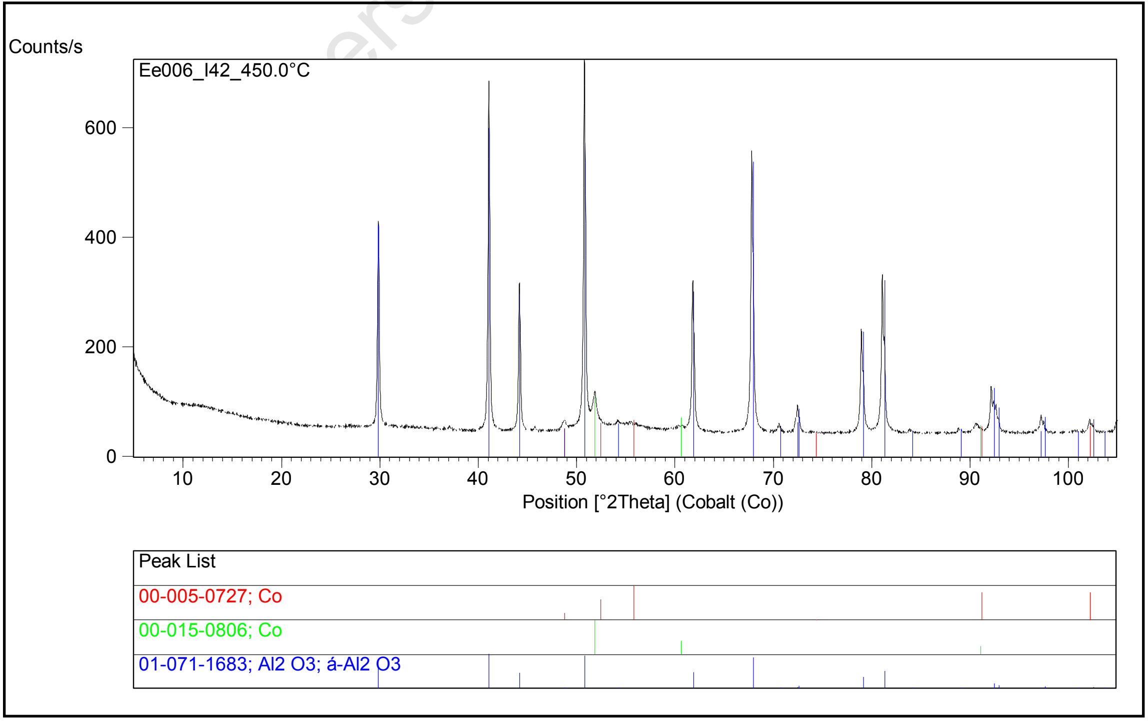

Figure B.2.1: *In-situ XRD-pattern of 1st oxidation step at 70°C*

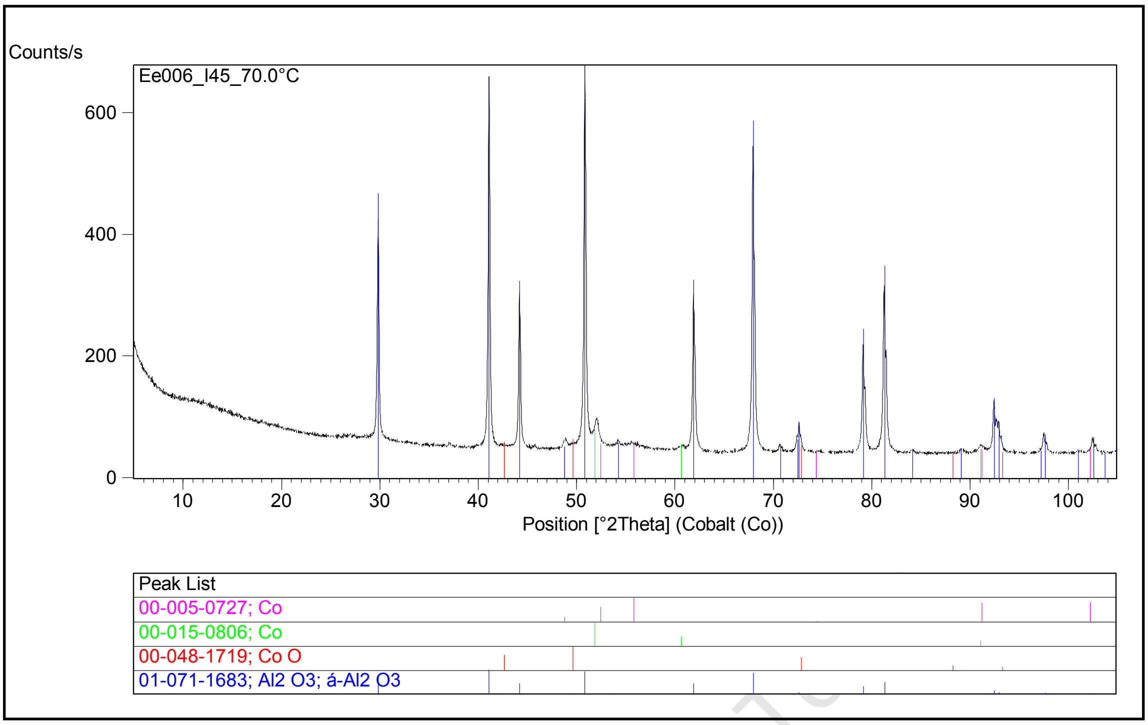

Figure B.2.2: *In-situ XRD-pattern of 1st oxidation step at 300°C*

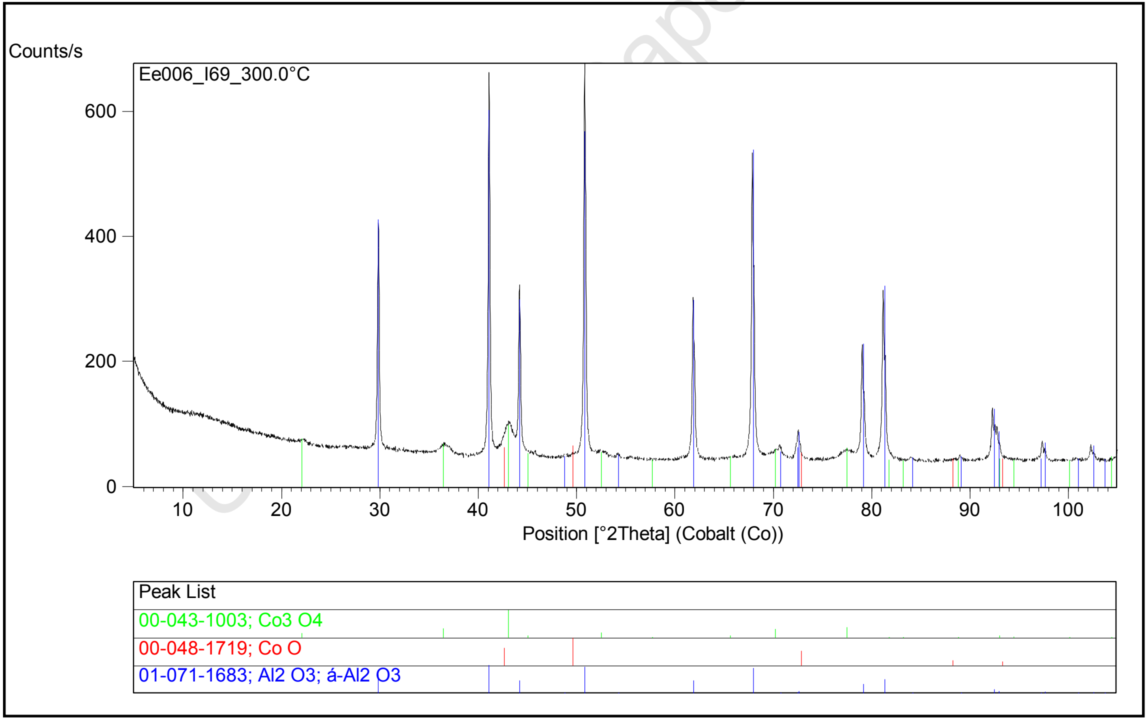

Figure B.3.1: *In-situ XRD-pattern of 2nd reduction step at 35°C*

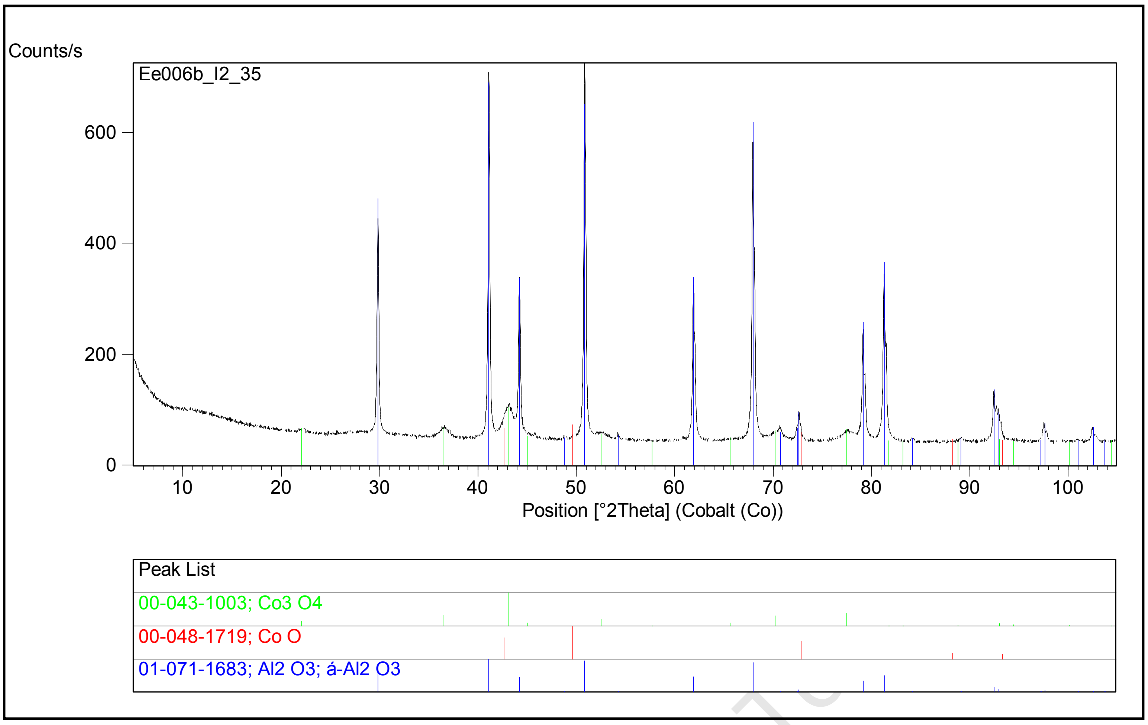

Figure B.3.2: *In-situ XRD-pattern of 2nd reduction step at 450°C*

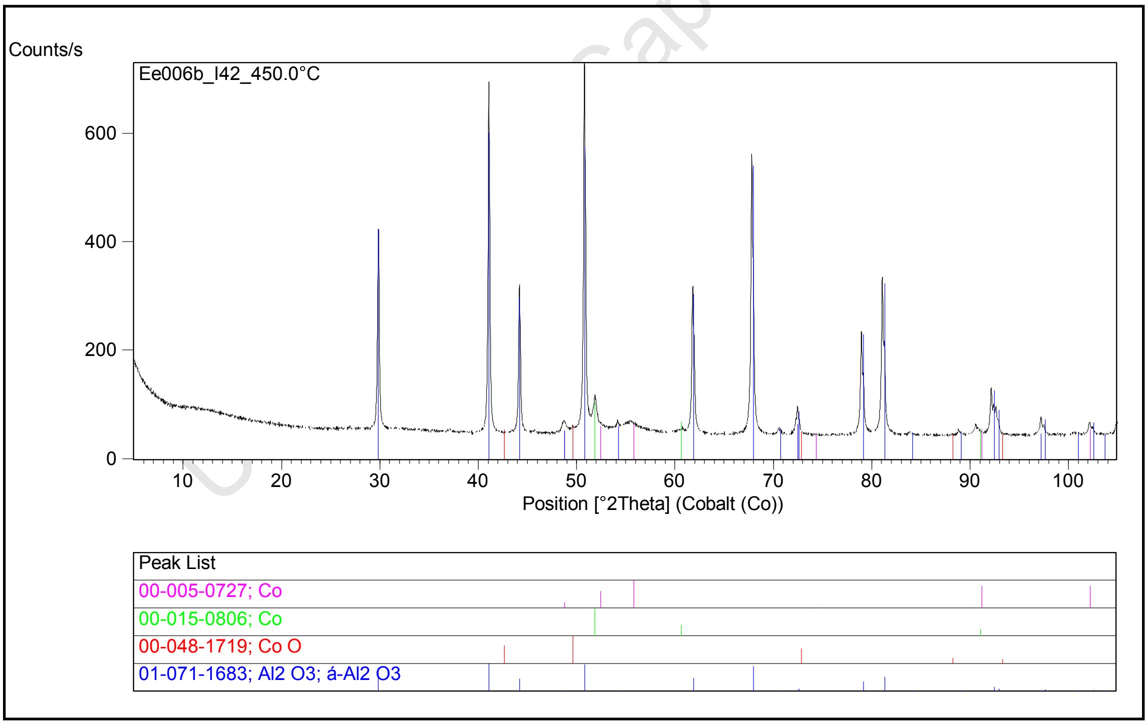

Figure B.4.1: *In-situ XRD-pattern of 2nd oxidation step at 75°C*

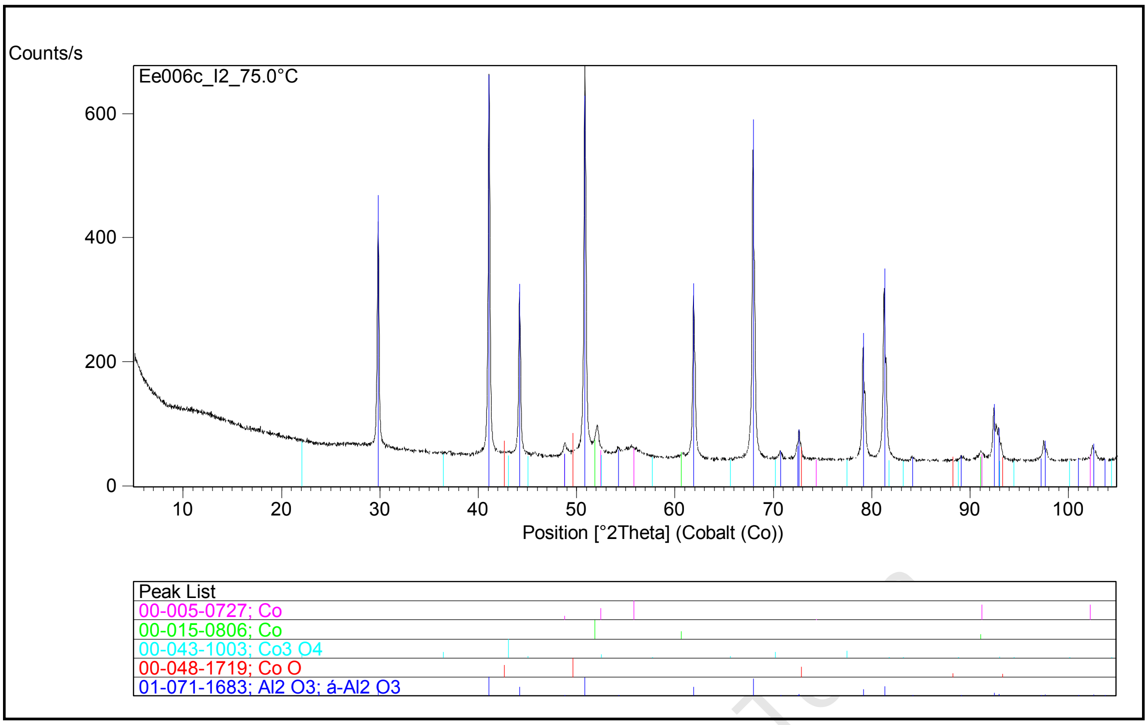

Figure B.4.2: *In-situ XRD-pattern of 2nd oxidation step at 300°C*